Total Internal Reflection Fluorescence Microscopy for Characterizing Biochemical Interactions

Bridgett L. Steele

A dissertation submitted to the faculty of the University of North Carolina at Chapel Hill in partial fulfillment of the requirements for the degree of Doctor of Philosophy in the Department of Chemistry.

Chapel Hill
2009

Approved by:

Dr. Nancy L. Thompson

Dr. James Jorgenson

Dr. J. Michael Ramsey

Dr. Dorothy Erie

Dr. Matthew Redinbo

ABSTRACT

Bridgett L. Steele: Total Internal Reflection Fluorescence Microscopy for Characterizing Biochemical Interactions
(Under the Direction of Nancy L. Thompson)

Total internal reflection fluorescence (TIRF) microscopy is a widely used technique for the study of biologically relevant processes both *in vitro* and *in vivo*. In TIRF, an incident light beam propagates through a transparent solid and encounters a solid/liquid interface at an angle sufficient enough such that the light undergoes total internal reflection, which generates an evanescent field that decays exponentially with distance from the surface. Thus, the main advantage of TIRF is that it selectively excites fluorescent molecules at or near the solid-solution interface. TIRF is used to study the thermodynamic and kinetic properties of three systems in this dissertation.

Pregnane X receptor (PXR) is a member of the nuclear receptor family of ligand activated transcriptional factors that regulate gene expression. Using TIRF, the ligand-dependent binding of PXR to the steroid receptor coactivator-1 (SRC-1) is studied in the presence of the known PXR activator, rifampicin. In this system, the ligand binding domain of PXR is immobilized at the solid-solution interface, and fluorescently-labeled SRC-1 peptide in solution is used to mimic the full length SRC receptor. By measuring the fluorescence intensity as a function of the solution concentration of fluorescently-labeled SRC-1 at constant, increasing concentrations of rifampicin, four equilibrium binding constants are obtained, which illustrate the cyclic nature of these interactions.

Discoidin domain receptor 2 (DDR2) is a receptor tyrosine kinase that is activated by fibrillar collagens in the extracellular matrix. Upon activation through collagen binding, DDR2 regulates cell adhesion, proliferation, and extracellular matrix remodeling. To study the binding of the extracellular domain of DDR2 to collagen, methods to deposit thin films of aligned or unaligned collagen I on fused silica slides were developed. Additionally, to characterize the effect of oligomerization of DDR2 on collagen binding, methods to separate monomeric, dimeric, and aggregates of DDR2 were also explored. This work represents the preliminary steps necessary to study the binding of surface immobilized collagen to fluorescently-labeled DDR2 using TIRF.

A new method using through-prism total internal reflection fluorescence microscopy with continuous photobleaching (TIR-CP) is presented. In this method, small structures, such as prokaryotic cells or isolated eukaryotic organelles, containing fluorescent molecules are adhered to a surface. This surface is continuously illuminated by an evanescent wave created by total internal reflection. The characteristic length describing the decay of the evanescent intensity with distance from the surface is smaller than the structures. The fluorescence decay rate resulting from continuous evanescent illumination is monitored as a function of the excitation intensity. The data at higher excitation intensities provide apparent translational diffusion coefficients for the fluorescent molecules within the structures because the decay results from two competing processes (the intrinsic photobleaching propensity and diffusion in the small structures). The theoretical basis for the technique is presented and the applicability of the technique is demonstrated by measuring the diffusion coefficient, 6.3 ± 1.1 μm^2/sec, of green fluorescent protein (GFP) in *Escherichia coli* cells.

To Mom and Dad:

Thank you for 28 years of unfaltering love and support.

And in Loving Memory of

Boots Kelly Richardson

ACKNOWLEDGEMENTS

First and foremost, I'd like to thank my parents for always being there for me, whether it was car problems, the numerous moves in the sweltering heat, or just the periodic "You go, Girl!" pep talks. You've always believed in me, even when I didn't believe in myself. I know that without your support I would have never made it this far.

To Renea, thanks for pulling me out of the lab and onto a plane bound for Europe! It was an experience I'll never forget. Also, thanks for reminding me that the grass isn't always greener on the other side and to enjoy the experience of being in school.

Lance, I can't thank you enough for all the little things you've done over the last 3 years, but especially the last 3 months, to help me get through graduate school. Thank you for keeping me sane, for making me laugh, for weathering my moods, for fixing my computer issues, and for keeping me fed. Our relationship means more to me than I could ever put into words.

To Karen, from the good (?) old days in electronics lab to now, thanks for being a wonderful friend. I'll never forget our late night movies and brownie binges. Graduate school wouldn't have been the same without you.

I'd like to thank all my friends, especially the ladies in my women's group, for keeping me grounded, for lending a supportive ear, and for giving me great advice.

To my research advisor, Nancy, thanks for helping me grow into the person and the scientist that I am today. I've appreciated your guidance through the rough times in my research and in my life.

As for professional acknowledgements, I have many people to thank, but most especially my current and former lab mates, Xiang, Punya, Kristin, and Emily, for being colleagues and friends and for putting up with my incessant rambling. I'd like express my thanks to the Pielak and Spremulli labs for answering my general biochemistry questions and allowing me to borrow equipment. I also need to thank Dr. Redinbo and the Redinbo Lab for their assistance with the PXR project, especially Yuan Cheng who completed the DNA sequencing and was especially giving of his time and energy while teaching me molecular biology. My gratitude also goes to Dr. Erie, Susan Doyle, Dan Burke, and other members of the Erie lab for their assistance with AFM imaging. Lastly, I need to thank Dr. Edie Goldsmith of USC for her assistance with the DDR2 project.

TABLE OF CONTENTS

LIST OF TABLES

LIST OF FIGURES

LIST OF ABBREVIATIONS

α	incidence angle
α_c	critical angle
A488	Alexa Fluor® 488 C_5 maleimide
A514	Alexa Fluor® 514 carboxylic acid, succinimidyl ester
AF-2	activation factor 2 domain
AFM	atomic force microscopy
AMP	ampicillin
B-PXR	biotinylated PXR
BSA	bovine serum albumin
CCD	charge-coupled device
CHO	Chinese hamster ovary
CHLOR	chloramphenicol
CF	correction factor
CP	continuous photobleaching
d	depth of the evanescent wave
Da	Dalton
DBD	DNA binding domain
DDR(s)	discoidin domain receptor(s)
DDR1	discoidin domain receptor 1
DDR2	discoidin domain receptor 2
DI	deionized

dia	diameter
DMEM	Dulbecco's modified eagle medium
DNA	Deoxyribonucleic acid
DPPC	1,2-Dipalmitoyl-sn-Glycero-3-Phosphocholine
DS	discoidin
DTT	dithiothreitol
ε	molar extinction coefficient
ECD	extracellular domain
ECM	extracellular matrix
EDS	N-2-aminoethyl-3-aminopropyl-trimethoxysilane
EGFP	enhanced green fluorescent protein
EM-CCD	electron-multiplying charge coupled device
Fab	fragment antigen binding
FITC	fluorescein isothiocyanate
FC	fibrillar collagen
FCS	fluorescence correlation spectroscopy
FPLC	fast protein liquid chromatography
FRAP	fluorescence recovery after photobleaching
FRET	fluorescence resonance energy transfer
GFP	green fluorescent protein
G(t)	normalized autocorrelation function
HEK	human embryonic kidney
HEPES	(4-(2-hydroxyethyl)-1-piperazineethanesulfonic acid)

HCl	hydrochloride
HPLC	high performance liquid chromatograpy
HRP	horseradish peroxidase
IgG	Immunoglobulin G
IPTG	isopropyl-β-D-thiogalactopyranoside
K_d	dissociation constant
λ	wavelength
λ_0	wavelength of light in a vacuum
LB	Luria broth
LBD	ligand binding domain
LBP	ligand binding pocket
M	molarity (moles/liter)
mA	milliamp
MALS	multi-angle light scattering
MC	monomeric collagen
MEM	minimal essential media
MMP(s)	matrix metalloproteinase(s)
MW	molecular weight
MWCO	molecular weight cut off
n_1	refractive index of solid
n_2	refractive index of liquid
NAv	NeutrAvidin

NBD-DPPE	1,2-Dipalmitoyl-sn-Glycero-3-Phosphoethanolamine-N-(7-nitro-2-1,3-benzoxadiazol-4-yl) (Ammonium Salt)
Ni-DOGS-NTA	1,2-Dioleoyl-sn-Glycero-3-[N-(5-amino-1-carboxylpentyl)iminodiacetic acid)succinyl](nickel salt)
Ni-NTA	nickel nitrilotriacetic acid
NR	nuclear receptor
O	hydroxyproline
Ova	ovalbumin
PAGE	polyacrylamide gel electrophoresis
PBS	phosphate buffered saline
PMSF	phenylmethanesulphonylfluoride
POPC	1-Palmitoyl-2-Oleoyl-Glycero-3-Phosphocholine
PPAR	peroxisome proliferated-activator receptor
PVDF	polyvinyldiene fluoride
PXR	pregnane X receptor
RXRα	retinoid X receptor α
SDS	sodium dodecyl sulfate
SEC	size exclusion chromatography
SMRT	silencing mediator for retinoid and thyroid receptors
SPR	surface plasmon resonance
SRC-1	steroid receptor coactivator-1
SUVs	small unilamellar vesicles
TCEP	tris(2-carboxyethyl)phosphine

TCS	transferred cross-saturation
TEM	transmission electron microscope
TIR	total internal reflection
TIRF	total internal reflection fluorescence
Tris	2-amino-2-(hydroxymethyl)-1,3-propanediol

Chapter 1

Introduction

1.1 Overview

Measuring the interactions between individual biological molecules in a regulated pathway is key to understanding the overall functioning observed in cellular systems. Total internal reflection fluorescence microscopy (TIRF) is a powerful method for quantitatively measuring equilibrium thermodynamic and kinetic constants in biological systems. As such, this thesis presents work towards characterizing the molecular interactions of two biologically relevant systems, pregnane X receptor (PXR) and discoidin domain receptor 2 (DDR2), using TIRF microscopy, and presents a new TIRF method for studying protein diffusion in living cells. PXR is a member of the nuclear receptor family of ligand activated transcriptional factors and is believed to be responsible for the metabolism of over 50% of prescription drugs.[1] In Chapter 2, *in vitro* binding of PXR to one of its transcriptional co-activators, steroid receptor co-activator 1 (SRC-1), in the presence of the antibiotic rifampicin is examined using TIRF. DDR2 is a receptor tyrosine kinase that binds to collagens in the extracellular matrix (ECM), in turn leading to the upregulation of enzymes that degrade the ECM.[2] In Chapter 3, work towards using TIRF to study the binding of the extracellular domain of DDR2 to collagen type I is explained. Finally, a new method for studying diffusion of green fluorescent protein (GFP) in *Escherichia coli* through combination of TIRF with continuous photobleaching (CP) was developed and is described in Chapter 4. The theoretical basis and practical applications of TIRF microscopy and combinatory techniques is presented in this chapter, along with brief descriptions of other methods used in this thesis.

1.2 Total internal reflection fluorescence microscopy (TIRF)

Total internal reflection fluorescence microscopy (TIRF) was first introduced as a sensitive method for measuring the biophysical interactions of surface associated fluorescent molecules in the 1980's.[3] Nearly thirty years after its inception, TIRF is commonly used to measure surface densities of bound, fluorescent molecules and to image cell–substrate contacts.[4-6] TIRF is also used in conjunction with other techniques such as fluorescence recovery after photobleaching (FRAP), fluorescence resonance energy transfer (FRET), fluorescence correlation spectroscopy (FCS), and fluorescence polarization to measure surface binding kinetic rates and translational diffusion coefficients, molecular distance-dependent events, local fluorophore concentrations and translational mobilities, and population orientation distributions, respectively.[4, 7] Recently, TIRF has been combined with atomic force microscopy (AFM), and the combination has been shown to be a powerful technique for determining both the local structure and dynamics of biological molecules and assemblies.[8, 9]

In TIRF, an incident light beam propagates through a transparent solid, encounters a solid-liquid interface at an angle greater than the critical angle, and undergoes total internal reflection. The critical angle is defined as $\alpha_c = \sin^{-1}(n_2/n_1)$, where n_2 and n_1 are the refractive indices of the solution and solid, respectively ($n_1 > n_2$). An electromagnetic field called the evanescent wave is created and propagates parallel to the surface. The evanescent wave penetrates into the liquid medium, and the intensity decays exponentially with distance from the surface. The characteristic 1/e decay depth is defined by the equation $d = \lambda_0/[4\pi(n_1^2\sin^2\alpha - n_2^2)^{1/2}]$, where λ_0 is the wavelength of light in a vacuum, and $\alpha > \alpha_c$ is the incidence angle measured from the perpendicular to the

interface (Figure 1.1). The primary advantage of using evanescent illumination is that it selectively excites fluorescently labeled molecules at the surface-solution interface, even while they are in reversible equilibrium with the solution.[4, 7] For live cells immobilized at the solid-solution interface, only fluorophores located within or close to the plasma membrane are excited, which significantly reduces background fluorescence.[6] TIRF measurements are most commonly carried out on a fluorescence microscope but can also be performed in a conventional spectrofluorimeter adapted for evanescent excitation.[7, 10] Additionally, the use of microfluidics with fluorescence microscopy would allow for the automation of TIRF measurements.[11]

For fluorescence microscopy, the conventional method for generating TIR to date has been to use a prism, mounted to the stage of an inverted fluorescence microscope, through which a laser beam is loosely focused at the point of internal reflection. The prism is optically coupled, generally by using a refractive index matching liquid such as glycerol, to the surface of interest. A surface, solution and coverslip sandwich is formed using spacers. The evanescently excited fluorescence is collected with a microscope objective and is passed through a barrier filter (and usually a dichroic mirror) in the microscope to remove scattered radiation from the excitation source. The light is passed to a detector, which is typically a silicon avalanche photodiode or a photomultiplier. For some combinatorial TIRF techniques, a circular pinhole between 50 and 200 μm in diameter is placed in a confocal back-image plane to limit the area from which the fluorescence is collected before passing to the detector (Figure 1.2a). Alternatively, an optical fiber can be used in the same manner as a pinhole to limit the amount of light that reaches the detector.[12-15]

A second method for generating an evanescent field along a surface of interest is to use through-objective TIRF. As the name implies, internal reflection is generated by focusing a laser beam through the periphery of a high numerical aperture objective, which is directly coupled to the surface of interest, in a manner similar to epi-illumination (see section 1.3). The evanescently excited fluorescence is collected back through the same objective, passes through a dichroic mirror and barrier filter to remove scattered excitation light and is passed through a pinhole to the detector (Figure 1.2b). Additional focusing lenses may also be required to direct the light source through the objective at an angle great enough for TIRF. Recent work details the building and testing of in-house through-objective TIRF systems.[4, 12-14] Additionally, several manufacturers provide TIRF attachments for inverted microscopes; thus, through-objective TIRF is becoming the predominant configuration.

Three advantages of through-prism TIRF are the versatility of optical alignment, a lower background signal arising from the fact that the incident beam does not enter the interior of the microscope and (in many cases) lower cost. This geometry is also readily amenable to constructing evanescent interference patterns[15] and to the use of very high refractive index substrates.[16] Advantages of through-objective TIRF include sample-top accessibility, although through-prism configurations allowing such accessibility have also been designed,[17] decreased stray laser radiation in regions exterior to the microscope owing to the enclosed nature of the system, and the fact that slightly more fluorescence is collected through the higher refractive index side of the interface compared with the lower index side.[18] Also, through-objective TIRF often gives a slightly better image quality owing to proper matching of the objective with the coverslip and sample plane.

Theoretical treatments for the optical characteristics of the evanescent wave for both geometries have been presented.[19-21]

In TIRF, equilibrium constants are found by measuring the evanescently excited fluorescence intensity as a function of the bulk concentration of fluorescently labeled molecules in solution. The resulting signal arises from two sources—from fluorescently labeled molecules that bind to the surface and from fluorescently labeled molecules that are not associated with the surface but diffuse within the evanescent wave. The latter creates a background signal that increases linearly with the bulk concentration of fluorophores in solution, therefore requiring the use of negative controls to account for this phenomenon. Negative controls are created either by removing surface binding sites or by blocking binding to the surface. The background signal is then subtracted from the original curve before obtaining the equilibrium binding constant (Figure 1.3).[22]

While equilibrium binding constants can be directly measured with TIRF, measuring kinetic rates for biological systems requires conjunction with other techniques, such as FCS or FRAP. In TIR-FRAP, a high powered laser beam is used to rapidly bleach fluorescent molecules that are in equilibrium at the solid-solution interface. After bleaching, a low power beam is then used to monitor fluorescence recovery, which arises as photobleached molecules at the solid-solution interface desorb from the surface and are replaced with unbleached molecules from the solution or that diffuse from surrounding, non-illuminated surface areas. The rate and shape of the fluorescence recovery contains information about the surface association and dissociation rate constants, diffusion coefficients on the surface, and solution diffusion coefficients (Figure 1.4). TIR-FRAP has been used *in vitro* to examine protein binding to phospholipid

bilayers and has been used in live cell work to monitor kinetic rates for the interactions of intracellular and extracellular proteins with the plasma membrane.[5] When used in combination with an imaging detector, spatial maps of dissociation rates from intact cell membranes for a fluorescent molecule can be generated and used to probe surface inhomogeneity in cells.[23]

In FCS, temporal fluctuations in fluorescence are correlated to obtain information about the processes giving rise to the observed fluctuations, when the number of molecules in the observation volume is small. The fluctuations typically arise from molecules diffusing into and out of the observation region or from molecules undergoing transitions between different fluorescent states. FCS is commonly used to measure equilibrium binding constants, diffusion coefficients, kinetic rate constants and oligomerization.[24-26] In combination, TIR-FCS is a tool for elucidating events that occur at or very close to surface-solution interfaces, such as the kinetic rate constants that describe the reversible association of fluorophores with the interface, local fluorophore concentrations and local translational mobilities.[7, 27] These parameters can be extracted from the magnitude and the rate and shape of the decay of the normalized fluorescence fluctuation autocorrelation function G(t).[28-32] While TIR-FRAP is useful for measuring kinetic rates in systems with characteristic off rates on the order of 1 sec to 30 min, TIR-FCS requires faster characteristic rates, on the order of 1 ms to 1 sec, to generate correlation functions with adequate signal to noise ratios. It should be noted that the characteristic time range for each technique is limited by instrumental and software time resolution and may vary for different instrumental set-ups.

In recent years, the commercialization of through-objective TIRF microscopes, combined with improvements in data acquisition rates in electron-multiplying charge coupled device (EM-CCD) cameras, has lead to a rapid rise in use of TIRF in single-molecule detection and imaging *in vivo* of dynamic membrane processes. The advantages of imaging with TIRF include improved background as compared to traditional fluorescence microscopy, precise axial tracking, applicability to multi-color and multi-photon excitation, and the ability to image cells longer due to higher survival rates achieved by using low excitation intensities.[4, 6] Furthermore, TIRF has been shown to be compatible with standard epifluorescence, bright field, dark field, or phase contrast illumination and can be switched back and forth to obtain more information about the biological systems under study. Unlike confocal microscopy, TIRF lacks the ability to probe deep within thick cells, but will likely continue to grow in popularity due to its ability to be adapted to standard microscope optics.[4]

1.3 Epifluorescence Microscopy

Epifluoresence refers to a general technique for stimulating and collecting fluorescence of a sample using the same lens. For epi-illumination, a light source is reflected off a dichroic mirror through a microscope objective which focuses the light into a spot on the sample. The emitted fluorescence is then collected back through the same objective, is passed through the dichroic mirror to a barrier filter that allows only selected wavelengths of light to pass, and is reflected onto a detector, typically a CCD camera (Figure 1.5). Reflected excitation light that is collected by the objective will not be transmitted through the dichroic mirror and barrier filter. Epifluorescence is

commonly used for imaging of biological samples labeled with fluorescent dyes and is the illumination method used in wide field, through-objective TIRF, and confocal fluorescence imaging. Epifluorescence is used in Chapter 3 to image collagen films on fused-silica substrates.

1.4 Continuous Photobleaching

Continuous photobleaching (CP) was first developed in the 1980's as alternative method to FRAP for studying the translation diffusion of lipids in model systems and live cells. In CP, an excitation source is used to bleach fluorescence molecules in a sample, and the fluorescence decay is monitored as a function of time. The rate and the shape of the fluorescence decay can then be analyzed to extract diffusion coefficients for biological samples. As high powered laser flashes and detector protection intervals are not required for CP, the instrumental set-up is also less complicated than for FRAP. However, there is a higher probability of photochemical effects occurring in CP, since the intensity used to excite and bleach fluorophores in CP is higher than the intensity used to monitor fluorescence recovery in FRAP, and data interpretation can be complicated.[33, 34] A novel method that combines CP with TIR, which allows for diffusion to be measured in structures only slightly larger than optical resolution, is described in chapter 4.[35]

1.5 Atomic Force Microscopy

Atomic force microscopy (AFM) is a scanning probe technique, which was invented in 1986,[36] that is used to study nonconductive, soft, and live biological samples. AFM is used to image surface topography of samples and to measure intermolecular and

intramolecular forces between interacting molecules.[37-40] In imaging AFM, a sharp tip (typically made of silicon or silicon nitride), which is attached to a spring loaded cantilever, is rastered across the surface of sample. Interactions with features on the surface cause the tip to move up or down with the contour of the surface and are detected using a laser beam, which is reflected off the back of the cantilever and onto a position sensitive photodiode. A piezoelectric tube connected to a feedback mechanism is used to translate the sample in the X, Y, and Z directions (Figure 1.6). An image of the surface is then generated by plotting Z direction movements as a function of X-Y positions.[39, 40] The spatial resolution of the measurements is related to the radius of curvature of the tip apex, which is minimized (typically 2 to 50 nm) for best resolution.[40] AFM can be conducted in air, aqueous solution, or under vacuum. Due to its widespread use, many AFM scanning techniques have been developed,[40] and the two most commonly used modes are contact and intermittent-contact or tapping mode.

AFM is a powerful tool for probing biological systems either in air, under near physiological conditions, or on live cells and has been used to study biological systems from the single molecule to cellular level. AFM is advantageous in that biological samples can be studied in buffered solutions at ambient temperature without the need for fixing, staining, or labeling of samples.[37, 38] For biomembranes imaged in aqueous environments, lateral resolution on the order of several nanometers and height resolution of 0.1 nm have been achieved with image acquisition on the order of 1 minute. However, if biological molecules are flexible or are loosely attached to the surface of interest, the AFM tip can act as a "molecular broom," sweeping aside biological components as it scans the surface, potentially damaging the sample. To overcome this limitation, tapping

mode is commonly used as it exerts lower forces on the sample.[37] In tapping mode, the cantilever is oscillated by an additional piezo such that the tip intermittently touches or taps the surface, instead of continuously being in hard contact with the surface as in contact mode.[40] Traditionally, AFM has also suffered from slow acquisition times, which prevented real time monitoring of biological processes and observation of events that occur on the millisecond time scale,[39] but in recent years AFM microscopes with video rate imaging have been introduced.[41, 42] AFM is used in Chapter 3 to image collagen films on glass substrates.

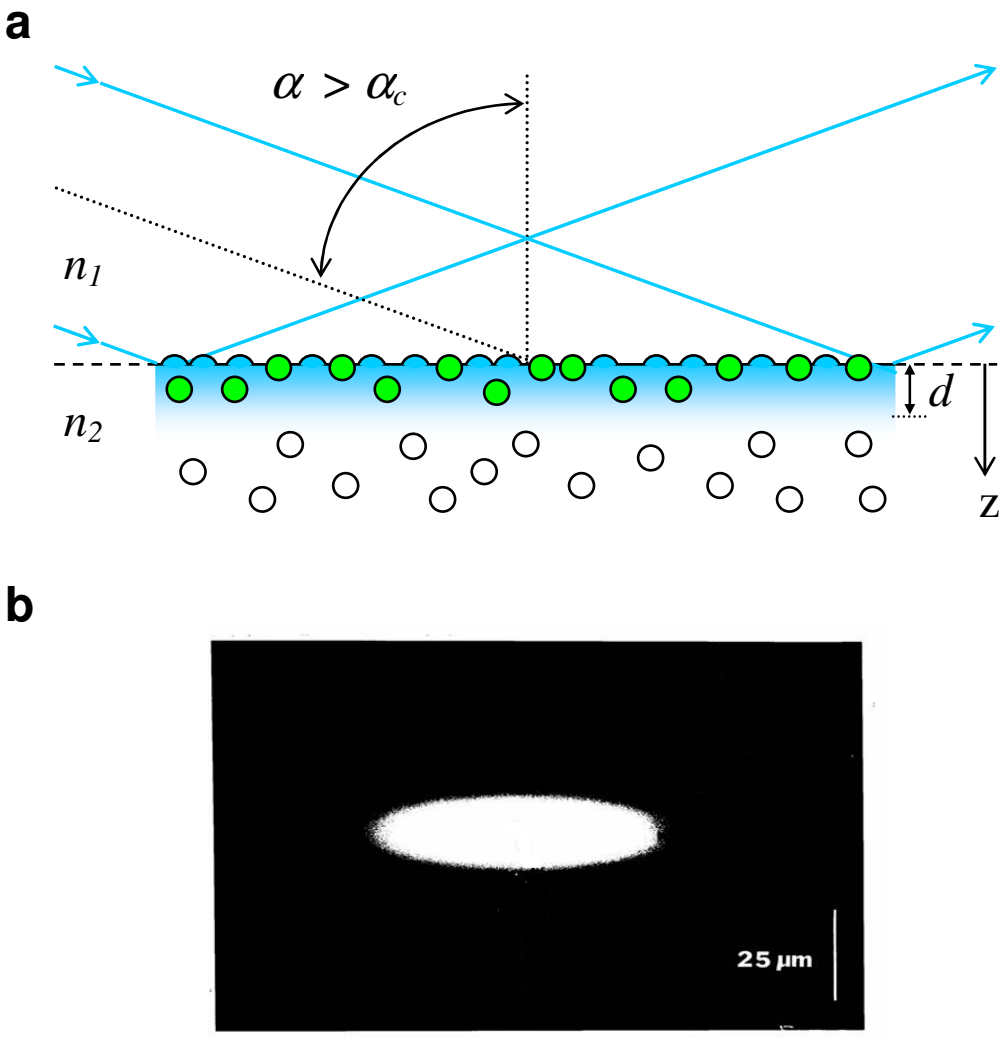

Figure 1.1 Total Internal Reflection. (a) Total internal reflection is generated when an incident light beam propagates through a transparent solid and encounters a planar solid-solution interface at an angle greater than the critical angle α_c, creating an electromagnetic field that excites fluorescent molecules near the solid-solution interface (green circles). The evanescent wave decays exponentially with distance d (shown in blue) from the surface, and fluorescent molecules outside of this field are not excited (clear circles). For fused silica and glass, $n_1 \approx 1.5$, $n_2 \approx 1.3$ and $d \approx 0.1$ µm. (b) For through-prism TIR, if the laser beam is loosely focused at the point of internal reflection, the resulting evanescent field along the surface has an elliptical Gaussian shape.

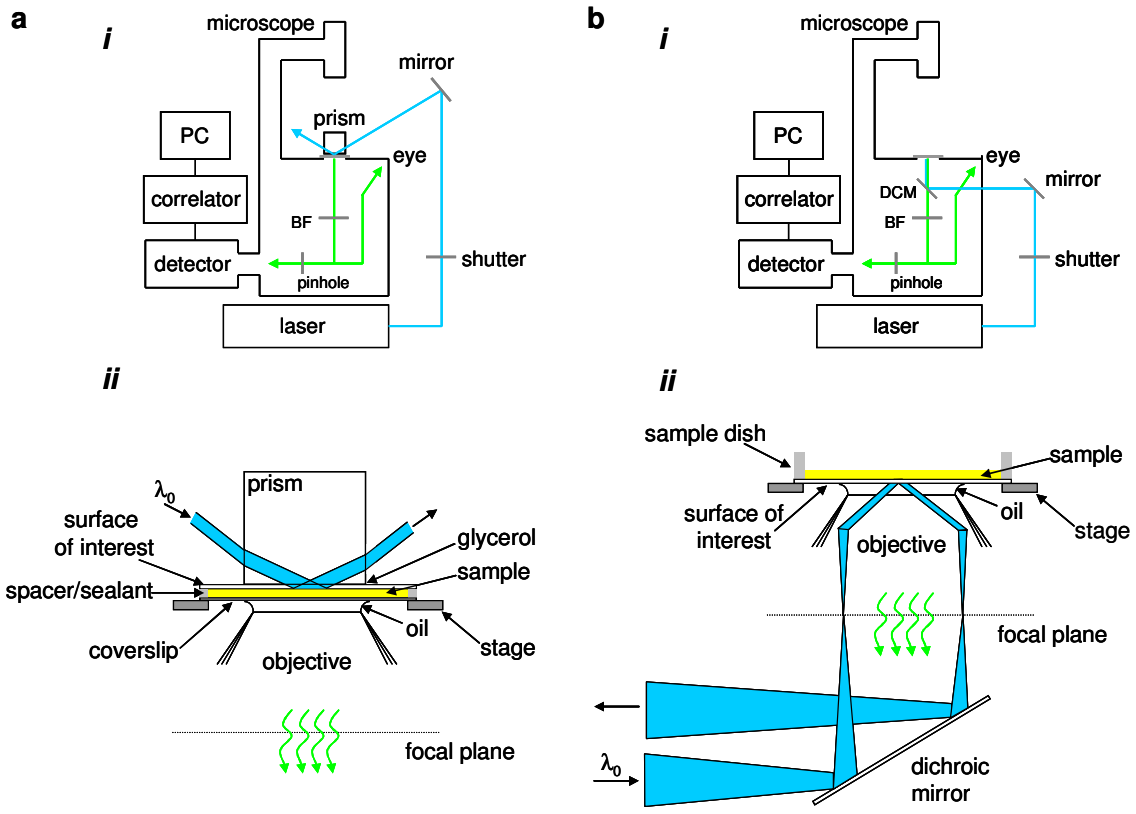

Figure 1.2 TIRF Apparatus. (a) Through-Prism TIRF. (*i*) A laser beam is totally internally reflected into a sample through a prism that is mounted onto the stage of an inverted microscope. The evanescently excited fluorescence is collected through a microscope objective and passed through a barrier filter (BF) to remove scattered evanescent light. The light is passed through a circular pinhole (optional), which is placed in a confocal back-image plane, before reaching the detector. The resulting signal is processed using a PC with an optional correlator card. (*ii*) The sample is composed of a transparent planar substrate of interest, solution and coverslip sandwich separated by spacers, and is mounted onto an inverted microscope such that the prism is optically coupled with glycerol to the substrate (usually fused silica). Internal reflection is generated by focusing a laser beam through the prism onto the sample and the evanescently excited fluorescence is collected through the objective. (b) Through-objective TIRF. (*i*) A laser beam is directed through the microscope, reflected upwards using a dichroic mirror (DCM) and focused through the periphery of a high numerical aperture objective, which is directly coupled to the surface of interest, to generate internal reflection. The evanescently excited fluorescence is collected back through the same objective, passes through a barrier filter (BF) to remove excitation light and passes through a pinhole (optional) before reaching the detector. The resulting signal is acquired using a PC. (*ii*) The transparent planar substrate of interest is coupled to a high numerical aperture objective using immersion oil. Total internal reflection is generated by focusing the laser through the periphery of a high numerical objective onto the substrate and the evanescently excited fluorescence is collected back through the objective and filter as described b(*i*).

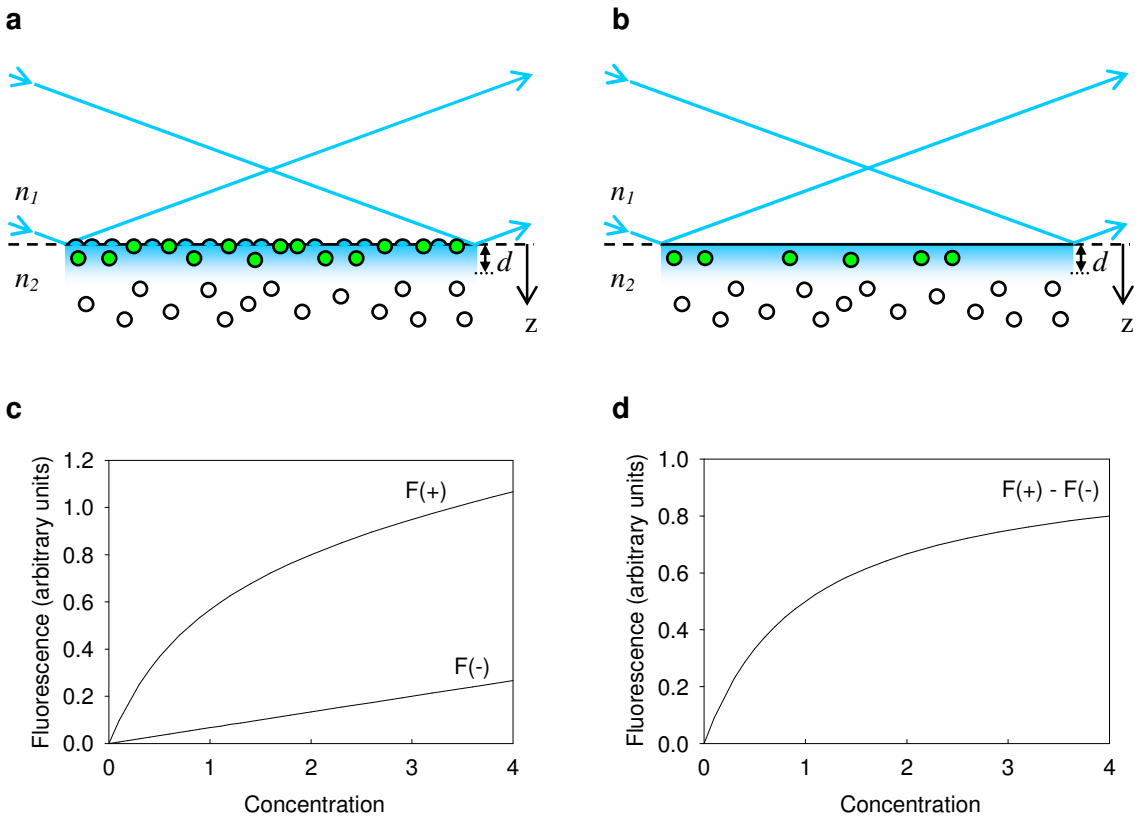

Figure 1.3 Equilibrium Binding Measured with TIRF. (a) Fluorophores (clear and green circles) are in equilibrium between surface binding sites and solution. Fluorophores within the evanescent wave, which are diffusing near the surface or are bound to the surface, are evanescently excited (green circles) and give rise to a signal, F(+). (b) Negative controls are generated by removing the surface binding sites. Therefore, the resulting evanescently excited fluorescence, F(-), arises only from fluorophores that are not surface associated, but are diffusing within the evanescent wave. (c) The fluorescence intensities for F(+) and F(-) are plotted as a function of the bulk concentration of fluorescent molecules in solution, and (d) F(-) is subtracted from F(+) to obtain an accurate equilibrium binding constant for the surface-associated binding.

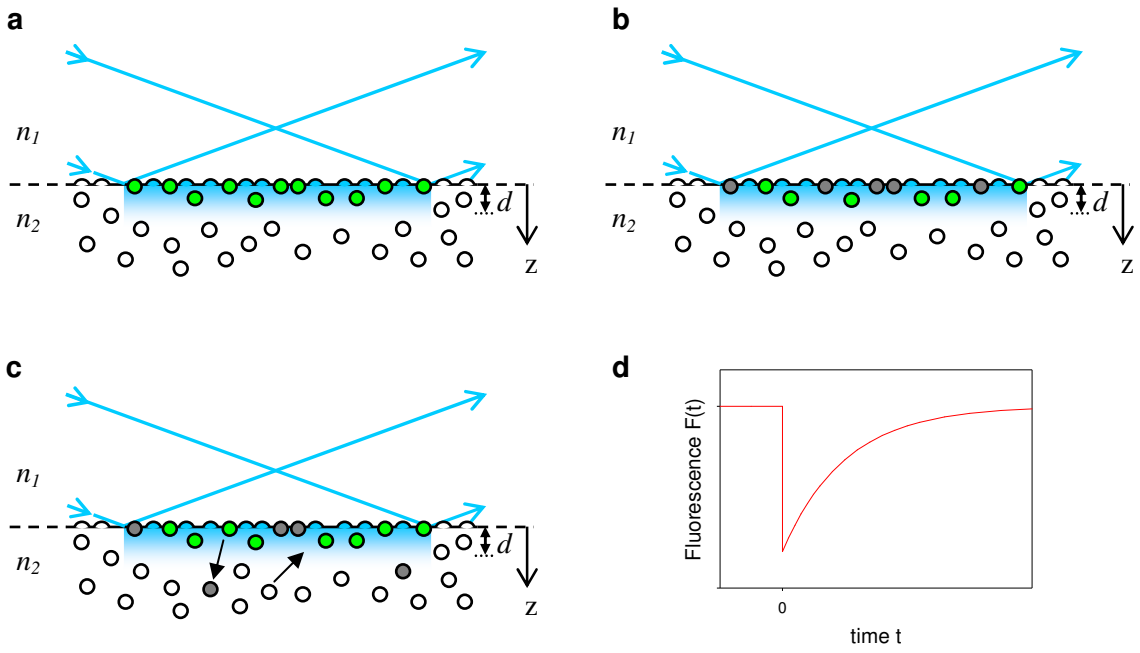

Figure 1.4 TIR-FRAP. In TIR-FRAP, (a) before bleaching (t<0), fluorescent molecules (green and clear circles) are in equilibrium between surface binding sites and the solution, and those at or near the surface are evanescently excited (green circles), giving rise to a fluorescence signal. (b) At t=0, a short, high intensity laser pulse is applied to the sample such that a fraction of the surface-associated fluorescent molecules within the evanescent wave are irreversibly photobleached (gray circles), reducing the fluorescence signal. (c) At t>0, surface-associated, photobleached molecules begin to desorb from the surface and are replaced with unbleached fluorophores from solution or from the surrounding non-illuminated area, and the fluorescence signal begins to recover. (d) By fitting the fluorescence recovery curve to appropriate theoretical forms, information about the surface association and dissociation constants and diffusion coefficients on the surface can be obtained from the rate and shape of the curve.

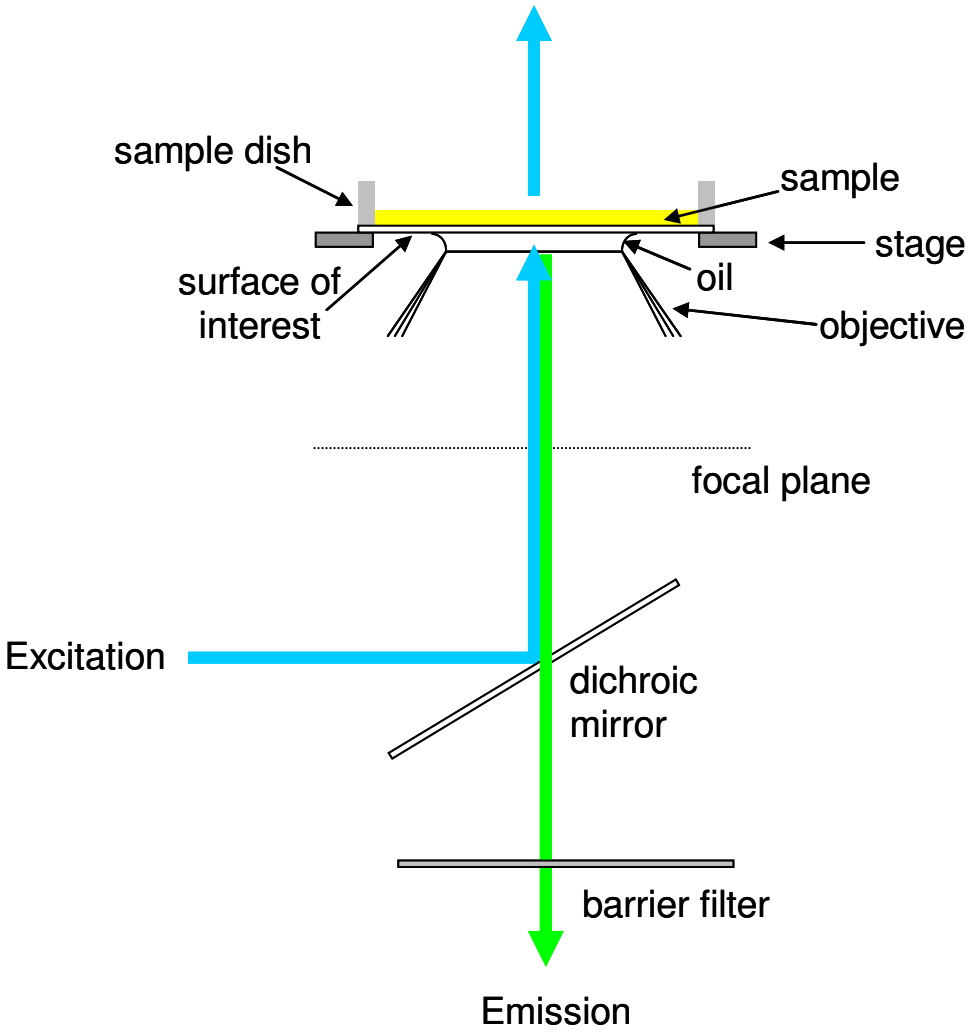

Figure 1.5 Epifluorescence Illumination. In epi-illumination, excitation light (blue) is passed through a microscope port, reflected off a dichroic mirror through an objective which focuses the light onto a sample, giving rise to fluorescence (green). The emitted fluorescence is then collected through the objective and passes through the dichroic mirror and barrier filter, which removes reflected and scattered excitation light, to an imaging detector.

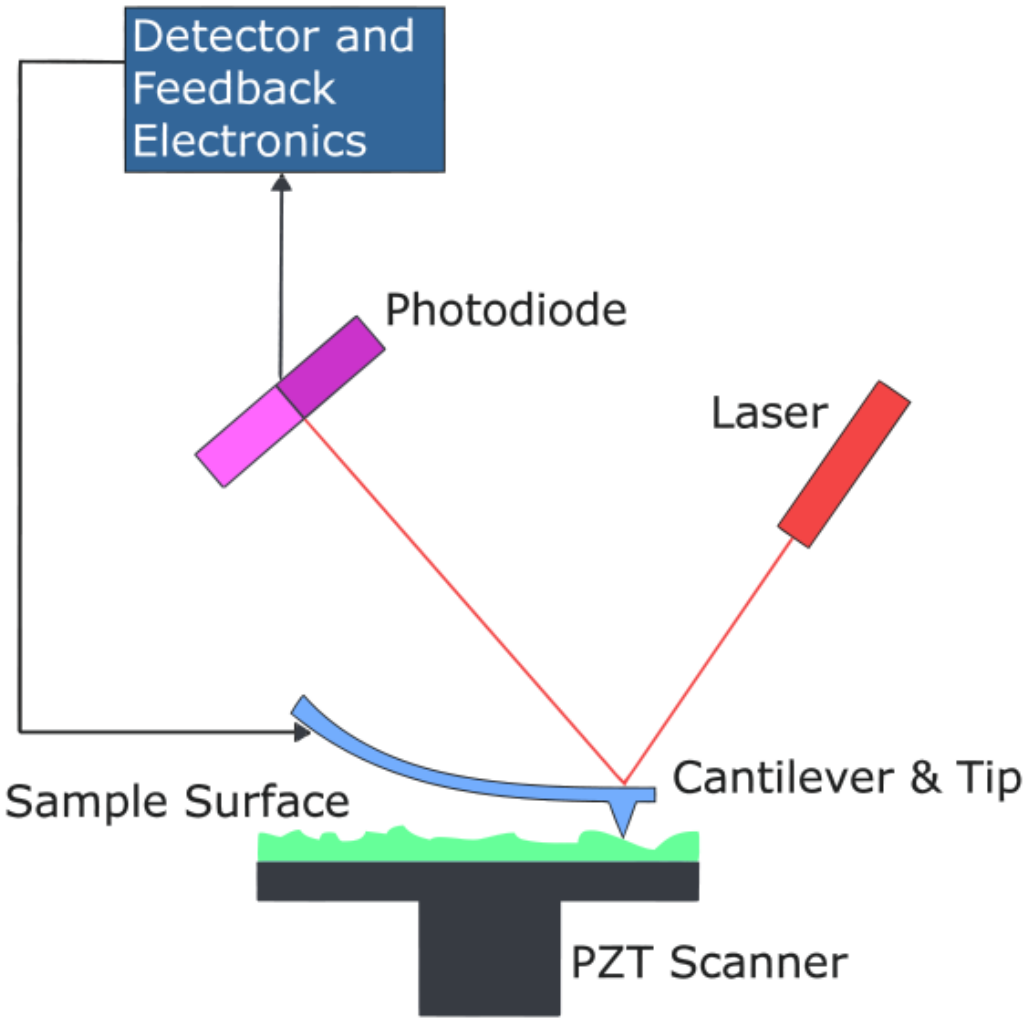

Figure 1.6 AFM Apparatus. In AFM, a silicon or silicon nitride tip attached to a cantilever is rastered over the surface of a sample and encounters surface features that cause deflections of the tip. These deflections are monitored using a laser beam that is reflected off the cantilever onto a position-sensitive photodiode. A feedback loop from the detector keeps either the force between the sample and the tip constant or the distance between the tip and the sample constant, by changing the Z position of the surface or tip, using a piezoelectric (PZT) scanner, which also controls the X and Y positions. (Image released to Public Domain, 2008)

1.6 References

1. Watkins, R. E.; Wisely, G. B.; Moore, L. B.; Collins, J. L.; Lambert, M. H.; Williams, S. P.; Willson, T. M.; Kliewer, S. A.; Redinbo, M. R., The human nuclear xenobiotic receptor PXR: structural determinants of directed promiscuity. *Science* **2001,** *292*, 2329-2333.

2. Vogel, W. F.; Abdulhussein, R.; Ford, C. E., Sensing extracellular matrix: an update on discoidin domain receptor function. *Cellular Signalling* **2006,** *18*, 1108-1116.

3. Axelrod, D., Cell surface contacts illuminated by total internal reflection fluorescence. *The Journal of Cell Biology* **1981,** *89*, 141-145.

4. Axelrod, D., Total internal reflection fluorescence microscopy. In *Biophysical Tools for Biologists, Vol 2: In Vivo Techniques*, 2008; Vol. 89, pp 169-221.

5. Thompson, N. L.; Pero, J. K., Total internal reflection fluorescence microscopy: applications in biophysics. In *Fluorescence Spectroscopy in Biology Advanced Methods and their Applications to Membranes, Proteins, DNA, and Cells*, Hof, M.; Hutterer, R.; Fidler, V., Eds. Springer-Verlag: Berlin Heidelberg, 2005; Vol. 3, pp 79-103.

6. Groves, J. T.; Parthasarathy, R.; Forstner, M. B., Fluorescence imaging of membrane dynamics. *Annual Review of Biomedical Engineering* **2008,** *10*, 311-338.

7. Thompson, N. L.; Pero, J. K., Total internal reflection-fluorescence correlation spectroscopy. In *Reviews in Fluorescence 2006*, Geddes, C.; Lakowicz, J., Eds. Kluwer Academic/Plenum Press: New York, 2006; Vol. 3, pp 215-237.

8. Oreopoulos, J.; Yip, C. M., Combined scanning probe and total internal reflection fluorescence microscopy. *Methods* **2008,** *46* (1), 2-10.

9. Shaw, J. E.; Oreopoulos, J.; Wong, D.; Hsu, J. C. Y.; Yip, C. M., Coupling evanescent-wave fluorescence imaging and spectroscopy with scanning probe microscopy: challenges and insights from TIRF-AFM. *Surface and Interface Analysis* **2006,** *38* (11), 1459-1471.

10. Thompson, N. L.; Pearce, K. H.; Hsieh, H. V., Total internal fluorescence microscopy-application to substrate-supported planar membranes. *European Biophysics Journal with Biophysics Letters* **1993,** *22* (5), 367-378.

11. Holden, M. A.; Cremer, P. S., Microfluidic tools for studying the specific binding, adsorption, and displacement of proteins at interfaces. *Annual Review of Physical Chemistry* **2005,** *56*, 369-387.

12. Hassler, K.; Anhut, T.; Rigler, R.; Gosch, M.; Lasser, T., High count rates with total internal reflection fluorescence correlation spectroscopy. *Biophysical Journal* **2005,** *88* (1), L1-L3.

13. Hassler, K.; Leutenegger, M.; Rigler, P.; Rao, R.; Rigler, R.; Gosch, M.; Lasser, T., Total internal reflection fluorescence correlation spectroscopy (TIR-FCS) with low background and high count-rate per molecule. *Optics Express* **2005,** *13* (19), 7415-7423.

14. Ohsugi, Y.; Saito, K.; Tamura, M.; Kinjo, M., Lateral mobility of membrane-binding proteins in living cells measured by total internal reflection fluorescence correlation spectroscopy. *Biophysical Journal* **2006,** *91* (9), 3456-3464.

15. Leutenegger, M.; Blom, H.; Widengren, J.; Eggeling, C.; Gosch, M.; Leitgeb, R. A.; Lasser, T., Dual-color total internal reflection fluorescence cross-correlation spectroscopy. *Journal of Biomedical Optics* **2006,** *11* (4).

16. Thompson, N. L.; Steele, B. L., Total internal reflection with fluorescence correlation spectroscopy. *Nature Protocols* **2007,** *2*, 878-890.

17. Huang, Z. P.; Pearce, K. H.; Thompson, N. L., Translational diffusion of bovine prothrombin fragment 1 weakly-bound to supported planar membranes-measurement by total internal-reflection with fluorescence pattern photobleaching recovery. *Biophysical Journal* **1994,** *67* (4), 1754-1766.

18. Starr, T. E.; Thompson, N. L., Formation and characterization of planar phospholipid bilayers supported on TiO2 and SrTiO3 single crystals. *Langmuir* **2000,** *16* (26), 10301-10308.

19. Axelrod, D., Total internal reflection fluorescence microscopy in cell biology. *Traffic* **2001,** *2* (11), 764-774.

20. Steyer, J. A.; Almers, W., A real-time view of life within 100 nm of the plasma membrane. *Nature Reviews Molecular Cell Biology* **2001,** *2* (4), 268-275.

21. Burghardt, T. P.; Ajtai, K.; Borejdo, J., In situ single-molecule imaging with attoliter detection using objective total internal reflection confocal microscopy. *Biochemistry* **2006,** *45* (13), 4058-4068.

22. Burghardt, T. P.; Thompson, N. L., Evanescent intensity of a focused gaussian light-beam undergoing total internal-reflection in a prism. *Optical Engineering* **1984,** *23* (1), 62-67.

23. Mattheyses, A. L.; Axelrod, D., Direct measurement of the evanescent field profile produced by objective-based total internal reflection fluorescence. *Journal of Biomedical Optics* **2006,** *11* (1).

24. Thompson, N. L.; Axelrod, D., Biochemical kinetics of protein surface binding studied at equilibrium with total internal-reflection fluorescence. *Biophysical Journal* **1983,** *41* (2), A305-A305.

25. Sund, S. E.; Axelrod, D., Actin dynamics at the living cell submembrane imaged by total internal reflection fluorescence photobleaching. *Biophysical Journal* **2000,** *79* (3), 1655-1669.

26. Gösch, M.; Rigler, R., Fluorescence correlation spectroscopy of molecular motions and kinetics. *Advanced Drug Delivery Reviews* **2005,** *57* (1), 169-190.

27. Thompson, N. L., Fluorescence correlation spectroscopy. In *Topics in Fluorescence Spectroscopy*, Lakowicz, J., Ed. Plenum Press: 1991; Vol. 1, pp 337-378.

28. Rigler, R.; Elson, E. L., *Fluorescence correlation spectroscopy: theory and applications*. Springer: Berlin, 2001.

29. Thompson, N. L.; Wang, X.; Navaratnarajah, P., Total internal reflection with fluorescence correlation spectroscopy: applications to substrate-supported planar membranes. *Journal of Structural Biology* **2009,** *In press*.

30. Pero, J. K.; Haas, E. M.; Thompson, N. L., Size dependence of protein diffusion very close to membrane surfaces: measurement by total internal reflection with fluorescence correlation spectroscopy. *Journal of Physical Chemistry B* **2006,** *110* (22), 10910-10918.

31. Lieto, A. M.; Cush, R. C.; Thompson, N. L., Ligand-receptor kinetics measured by total internal reflection with fluorescence correlation spectroscopy. *Biophysical Journal* **2003,** *85* (5), 3294-3302.

32. Lieto, A. M.; Thompson, N. L., Total internal reflection with fluorescence correlation spectroscopy: nonfluorescent competitors. *Biophysical Journal* **2004,** *87* (2), 1268-1278.

33. Starr, T. E.; Thompson, N. L., Total internal reflection with fluorescence correlation spectroscopy: combined surface reaction and solution diffusion. *Biophysical Journal* **2001,** *80* (3), 1575-1584.

34. Thompson, N. L., Surface binding rates of non-fluorescenct molecules may be obtained by total internal-reflection with fluorescence correlation spectroscopy. *Biophysical Journal* **1982,** *38* (3), 327-329.

35. Brünger, A.; Peters, R.; Schulten, K., Continuous fluorescence microphotolysis to observe lateral diffusion in membranes. Theoretical methods and applications. *Journal of Chemical Physics* **1985,** *82*, 2147-2160.

36. Peters, R.; Brünger, A.; Schulten, K., Continuous fluorescence microphotolysis: a sensitive method for study of diffusion processes in single cells. *Proceedings of the National Academy of Sciences of the United States of America* **1981,** *78*, 962-966.

37. Slade, K.; Steele, B. L.; Pielak, G.; Thompson, N. L., Quantifying green fluorescent protein diffusion in *Escherichia coli* by using continuous photobleaching with evanescent illumination. *Journal of Physical Chemistry B* **2009,** *113*, 4837-4845.

38. Binnig, G.; Quate, C.; Gerber, C., Atomic force microscopy. *Physical Review Letters* **1986,** *56*, 930-933.

39. Goksu, E. I.; Vanegas, J. M.; Blanchette, C. D.; Lin, W. C.; Longo, M. L., AFM for structure and dynamics of biomembranes. *Biochimica Et Biophysica Acta-Biomembranes* **2009,** *1788* (1), 254-266.

40. Muller, D. J.; Krieg, M.; Alsteens, D.; Dufrene, Y. F., New frontiers in atomic force microscopy: analyzing interactions from single-molecules to cells. *Current Opinion in Biotechnology* **2009,** *20* (1), 4-13.

41. Yang, Y.; Wang, H.; Erie, D. A., Quantitative characterization of biomolecular assemblies and interactions using atomic force microscopy. *Methods* **2003,** *29* (2), 175-187.

42. Frétigny, C., Atomic force microscopy. In *Nanoscience: Nanotechnologies and Nanophysics*, Dupas, C.; Houdy, P.; Lahmani, M., Eds. Springer-Verlag: Berlin Heidelberg, 2007.

43. Ando, T.; Uchihashi, T.; Fukuma, T., High-speed atomic force microscopy for nano-visualization of dynamic biomolecular processes. *Progress in Surface Science* **2008,** *83* (7-9), 337-437.

44. Humphris, A. D. L.; Miles, M. J.; Hobbs, J. K., A mechanical microscope: High-speed atomic force microscopy. *Applied Physics Letters* **2005,** *86* (3).

Chapter 2

Quantitative Studies of the Ligand-Dependent Binding of Pregnane X Receptor to Steroid Receptor Coactivator 1

2.1 Introduction

Pregnane X receptor is a member of the nuclear receptor (NR) family of ligand activated transcription factors that regulate gene expression. These receptors bind to DNA, recruit transcriptional coregulators in a ligand dependent manner, and activate the production of proteins that metabolize exogenous (xenobiotic) and endogenous chemicals.[43-45] Unlike many other nuclear receptors that bind with high specificity to a particular set of ligands, PXR is a promiscuous receptor that binds to ligands of various sizes, ranging from 200 to 800 Da, with a wide array of structural diversity, including prescription drugs, herbal medicines, dietary supplements, environmental pollutants, and endobiotics.[46, 47] Upon activation through ligand binding, PXR induces the expression of gene products involved in the uptake, metabolism, and elimination of xenobiotic and endobiotic compounds.[45, 48]

PXR regulates genes involved in all phases of drug metabolism, including the cytochromes P450 (CYP450s), heme-containing monooxygenases involved in phase I metabolism; phase II enzymes such as glutathione-S-transferases (GSTs), UDP-glucuronoslytransferases (UGTs), and sulfotransferases (SULTs); and phase III transporters such as the multidrug resistance associated proteins-1 and -2 (MDR1 and MDR2) and the organic anion transporter polypeptide 2 (OATP2). Furthermore, PXR has been termed the master regulator of CYP3A4 gene expression, which mediates the metabolism of over 50% of prescription drugs in humans.[44, 45] In humans, PXR is expressed mainly in the liver and intestines. PXR also regulates other pathways including bile acid detoxification and cholestasis, adrenal steroid homeostasis, lipid metabolism, inflammation and inflammatory bowel disease, and bone homeostasis.[46]

The complete extent of gene regulation by PXR is still being determined, as recent studies have implicated new genes previously not classified as PXR targets.[49, 50]

The general structure of PXR is similar to that of other nuclear receptors and contains an N-terminal ligand-independent transcriptional factor (AF-1) domain followed by a highly conserved DNA binding domain (DBD), characterized by two C4-type zinc fingers. A flexible hinge region connects the DBD to the ligand binding domain (LBD), which in addition to the ligand binding pocket (LBP) contains hetero- and homo-dimerization motifs and the ligand-dependent transcriptional regulation docking site, known as activation factor 2 (AF-2). PXR heterodimerizes with its obligate DNA binding partner, retinoid X receptor α (RXRα), and binds to a variety of xenobioitic recognition elements (direct repeats DR-3, DR-4, DR-5 and everted repeats ER-6 and ER-8), in the promoter regions of target genes.[44, 45] Studies with human PXR indicate sublocalization in the nucleus even in the absence of activating ligand,[50-52] however; localization may be species dependent, as studies in mice have shown that PXR is localized in the cytoplasm and translocates to the nucleus after receptor activation.[51, 53]

In the absence of ligand, the AF-2 domain of PXR preferentially interacts with corepressors, specifically small heterodimer partner (SHP) and silencing mediator for retinoid and thyroid receptors (SMRT),[50] which contain LXXX(L/I)XXX(L/I) or (L/V)XX(I/V)I motifs, where I is isoleucine, L is leucine, V is valine, and X is any amino acid. The corepressor serves as a platform for the recruitment of additional transcriptional repressors, such as histone deacetylases. Agonist binding in the ligand binding pocket of the receptor switches PXR to an active state by inducing a conformational change in the AF-2 domain that releases the corepressor. Coactivators

that contain the LXXLL motif, such as members of the p160 family of transcriptional activators, which includes steroid receptor coactivator-1 (SRC-1) and glucocorticoid receptor interacting protein-1 (Grip-1), are recruited along with basal transcriptional machinery, ultimately leading to gene expression. This two-state model for transcriptional activation is a common paradigm for ligand-dependent activation of nuclear receptors and is depicted in Figure 2.1. However, the discovery of corepressors that interact with agonist-bound nuclear receptors may require refinement of this model.[54, 55]

The overall fold of the ligand binding domain of PXR is similar to other NRs and consists of a three-layer "α-helical sandwich" that encloses the large, spherical binding-pocket of PXR (Figure 2.2). Unique to PXR, the LBD contains an insert of 50-60 amino acid residues located between α1 and α3 that creates an extended, five-stranded anti-parallel β-sheet adjacent to the LBP (other NR LBDs contain only 2 or 3-stranded β-sheets) and creates a novel α2 fold along the underside of the LBP. Residues 178-191 of the insert are disordered in PXR LBD crystal structures, implying structural mobility. Additionally, the binding pocket of PXR is much larger (on the order of 2 to 3 times) than other NRs and contains hydrophobic and hydrophilic residues that interact with bound ligands. As in other NR-LBDs, the PXR LBD ends with a short helix (termed αAF or α12) that is critical to the AF-2 region and thus coregulator binding.

The observed promiscuity of PXR ligand binding is due to structural mobility in the LBD that allows the binding pocket to expand and contract. Comparison of the crystal structures of apo-PXR-LBD[1] with those of bound to rifampicin,[56] to hyperforin,[57] to SR12813[1] and to the combination of SR12813 and SRC-1 coactivator peptide[58] reveals

that three main regions become disordered to create the space necessary to accommodate large agonists. These regions are the flexible loop formed from residues 229 to 235, a hydrophobic loop formed from residues 309 to 321 that folds into α6 in some structures, and residues 192 to 210 that form a pseudo-helix or fold into α2, a "*bona fide* helix", depending on the bound agonist. These structures reveal that the region comprising the α2 helix directly contacts bound ligands and changes its conformation to accommodate specific ligands. Additionally, α2 is believed to act as "trapdoor" to the ligand binding pocket, dropping out of the way to provide a dynamic entry and exit way to the LBP of PXR. The crystal structure of SR12813 ligand alone showed three distinct binding conformations within the LBP, suggesting that the LBD of PXR "breathes" to allow the ligand to find the optimal binding orientation, and binding of the SRC-1 coactivator locks the ligand into a single conformation, stabilizing the interaction.[44] Interestingly, the crystal structure of the LBD of PXR bound to the endobioitic ligand 17β-estradiol (272 Da) showed that 1000 $Å^3$ of the ligand binding pocket was unoccupied.[59]

For many studies including in crystal structures, small α-helical peptides that contain the LXXLL or LXXX(L/I)XXX(L/I) motifs, termed NR boxes or interaction domains (ID), observed in coactivators and corepressors, respectively, are used instead of the corresponding full length proteins. Transcriptional coregulators generally contain several interaction domains, and NRs exhibit preferential binding to a particular ID within the coregulator.[60] The crystal structure of PXR bound to ID2 of SRC-1 reveals that the coactivator binding motif contains a two turn α-helix, which forms a charge clamp with the AF-2 region of PXR, connected to a second short, kinked helix that is perpendicular to the first.[44] The corepressor motif contains a three turn α-helix that

interacts with the corepressor docking site, located in NRs on α helices 3 through 5. The coregulator binding sites overlap each other, and ultimately the position of the αAF/α12 helix determines whether the coactivator or corepressor binds to the LBD of the NR.[55]

Crystal structure data have also revealed that PXR forms a novel homodimer at an interface created by the extended β-sheet observed in the LBD domain of PXR.[58] The β1' strands from each monomer associate in an antiparallel fashion, creating the homodimer interface, to form a 10-stranded intermolecular, β-sheet. The association of the β1' strands is stabilized by intermolecular hydrogen bonding between the main-chains and through interlocking tryptophan and tyrosine residues (Trp223/Try225) that form an aromatic zipper at the dimer interface. Further studies have shown that removal of the tryptophan zipper resulted in loss of homodimerization, but did not affect the ability of the receptor to bind to DNA, to heterodimerize with RXRα, or to bind to activating ligands, and did not alter the subcellular localization of the receptor.[61] However, the recruitment of transcriptional coactivators has been shown to be dependent on PXR's ability to homodimerize,[61] indicating that long-range motions "communicate" stabilizing effects from homodimerization to the AF-2 domain.[62] Therefore, it has been proposed that the functional unit of PXR is a heterotetramer that is comprised of a PXR dimer bound to two separate RXRα units.[61, 62]

As mentioned above, PXR is activated by a wide range of ligands ranging from natural products, such as the active ingredient of St. John's wort, hyperforin, to prescription drugs, such as antibiotics (rifampicin) and anti-cancer drugs (paclitaxel), as well as endogenous compounds such as vitamin D and lithocholic acid, a by-product of cholesterol metabolism. Table 2.1 gives a list of selected PXR activators and their

relative potency. The inadvertent upregulation of metabolizing enzymes by PXR often leads to undesirable drug-drug interactions such as reduced efficacy of co-administered therapeutic drugs or the generation of toxic levels of drug metabolites. The classical example of this type of interaction is the failure of estrogen-containing oral contraceptives due to their increased metabolism by PXR gene products when taken with other known PXR activators such as rifampicin or St. John's wort. To avoid these interactions, high throughput screening methods to detect possible PXR agonists have been developed using *in vitro* methods[63, 64] and a commercialized kit is available.[64] As the potency of PXR activation by agonists has been shown to be species specific, the development of *in vivo* screening methods in animal models may not be optimal unless "humanized" models are used.[65, 66] Additionally, computational modeling methods have been developed to screen potential agonists based on structural similarity to known activators, through computational docking of ligands to the three dimensional structures generated from x-ray crystallography, NMR structures, or homology modeling of the protein, or through combination of both (reviewed in [67, 68]).

Table 2.1 Selected Agonists of PXR

Compound	Function	Mol Wt.(Da)	K_d	EC_{50}	Ref
17β-Estradiol	hormone	272		22 μM	[59]
Paclitaxel	anti-cancer drug	854		5 μM	[69]
Rifampicin	antibiotic	823		0.8 μM	[70]
SR12813	cholesterol lowering drug	507	27 nM		[71]
Hyperforin	active ingredient in St. John's wort	537	41 nM		[1]
Dexamethasone	anti-inflammatory agent	392		10 μM	[70]
Phenobarbitol	barbiturate	232		370 μM	[72]

Another method for preventing PXR mediated drug-drug interactions is through the therapeutic use of PXR antagonists. Until recently, very few PXR antagonists had been identified, but the list is steadily growing, due in part to the discovery that antifungal azoles such as ketaconazole, which were first characterized as weak agonists of PXR, act as antagonists to ligand bound PXR. Studies showed that these PXR antagonists allosterically inhibit the receptor by binding in the same hydrophobic groove to which the coactivator binds.[73, 74] Computational modeling and docking studies of this interaction eventually lead to the discovery of novel antagonists through database searching of commercially available molecules and through computer-aided antagonist design methods.[67, 68, 75-77] Table 2.2 presents a selected list of known PXR antagonists along with their corresponding half maximal inhibitory concentrations (IC_{50}), which are a measure of the concentration of the antagonist necessary to achieve a 50% reduction in the signal that results from the activation of PXR in the presence of a known agonist.

Table 2.2 Selected Antagonists of PXR

Compound	Function	Mol Wt (Da)	IC_{50}	Ref
Ecteinascidin (ET-743)	anti-tumor drug	762	2 nM	69
Ketaconazole	anti-fungal	531	~20 μM	73
Fluconazole	anti-fungal	306	~20 μM	74
Enilconazole	fungicide	297	~20 μM	74
Leflunomide	drug for rheumatoid arthritis	270	6.8 μM	75

Despite the plethora of studies as to the nature of gene activation by PXR, there are still many questions concerning the mechanisms of recruitment of transcriptional coregulators and the overall role of agonist and antagonists in the modulation of protein production through binding to nuclear receptors. To date, there have been very few

experimental studies that quantitatively measure the interaction of PXR with its transcriptional coregulators, agonists, and antagonists. As such the goal to this study is to use total internal reflection fluorescence microscopy (TIRF) to measure the binding equilibrium of the LBD of PXR to a peptide analog of the steroid receptor coactivator-1 (SRC-1) in the presence of rifampicin, a known ligand and classic transcriptional activator. The rates will be used to quantitatively define the cyclic nature of the ligand dependent binding of coregulators to PXR. As TIRF requires that the LBD of PXR be immobilized at the solid-solution interface, this chapter also briefly describes the development of immobilization techniques that preserve biological functioning of the immobilized species.

2.2 Theory

2.2.1 Equilibrium Binding of Coactivator Peptide in the Absence of Ligand

To measure the equilibrium binding of the LBD of PXR using TIRF, the receptor is irreversibly immobilized at a solid-solution interface (see Methods) at which a laser is internally reflected. Enough fluorescently-labeled coactivator is added such that the bound coregulator density is constant and the solution concentration is known. The presumed reaction scheme is

$$A + R \Leftrightarrow C_1 \qquad (1)$$

$$K_1 = \frac{C_1}{RA} \qquad (2)$$

$$R_T = R + C_1 \qquad (3)$$

where A is the solution concentration of fluorescently-labeled coregulator, R is the surface density of free receptor, C_1 is the surface density of receptor complexed with

fluorescent coregulator, R_T is the total surface density of deposited receptor, and K_1 is the equilibrium binding constant for the association of free receptor, R, with fluorescently-labeled coregulator, A. The resultant evanescently excited fluorescence from the surface is

$$F = QC_1 \qquad (4)$$

where Q is proportionality constant, and substituting for C_1 and R using equations (2) and (3) gives

$$F = \frac{K_1 A}{1 + K_1 A} QR_T \qquad (5)$$

which has the standard form for the binding of a monovalent ligand to an immobilized receptor.

By measuring the evanescently excited fluorescence at increasing solution concentrations of A, a plot of F versus A is obtained (Figure 2.3a). After background subtraction, the equilibrium constant K_1 can then be extracted by fitting the curve to equation (5). To measure the background signal, negative controls that lack the immobilized receptor are made, and the fluorescence intensity is recorded as function of solution concentration of the fluorescently labeled coregulator, as the background solution fluorescence increases linearly as a function of A (F=QAd, where d is the depth of the evanescent wave). The negative controls also account for contributions to the signal from nonspecific background. For simplicity, contributions from background will be ignored in the discussion of the theory.

2.2.2 Effect of Nonfluorescent Ligands

Addition of non-fluorescent ligands of PXR to the solution containing fluorescently labeled coregulators in the presence of the immobilized LBD of PXR, results in a multiple reaction system. The presumed reaction scheme (depicted in Figure 2.4) is

$$A + R \Leftrightarrow C_1 \qquad (1)$$

$$L + R \Leftrightarrow C_2 \qquad (6)$$

$$L + C_1 \Leftrightarrow C_3 \qquad (7)$$

$$A + C_2 \Leftrightarrow C_3 \qquad (8)$$

where L is the solution concentration of nonfluorescent ligand, C_2 is the surface density of receptor complexed with nonfluorescent ligand, and C_3 is the surface density of receptor complexed with ligand and fluorescent coregulator. This generates four equilibrium association constants

$$K_1 = \frac{C_1}{RA} \qquad (2)$$

$$K_2 = \frac{C_2}{RL} \qquad (9)$$

$$K_3 = \frac{C_3}{C_1 L} \qquad (10)$$

$$K_4 = \frac{C_3}{C_2 A} \qquad (11)$$

where K_2 is the association constant for ligand and receptor, K_3 is the association constant for receptor-coregulator complex and ligand, K_4 is the association constant for

receptor-ligand complex and coregulator and all K values have units of (solution concentration)$^{-1}$. The total concentration of receptors on the surface is defined by

$$R_T = R + C_1 + C_2 + C_3 \quad (12)$$

and the resulting fluorescence from surface bound evanescently excited molecules is

$$F = Q(C_1 + C_3) \qquad (13)$$

with the assumption that Q is equivalent for C_1 and C_3.

As the scheme outlined above is cyclic, the equilibrium constants are related. By using equations 10-13 and by simplifying we find that

$$K_1 K_3 = K_2 K_4 \qquad (14)$$

Therefore, by substituting for C_1 and C_3, equation 15 for the measured surface-associated fluorescence, after correction for background and contributions from solution, can be written as

$$F(A,L) = \frac{(K_1 + K_2 K_4 L)A}{1 + K_1 A + K_2 L + K_2 K_4 LA} QR_T =$$

$$\frac{K_1(1 + K_3 L)A}{1 + K_1 A + K_2 L + K_1 K_3 LA} QR_T \qquad (15)$$

where the second equation follows from the relationship defined in equation 14. Note that at the limits of A=0 and A=∞

$$F(0,L) = 0 \qquad (16)$$

$$F(\infty,L) \rightarrow \frac{K_1(1 + K_3 L)A}{K_1 A + K_1 K_3 LA} QR_T = QR_T \qquad (17)$$

Thus, when there are no fluorescent coregulators present, the measured fluorescence is zero, and, when the concentration of fluorescent coregulators is very high, the surface-immobilized receptors are saturated with coregulator and the signal is proportional to the total surface concentration of receptor. Also, applying the same limits to the ligand concentration results in

$$F(A,0) = \frac{K_1 A}{1 + K_1 A} QR_T \tag{18}$$

$$F(A,\infty) \rightarrow \frac{K_2 K_4 LA}{K_2 L + K_2 K_4 LA} QR_T = \frac{K_4 A}{1 + K_4 A} QR_T \tag{19}$$

Therefore, when the concentration of ligand is zero, the equation for the surface fluorescence is equivalent to equation 5 and, of the four, only the association constant K_1 contributes to the observed signal. When saturating concentrations of ligand are present ($L=\infty$), the resulting fluorescence is dependent on the association of C_2 with A, which is described by K_4. Additionally, equation 17 can be written as

$$F(A,L) = \frac{K_1 (\frac{1 + K_3 L}{1 + K_2 L}) A}{1 + K_1 (\frac{1 + K_3 L}{1 + K_2 L}) A} QR_T =$$

$$\frac{K_a A}{1 + K_a A} QR_T \tag{20}$$

where K_a is an "apparent" K, depends on L, and is given by

$$K_a = K_1 (\frac{1 + K_3 L}{1 + K_2 L}) \tag{21}$$

At the limits,

$$[K_a]_{L=0} = K_1 \tag{22}$$

$$[K_a]_{L=\infty} = (\frac{K_3}{K_2})K_1 = K_4 \tag{23}$$

which is in agreement with equations 16 and 17. Additionally, equation 21 can be rewritten using equation 14 as

$$K_a = \frac{K_1 + K_2 K_4 L}{1 + K_2 L} \tag{24}$$

Using TIRF, the surface fluorescence as a function of A is measured for increasing, constant values of L (to beyond a saturating concentration). In other words, multiple binding curves as a function of A are collected at different, constant concentrations of L. After background correction, each curve is fit to

$$F(A) = \frac{K_a A}{1 + K_a A} Q R_T \tag{25}$$

For each binding curve, best-fits of the data should give equivalent values of QR_T but values of K_a that depend on L (Figure 2.3b). The K_a values are then plotted as function of L, and fitted to equation 21, where K_2 and K_3 are free parameters and K_1 is determined from the curve taken when the concentration of ligand is zero. Using the relationship defined in equation 16, K_4 can then be determined. When the coregulator is a coactivator that acts by a mechanism in which the ligand increases the association constant for the coactivator and receptor such that $K_3 > K_2$, the K_a vs L plot appears as shown in Figure 2.5, where K_a ranges from K_1 to $K_4 > K_1$. If the coregulator is a corepressor in that $K_3 <$

K_2, the data would be similar, except that the plot would decrease from a maximum at L = 0 (K_1) to a minimum at at L = ∞ (K_4).

2.3 Materials and Methods

2.3.1 Materials

All chemicals were purchased from Fisher Scientific (Fairlawn, NJ) unless otherwise specified. Deionized (DI) water was generated using a NANOpure® II water purification system (Barnstead International, Dubuque, IA). All lipids were purchased from Avanti Polar Lipids (Alabaster, Alabama). Purified biotin protein ligase (BirA), Biomix A, and Biomix B, were purchased from Avidity (Aurora, Colorado).

2.3.2 Slide Cleaning

Fused-silica slides (1" x 1" x 1 mm, cut in house from 3" x 1" x 1 mm slides, Quartz Scientific Inc, Fairport Harbour, OH) and glass microscope slides (Gold Seal® Products, Portsmouth, NH) were cleaned in detergent. Cleaning was carried out by boiling slides in a 10% solution of 7X -ICN detergent (MP BioMedicals, Solon, OH), by bath sonicating for 30 minutes and by thoroughly rinsing with DI water. The slides were then sonicated in DI water for an additional 30 minutes, were rinsed again, and were dried at 160^{o}C. For test tubes and vials used for lipid preparation, base cleaning was carried out by soaking slides in a solution containing 120 g of potassium hydroxide dissolved in 120 mL of DI water and diluted to 1 L with 95% ethanol (AAPER Alcohol, Shelbyville, KY) for 10 minutes, washing with 95% ethanol, and then rinsing with DI water until the pH of the solution returned to neutral.

2.3.3 Immobilizing Proteins Using His_6 Tags

2.3.3.*i* *EGFP-His_6 Expression and Purification*

Glycerol stocks of *Escherichia coli* (*E. Coli*) cells transformed with a plasmid containing enhanced green fluorescent protein (EGFP) with a C-terminal His_6 tag under a T7 promoter (a gift from Dr. Dorothy Erie's lab, UNC chemistry) were used to express protein using standard procedures. Briefly, a starter culture of liquid Luria Broth with 100 μg/mL of ampicillin (LB_{AMP}) was inoculated with a single colony and grown overnight. This starter culture was used to inoculate (1:100 dilution) 2 L of fresh LB_{AMP}. Once the optical density at 600 nm was between 0.5 to 0.7, the culture was induced with a final concentration of 100 μM isopropyl-β-D-thiogalactopyranoside (IPTG) (99% Pure, Dioxane-free; Promega Corp, Madison, WI) and was grown for 4 hours. All cultures were grown at 37˚C with constant shaking at 225 rpm. Cells were harvested by centrifugation (Sorvall RC-3B, Sorvall Instruments, Newtown, CT) at 1600 g for 20 min at 4˚C. The pellet was frozen at -80°C prior to protein purification.

The cell pellet was resuspended in lysis buffer (50 mM sodium phosphate pH 7.8, 300 mM NaCl, 5 mM imidazole, and 1 mM phenylmethanesulphonylfluoride (PMSF), before adding lysozyme (1 mg/mL working concentration) and reacting for 30 min at 4°C with gentle agitation to lyse the cells. The cell solution was then tip sonicated using 10 second pulses for 1 minute, and cell debris were removed by centrifugation (Sorvall RC-3B) at 27000 g. The supernatant was 0.4 μm filtered, before running down a Sepahrose®4-B (Sigma-Aldrich, St. Louis, MO) guard column connected to a nickel nitrilotriacetic acid column (Ni-NTA) (Qiagen, Valencia, CA). The column was washed with buffer containing 50 mM sodium phosphate pH=8.0, 300 mM sodium chloride, and

20 mM imidazole until the absorbance at 280 nm was less than 0.01, and 1 mL fractions were eluted with buffer containing 50 mM sodium phosphate pH=8.0, 300 mM sodium chloride, and 250 mM imidazole. The fractions containing EGFP were then pooled and dialyzed into PBS (phosphate buffered saline; 0.05 M sodium phosphate pH=7.4, 0.15 M sodium chloride, 0.01% sodium azide) overnight at 4°C. The concentration of the protein was determined spectrophotometrically using the molar extinction coefficient (ε) of 5.5 x 10^4 $M^{-1}cm^{-1}$ at 488 nm.

2.3.3.*ii* *Vesicle Fusion and Sample Preparation*

For imaging studies, small unilamellar vesicles (SUVs) consisting of 5% 1,2-Dioleoyl-sn-Glycero-3-[N-(5-amino-1-carboxylpentyl)iminodiacetic acid)succinyl] (Nickel Salt) (Ni-DOGS-NTA); 93% 1,2-Dipalmitoyl-sn-Glycero-3-Phosphocholine (DPPC); 2% 1,2-Dipalmitoyl-sn-Glycero-3-Phosphoethanolamine-N-(7-nitro-2-1,3-benzoxadiazol-4-yl) (Ammonium Salt) (NBD-DPPE) were prepared by vesicle fusion. For control measurements, SUVS consisting of 98% (DPPC); 2% (NBD-DPPE) were also prepared. Lipids were mixed in chloroform, were dried under vacuum overnight, and were suspended in 3 mL of DI water such that the total concentration of lipids was 2 mM. The suspended mixture was then tip sonicated (Fisher Sonic Dismembrator, Model 300) for 15 minutes at 40-80% power in an ice bath to form SUVs. For TIRF measurements, 5 mol% Ni-DOGS-NTA, 95 mol% DPPC or 100 mol% 1-Palmitoyl-2-Oleoyl-Glycero-3-Phosphocholine (POPC) were made using the methods described above.

Immediately prior to use, fused silica substrates and glass slides were argon ion plasma cleaned for 10 minutes (PDC-3XG, Harrick Scientific, Ossining, NY), and the

vesicle suspension was clarified by air ultracentrifugation at 130,000 g for 30 min (Beckman Airfuge; Beckman-Coulter, Fullerton, CA). Planar substrate supports were formed by attaching fused-silica substrates (1 in x 1 in x 1 mm) to glass microscope slide (1 in x 3 in 1 mm) using double-sided tape (3M Corp., Part No. 021200-64988) to form slide "sandwiches". To the internal volume of the sandwich, 75 μL of SUVs were applied and incubated at room temperature for 1 hour before washing with 3 mL of PBS or PXR buffer (20 mM Tris pH 7.8, 250 mM sodium chloride, 5 mM dithiothreitol (DTT), 5% glyercol).

2.3.3.*iii* *Equilibrium Binding of EGFP to Ni- DOGS-NTA Membranes*

To study the equilibrium binding of EGFP to Ni-NTA-DOGS membranes using TIRF, slide sandwiches with lipid bilayers consisting of 5 mol% Ni- DOGS-NTA, 95 mol % DDPC or 100 mol% POPC were made as described above. To each slide, 200 μL of 0.5 to 10 μM EGFP in PBS were added, and evanescently-excited fluorescence intensity was measured for nine spots on each slide using the TIRF system described below. Three completed data sets were collected and averaged to obtain the equilibrium binding constant (K_d). Sigma Plot® (Systat Software Inc., San Jose, CA) was used for data analysis and curve fitting.

2.3.4 AviTag-His_6-LBD-PXR

2.3.4.*i* *Plasmids*

The LBD of human PXR, amino acids 130-434, containing a N-terminal His_6 tag was cloned into a commercially available vector containing an N-terminal AviTag insert (pAN4 vector; Avidity), using standard cloning techniques (work completed by Yuan Cheng under direction of Dr. Matthew Redinbo). The successful insertion of the

sequence was confirmed by DNA sequencing using commercially available primers (FASP and RSAP, Avidity). The AviTag-His_6-LBD-PXR forthwith will be referred to as b-PXR. A plasmid coding for an 88 amino acid fragment of SRC-1 (residues 623-710) was provided by Dr. Matthew Redinbo.[1]

2.3.4.*ii* *Expression and Purification*

b-PXR was co-coexpressed in *E. Coli* cells with the SRC-1 plasmid in either the BL21 (DE3) or BL21 (AI) strain (Invitrogen Corp, Carlsbad, CA). For expression in BL21 (DE3) cells, an overnight culture containing 100 μg/mL of ampicillin and 35 μg/ml chloramphenicol in LB ($LB_{AMP\text{-}CHLOR}$) was grown from a single colony and a 1:100 dilution of this cultrure was used to start a 1.5 L culture of TB (24 g/L yeast extract, 12 g/L tryptone, 17 mM potassium phosphate monobasic, 72 mM potassium phosphate dibasic, 0.4% glycerol) at the same concentration of antibiotic ($TB_{AMP\text{-}CHLOR}$) or 1.5 L culture of $LB_{AMP\text{-}CHLOR}$. The cells were grown to an optical density at 600 nm (OD_{600}) of approximately 0.6 at 37°C with shaking (225 rpm), and then induced with 50 μM to 1 mM of IPTG and allowed to grow at 37°C for 4 hours or overnight at 18°C. Alternatively, a 1.5 L culture of $TB_{AMP\text{-}CHLOR}$ was started as described above, IPTG was added, and the culture was allowed to grow overnight at 22°C. For expression in BL21 (AI) cells, a 1.5 L culture of $TB_{AMP\text{-}CHLOR}$ was started as described, grown until an OD_{600} of approximately 1.0 was reached, induced with 1 mM IPTG and 0.1% L-arabinose (98% pure, Sigma-Adrich), and allowed to grow at 37°C for 4 hours. For all cell preps, cells were collected by centrifugation (3000 g, 20 minutes), and the cell pellet was frozen at -80°C until protein purification.

For all cultures, the cell pellet was resuspended in Ni-A wash buffer (20 mM Tris, pH 7.8, 250 mM sodium chloride, 20 mM imidazole, 5% glycerol) with 2 mM PMSF, 50 µg/mL DNase, 5 µg/mL aprotinin and 5 µg/mL leupeptin and was tip sonicated using 5 second pulses with 10 second off cycles for 3 minutes. The mixture was then centrifuged at 27000 g for 45 minutes to pellet cell debris, and the supernatant was collected and 0.45 µm filtered (Millex-HV syringe filters; Millipore Corp., Billerica, MA) before loading onto a Ni-NTA column. The column was then washed with 400 mL of Ni-A buffer, and was eluted using Ni-E buffer (20 mM Tris, pH 7.8, 250 mM sodium chloride, 300 mM imidazole, 5% glycerol). The fractions containing protein were pooled and dialyzed overnight into biotinylation buffer (20 mM Tris pH 7.8, 250 mM NaCl, 10 mM imidazole). All steps were performed at 4°C. Protein purity was ascertained using SDS-PAGE with Coomassie blue staining.

Protein expression was verified using western blotting with anti-His_3-horseradish peroxidase (HRP) antibodies (His-probe (H-3) HRP; Santa Cruz Biotechnology, Inc, Santa Cruz, CA) by pelleting 1 mL of cell culture. After discarding the supernatant, the cell pellet was resuspended in 0.25 mL of Ni-A buffer and put through a freeze-thaw cycle three times to lyse cells. The samples were then centrifuged to remove cell debris, and an aliquot of the supernatant was diluted 1:1 with 2x SDS-Loading Buffer (250 mM Tris-base pH=6.9, 40% (v/v) glycerol, 9.25% (w/v) SDS, 0.1% bromophenol blue, 10% (v/v) β-mercaptoethanol). Alternatively, purified protein at a concentration of 1 µM was diluted 1:1 with 2x SDS-Loading Buffer, and all samples were loaded onto a 10% Tris-HCl ready gel (BioRad Laboratories, Hercules, CA) with 6xHis protein ladder (Qiagen). The gel was run at 120 V for 20 minutes, then at 180 V until complete, before

transferring to a PVDF membrane in 20 mM Tris-HCl, 20 mM glycine buffer at 350 mA for 60 minutes at 4°C. The membrane was blocked in 10 mM Tris pH=7.5, 150 mM sodium chloride, 5% (w/v) non-fat dried milk, and 0.05% Tween-20 buffer (TBST) for 45 minutes, was incubated with 1:1000 dilution of anti-His_3 antibody in TBST for 1 hour, was washed three times for 15 minutes with TBST, and was thoroughly washed with DI water to remove the milk. The blocking, incubation, and washing steps were all completed at room temperature. In the dark room, the blot was incubated with ECL detection chemical (Pierce Biotechnology, Rockford, IL) for 2 minutes and was exposed to Amersham Hyperfilm ECL photosensitive film (GE Healthcare, Piscataway, NJ) for 8-16 seconds. The film was developed using standard procedures.

2.3.4.*iii* *Biotinylation of b-PXR*

Purified b-PXR in biotinylation buffer was concentrated to 0.2 mg/mL using Amicon Ultra MWCO 10,000 (Millipore). Protein concentration was determined using Bio-Rad Protein Assay and BSA standards according to manufacturer's protocols. The protein was biotinylated according to manufacturer's instructions (Avidity product inserts). Briefly, the sample was diluted 8:1:1 b-PXR in biotinylation buffer, Biomix A, and Biomix B, and 2.5 μg of BirA were added for every 10 nmoles of b-PXR. The solution was allowed to react overnight at 4°C. To remove excess biotin, the sample was purified using Ni-NTA chromatography as described previously, and eluted B-PXR (biotinylated b-PXR termed B-PXR to distinguish addition of the biotin label) fractions were dialyzed into PXR buffer overnight at 4°C. After concentration, the protein samples were frozen in liquid nitrogen and stored at -80°C until use.

Biotinylation was confirmed using western blotting with anti-biotin-HRP antibodies (Santa Cruz Biotechnology). Briefly, samples containing B-PXR were diluted 1:1 with 2x SDS-Loading Buffer and run on a 10% Tris-HCl gel, as described previously, along with biotinylated protein ladder (Sigma-Aldrich). The gel was transferred to nitrocellulose membrane in 20 mM Tris-HCl, 20 mM glycine, 20% methanol buffer at 350 mA for 60 minutes at 4°C. The membrane was blocked in 5% bovine serum albumin (BSA) in b-TBS (20 mM Tris pH=7.5, 500 mM sodium chloride) overnight at 4°C. The blot was incubated with 1:2000 dilution of anti-biotin-HRP antibody in 3% BSA in b-TBST (b-TBS with 0.05% Tween-20) for 1 hour, was washed twice for 5 minutes with b-TBST, followed by two five-minute washes in TBS. The incubation and washing steps were completed at room temperature. In the dark room, the blot was developed as described above.

2.3.5 Fluorescent Labeling of SRC-1 peptide

A twenty five amino acid peptide of ID_2 of SRC-1 peptide was synthesized by the UNC Microprotein Sequencing & Peptide Synthesis Facility. The peptide sequence is

676-CPSSWSSLTERHKI**LHRLL**QEGSPS-700

where residue 680 has been mutated from the original sequence (H to W).[58] The average molecular weight is 2849.21 and the monoisotrophic molecular weight is 2847.44. The peptide was fluorescently labeled using either Alexa Fluor® 488 C_5 maleimide or fluorescein-5-maleimide (Molecular Probes, Carlsbad, CA) by incubating the peptide with a 2 to 3 mole excess of fluorophore and with a 10 mole excess of tris(2-carboxyethyl)phosphine (TCEP) in 30 mM ammonium bicarbonate, 25 mM NaCl pH=7.5 overnight at 4°C. The reactions were stopped by adding an excess of 2-

mercaptoethanol, before purification to remove excess free dye. For labeling with Alexa Fluor® 488, the pH of the sample was adjusted to 5.0 using 0.1 M acetic acid, and the mixture was run down a Q Sepharose™ ion exchange column (GE Healthcare) equilibrated in 30 mM ammonium acetate pH=5.0. For fluorescein labeling, the sample was run down the Q Sepharose™ ion exchange column equilibrated in 30 mM ammonium bicarbonate pH=8.0. For both systems, the labeled peptide eluted in equilibration buffer, and peptide fractions were collected and lyophilized. The lyophilized samples were reconstituted in water, and purified by high performance liquid chromatography (HPLC), using a 0 to 40% gradient of solvent B (95% acetonitrile, 5% water 0.1% trifluoroacetic acid) in solvent A (95% water, 5% acetonitrile, 0.1% trifluoroacetic acid), to remove salt. All samples were run on a Atlantis C18 Prep T3 column (10 x 100 mm) using a Waters HPLC with Delta 600 pump and controller (Waters Corp, Milford, MA). HPLC fractions were collected and lyophilized, and the purified peptide was stored at -20°C. Peptide labeling and purity were confirmed using mass spectrometry.

2.3.6 Surface Immobilization of Receptors Using NeutrAvidin (Control Experiments)

For control experiments, NeutrAvidin (Pierce Biotechnology) (NAv) and B-PXR were labeled with fluorescein isothiocyanate (FITC) and fluorescein-5-maleimide respectively, using standard procedures. NeutrAvidin was weighed out and dissolved in 0.1 M sodium bicarbonate pH=9.0 at a concentration 0.5 mg/mL and reacted with a 20 mole excess of FITC for 1 hour at room temperature. B-PXR in PXR buffer lacking DTT was reacted with 20 mole excess of fluorescein-5-maleimide in the presence of 10 mol excess of TCEP for 2 hours at 4°C. For both proteins, the free dye was separated from

the protein by running the mixture down a G-25 Sephadex® (Sigma-Aldrich) column that was equilibrated in PXR buffer. Eluted fractions were collected, pooled, and concentrated using Amicon YM-10 centrifugal concentrators. For B-PXR, the concentration of the protein was determined using BioRad Protein Assay and BSA standards, and the labeling ratio was determined using the concentration of protein and the concentration of fluorophore, which was determined spectrophometrically using $\varepsilon_{\lambda=492}$=83,000 $M^{-1}cm^{-1}$ for fluorescein-5-maleimide. For NAv, the concentration and labeling ratio were determined spectrophotometrically using $\varepsilon_{\lambda=280}$=1.66 for NAv at concentration of 1 mg/mL (Pierce Biotechnology, product insert), CF_{280}=0.3 and $\varepsilon_{\lambda=494}$=68,000 $M^{-1}cm^{-1}$ for fluorescein-5-maleimide, where CF is correction factor ($\varepsilon_{\lambda=280}/\varepsilon_{\lambda=494}$).

For control measurements, 50 μL of a solution containing 0.5 mg/mL of fluorescein labeled NAv (F-NAv), 0.1 mg/mL of ovalbumin (Ova) (98% pure; Sigma-Aldrich) or of a solution containing 0.5 mg/mL NAv, 0.1 mg/mL Ova in DI water were pipetted into a fused-silica/slide "sandwich" and allowed to non-specifically adsorb for 1 hour at room temperature, before being rinsed with 2 mL of PXR buffer. To the non-fluorescent slide, 200 μL of a 0.1 mg/mL solution of fluorescein-5-maleimide labeled B-PXR (FM-B-PXR) were added, and the slide was incubated at room temperature for 5 minutes, before rinsing with 1 mL of PXR buffer. After 30 minute incubation intervals at room temperature, the slides were washed with an additional 1 mL of PXR Buffer. At each time interval (t=0 to 60 minutes), using TIRF the average evanescently-excited fluorescence intensity over 10 seconds was measured for 4 different spots on each slide, and the four values were averaged for comparison.

2.3.7 Equilibrium Binding of SRC-1 to Immobilized B-PXR

For TIRF measurements, samples were created by pipetting 50 μL of a solution consisting of 0.5 mg/mL NAv, 0.1 mg/mL in water or PXR buffer, which had been clarified using ultracentrifugation immediately prior to use (see lipid procedure), into a slide sandwich and incubating for 1 hour at room temperature. The slide was then washed with 2 mL of PXR buffer. For positive controls, immediately prior to use 200 μL of a 0.1 mg/mL solution of B-PXR, which was kept on ice until use, was injected into the sandwich, incubated for 5 minutes, and washed with 1 mL of PXR buffer. Then, 150 μL of PXR buffer containing rifampicin, at concentrations ranging from 10 nM to 1 μM, and the fluorescently labeled SRC-1 peptide (typically with a labeling ratio of less than 10%), at concentrations ranging from 0.5 μM to 200 μM, were pippetted into sandwich. The sample was mounted, excited using TIRF, and the fluorescence intensity was recorded as an average over 10 seconds for nine spots on each sample. For negative controls, the process was repeated except 150 μL of buffer were added to the slide in place of B-PXR. Sigma Plot® was used for data analysis and curve fitting.

2.3.8 Apparatus for TIRF and Epifluorescence

Through-prism total internal reflection experiments were carried out on an instrument consisting of an inverted microscope (Zeiss Axiovert 35, Thornwood, NY), an argon ion-laser (Innova 90-3; Coherent, Palo Alto, CA), and a single-photon counting photomultiplier (RCA C31034A, Lancaster, PA). The instrument was controlled with an in-house LabVIEW program and DAQ board (PCI-MIO-16XE-50, Texas Instruments, Austin, TX), and the average fluorescence intensity was collected using a PC-based correlator board (model 5000/E, ALV). All samples were excited using the 488 nm line,

and the evanescently generated fluorescence was collected using a 40x 0.55 NA LWD objective (Nikon Instruments Inc., Nelville, NY). All experiments were conducted at room temperature.

For imaging, the same instrument was used in epifluorescence mode. The collected light was directed to a charge-coupled device (CCD) (Photometrics CH250) imaging detector connected to a PC with Photometrics PMIS Image 200 Processing Software (Tucson, AZ). All 8-bit digitalized images were taken using an excitation wavelength of 488.0 nm, 40x water 0.75 NA objective, and an appropriate long-pass filter for fluorescence detection.

2.4 Results

2.4.1 Immobilizing Proteins at Surfaces using His_6 Tags

In this experiment, the ability of nickel chelating lipids to coordinate to the 6x histidine tag of proteins was examined using a test system consisting of planar, lipid bilayers containing 5 mol% Ni-DOGS-NTA and enhanced green fluorescent protein (EGFP) with a C-terminal His_6 tag. To obtain equilibrium binding constants, the evanescently excited fluorescence generated by the association of EGFP in solution with Ni-DOGS-NTA lipid bilayers on a fused-silica surface was measured as a function of the solution concentration of EGFP using TIRF (Figure 2.6). Negative controls, in which lipid bilayers consisting of 100 mol % POPC were used in place of Ni-DOGS-NTA membranes, were used to account for background fluorescence signal generated from EGFP that was diffusing within the evanescent wave but was not bound to the surface. After background subtraction, the curves were fitted to

$$F = \frac{B_{\max} x}{K_d + x} \qquad (26)$$

where F is the measured fluorescence for a given EGFP solution concentration, B_{max} is the fluorescence at saturation, x is the concentration of EGFP in solution, and K_d is the equilibrium dissociation constant. From three complete sets of data, an average K_d of 4.43 ± 0.62 μM was obtained, which is consistent with other previously reported values for the interaction of histidine tags with metal chelating lipids.[78, 79] This weak binding constant suggests that reversible association between histidine-tagged proteins to lipid bilayers occurs, which is undesirable in these TIRF experiments. As such, this method for immobilizing proteins at the solid-solution interface is not feasible for these TIRF experiments.

2.4.2 Specifically Biotinylating the LBD of PXR

To biotinylate PXR at a single site on the protein surface, a specific recognition sequence called an AviTag was added to the N-terminal of the LBD of PXR, using a commercial DNA vector and standard cloning techniques. The tag was added to the N-terminal to preserve the structural integrity of the C-terminal LBP and AF_2 domains. Biotin protein ligase or BirA, a naturally occurring *E. Coli* protein, recognizes the AviTag sequence and through an ATP dependent reaction adds a biotin to the terminal amine in the side chain of a lysine residue in the tag. The cloning was verified using DNA sequencing, but attempts to co-express the AviTag/PXR plasmid with the SRC-1 plasmid in BL21 (DE3) *E. Coli* cells resulted in no expression of b-PXR under all conditions tested. As the commercial AviTag vector is under a trc promoter, which is a modified lac promoter, and the SRC-1 promoter is under a T7 promoter, the SRC-1 plasmid was expressed to the exclusion of the AviTag/PXR plasmid in BL21 (DE3) cells. Co-expressing the plasmids in BL21 (AI) *E. Coli* cells resulted in expression of both

vectors, but with low protein yields of b-PXR (approximately 0.5 milligrams of b-PXR per liter of culture). However, a sufficient amount of purified protein was obtained to conduct TIRF experiments. To increase protein yield, molecular cloning is currently being performed to place the AviTag-PXR sequence in a plasmid that operates under a T7 promoter.

Purified b-PXR was biotinylated *in vitro* using commercially purchased biotin protein ligase and reaction buffers. As BirA is inhibited by sodium chloride, the reaction was allowed to proceed overnight to ensure maximum labeling efficiency. The biotin labeling was verified by western blotting with anti-biotin antibodies. Biotinylated protein ladder served a dual purpose, acting as a molecular weight marker and as a positive control, and b-PXR samples before addition of BirA served as a negative control. As the molecular weight of BirA is similar to that of b-PXR, samples containing working concentrations of BirA and the supplied reaction buffers but without b-PXR were also run to exclude the possibility that the observed bands were generated from BirA. Figure 2.7 shows an example of a western blot of biotinylated PXR (B-PXR).

2.4.3 Immobilizing Proteins at Surfaces Using Biotin-Avidin Interactions

A promising method for immobilizing proteins at the solid-solution interface for TIRF experiments is to use systems that take advantage of the strong binding of biotin by avidin (K_a on the order of 10^{15} M). As such, NeutrAvidin (NAv), a modified form of avidin, was non-specifically adsorbed onto fused-silica surfaces in the presence of ovalbumin and was used to bind biotinylated biomolecules in solution, thereby irreversibly immobilizing them at the solid-solution interface. To determine whether the non-specific adsorption of NAv to glass surfaces is irreversible, fluorescently labeled

NAv was immobilized onto fused-silica surfaces in the presence of ovalbumin. The sample was then excited using TIRF, and the evanescently generated fluorescence was recorded for several spots on the sample and averaged. After 30 minute time intervals, the slide was washed with buffer, and the average fluorescence intensity was measured again. This experiment was repeated using NAv slides (non-fluorescent) that were incubated with fluorescently labeled B-PXR to determine whether biotin-labeled molecules are irreversibly immobilized on surfaces coated with NAv. As the average evanescently excited fluorescence for both systems declined less than 5% over the observed time period (data not shown), it was concluded that NAv non-specifically adsorbs to glass surfaces in an irreversible fashion, and that, over the course of a typical TIRF experiment, the binding of biotinylated biomolecules by surface immobilized NAv is also irreversible. Therefore, this system is a feasible method for immobilizing biological molecules at surfaces for TIRF experiments.

2.4.4 Equilibrium Binding of B-PXR to SRC-1 Peptide

The equilibrium constants for immobilized B-PXR binding to Alexa®Fluor 488 (A488) labeled SRC-1 peptide were determined for increasing concentrations of rifampicin using TIRF. For a given, fixed concentration of rifampicin, the evanescently excited fluorescence was measured as a function of the solution concentration of A488-SRC-1, and three complete sets of data were collected for each concentration of rifampicin. After background subtraction, the three sets of data were normalized to each other using fluorescence intensities obtained at a single, overlapping concentration of A488-SRC-1, thus accounting for sample to sample variation in fluorescence intensity. The normalized data were plotted as a single curve and fit to

$$F(A) = \frac{B_m A}{K_d + A} \qquad (27)$$

where B_m is equal to QR_T, A is the solution concentration of A488-SRC-1, and K_d is the inverse of K_a (see equation 21). The fitted curves are shown in Figure 2.8. The equilibrium dissociation constants obtained for SRC-1 binding to immobilized B-PXR as a function of rifampicin concentration are listed in Table 2.3. As expected, the equilibrium dissociation constant decreases with increasing solution concentration of rifampicin, indicating that the presence of ligand increases the affinity of B-PXR for the coactivator.

Table 2.3 K_d for B-PXR Binding to SRC-1

Rifampicin (μM)	K_d (μM)	Error (μM)
0	23.47	± 4.78
0.010	16.99	± 3.31
0.030	6.68	± 2.42
0.100	3.12	± 0.64
1.000	2.68	± 0.99

To determine the equilibrium association constants defined in equations 9-10, the K_d values in Table 2.3 were converted to their corresponding K_a values ($K_a=1/K_d$). The values were then plotted as a function of the solution concentration of rifampicin (L) and fit to equation 24, with K_2 and K_4 as free parameters and setting K_1 equal to the K_d obtained in the absence of rifampicin. The fitted plot is shown in Figure 2.9 and has the predicted shape for coactivator binding to the LBD of PXR in the presence of ligand. Using the relationship defined in equation 14, K_3 was then determined, and the calculated equilibrium association constants are shown in Table 2.4. For all values, the reported

error corresponds to the standard error generated by curve fitting in Sigma Plot or is determined using standard equations for the propagation of error.

Table 2.4 Calculated K's for B-PXR Binding to SRC-1

Constant	K_a	Error (±)	K_d	Error (±)
K_1*	42.6 nM^{-1}	8.7 nM^{-1}	23.5 μM	4.8 μM
K_2**	17.5 μM^{-1}	7 μM^{-1}	56.9 nM	22.5 nM
K_3**	168 μM^{-1}	77 μM^{-1}	5.92 nM	2.71 nM
K_4#	0.45 μM^{-1}	0.043 μM^{-1}	2.44 μM	0.25 μM

*Measured using TIRF
** Free parameters determined by fitting to K_a vs L plot
# Determined using Equation 14 and K_1, K_2, and K_3 values

As it was discovered that one of the reagents in the sample buffer, DTT, activates PXR by forming a covalent bond to a cysteine (Cys284) in the ligand binding pocket,[59] the calculated equilibrium constants are most likely not completely accurate for the PXR, SRC-1, rifampicin system. Subsequently, in experiments conducted using buffers made with newly purchased DTT, the ligand binding dependence of PXR to SRC-1 was diminished, and the receptor was believed to be in a permanently active state, as a K_d of ~6 μM was obtained for SRC-1 binding to PXR in the absence of rifampicin (data not shown). As such, experiments are currently being repeated with TCEP rather than DTT to determine accurate equilibrium binding constants. However, the data shown in Figure 2.8 strongly suggest that a ligand-dependent increase in the affinity of PXR for coactivator is observed. Whether the exact values for the equilibrium constants listed in Table 2.4 will remain the same is yet to be determined.

2.5 Discussion

As TIRF is a surface specific technique, studying the dynamics of biochemical interactions that typically occur in solution requires the immobilization of one of the components at the solid-solution interface in a manner that does not disrupt the biological functioning of the system. In this chapter, two methods to specifically orient biological molecules on fused silica surfaces were tested. The first method, which utilized the binding of hexa-histidine tags, which are typically added to recombinant proteins for ease of purification, to substrate-supported phospholipid membranes containing metal chelating lipids, was found to be insufficient for use with TIRF. However, commercial production of phospholipids or of beads containing multivalent chelator heads, which have been shown to increase the stability of the interaction between poly-histidine tags and chelator moieties by up to 4 orders of magnitude,[79] in combination with the use of His_{10} tagged proteins may allow this technique to be used in the future. The second technique, which utilizes the high binding affinity of avidin to biotin, resulted in irreversible immobilization of biotinylated protein bound to surface-immobilized NeutrAvidin, a modified form of avidin, and was adopted for use with TIRF.

Using TIRF, apparent equilibrium constants for the binding of surface-immobilized LBD-PXR to fluorescently labeled SRC-1 coactivator in the presence and absence of rifampicin were determined and are listed in Table 2.3. The apparent association constants were plotted as a function of rifampicin concentration and were used to determine the four cyclic rate constants defined by equations 2, 9-11, which are listed in Table 2.4. An approximately 10 fold increase in PXR binding affinity for SRC-1 was observed at saturating concentrations of rifampicin (K_4) as compared to the affinity

observed in the absence of rifampicin (K_1). Furthermore, constants for the association of PXR to rifampicin (K_2) and for the association of SRC-1-bound PXR to rifampicin were also determined (K_3). The associated errors in K_2 and K_4 were generated by the curve fitting software, and the error for K_3 was determined using standard propagation of errors. As such, the error associated with these constants could be reduced by obtaining measurements for the ligand-dependent binding of PXR to SRC-1 at more concentrations of rifampicin (to generate more K_a's) to reduce uncertainty in the fits. However, DTT, which covalently binds in the LBP of PXR, was present in the sample buffer, bringing into question the exact values shown in Tables 2.3 and 2.4. These measurements will be repeated in the future using TCEP rather than DTT.

While numerous studies have qualitatively or quantitatively assessed the activation of PXR by ligand binding, the majority of these studies have used methods, such as intracellular reporter systems,[80] co-immunoprecipitation,[81] and competitive binding studies,[71] that do not readily lend themselves to the study of the kinetic rates of molecular interactions. Subsequently, to date, quantitative studies on the kinetic rates of association of PXR to transcriptional coregulators in the presence or absence of ligand, to RXRα, or to xenobiotic DNA recognition elements have not been conducted. To obtain kinetic rates for the ligand-dependent binding of coregulators to the LBD of PXR, the *in vitro* system described in this chapter could be studied using total internal reflection in combination with fluorescence correlation spectroscopy[7, 82] or fluorescence recovery after photobleaching.[5] In addition, the rate of data acquisition could greatly be increased for both equilibrium and kinetic studies through automation using microfluidic devices.[11]

Overall, the experiments presented in this chapter represent the beginning of a plethora of studies that could be conducted to quantitatively explore the equilibrium binding of PXR using TIRF. The ligand-dependent binding of PXR to transcriptional coactivators could be expanded to include ligands of varying sizes to determine whether the structural disordering of PXR that is necessary to accommodate large ligands affects the affinity of the receptor for coactivators. Additionally, the mechanisms of corepressor binding to unliganded PXR and of the displacement of bound corepressor through agonist binding in the LBP of PXR could be studied using fluorescently-labeled peptide analogs of the IDs of nuclear corepressors known to interact with PXR, such as silencing mediator of retinoid and thyroid hormone receptors (SMRT).[81, 83] Moreover, these studies could be repeated using the full sequences of coregulators and of PXR. As nuclear receptors have been shown to preferentially bind to different coregulators,[84] the association of PXR with several coactivators and corepressors could also be studied. Furthermore, the heterodimerization of PXR with RXRα could be studied using PXR and fluorescently labeled RXRα, preferably using full length receptors as a recent crystal structure of peroxisome proliferated-activator receptor (PPAR), another nuclear receptor that exhibits ligand-dependent activation, in complex with RXRα and DNA has shown that interactions occur between the ligand binding domain of PPAR and the DNA binding domain of RXRα.[85] Finally, *in vitro* equilibrium binding of PXR and PXR-RXRα heterodimers to xenobiotic DNA recognition elements could be measured using full length receptors. Ultimately, the information obtained from these *in vitro* models using TIRF could provide valuable insight into the biological functioning of the system and could aid in designing *in vivo* experiments.

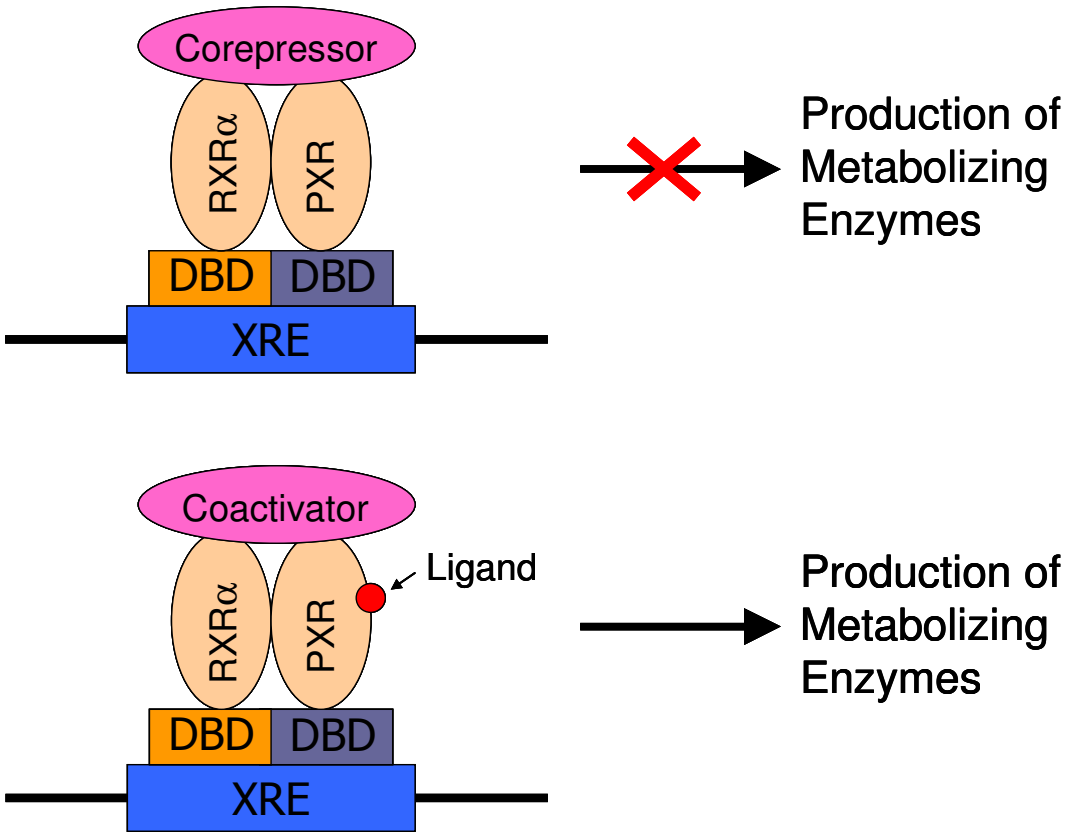

Figure 2.1 Ligand-Dependent Activation of PXR. Unliganded PXR binds to the promoter region of target genes at xenobiotic response elements (XRE) as a heterodimer with RXRα and actively represses target gene activation by recruiting transcriptional corepressors (top). Upon ligand binding, a conformational change in the LBD of PXR displaces the corepressor, and PXR recruits transcriptional coactivators, leading to the activation of target gene expression and production of metabolizing enzymes (bottom).

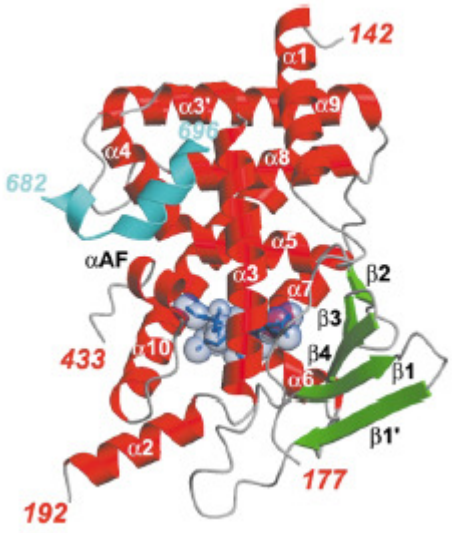

Figure 2.2 Crystal Structure of the LBD of PXR. The crystal structure of one monomer of the PXR-LBD bound to SRC-1 peptide (cyan) and SR12813 (blue) is shown above. From this view, the novel strands β1 and β1', which form the novel homodimer interface, are also visible (green). (Reprinted from reference 17)

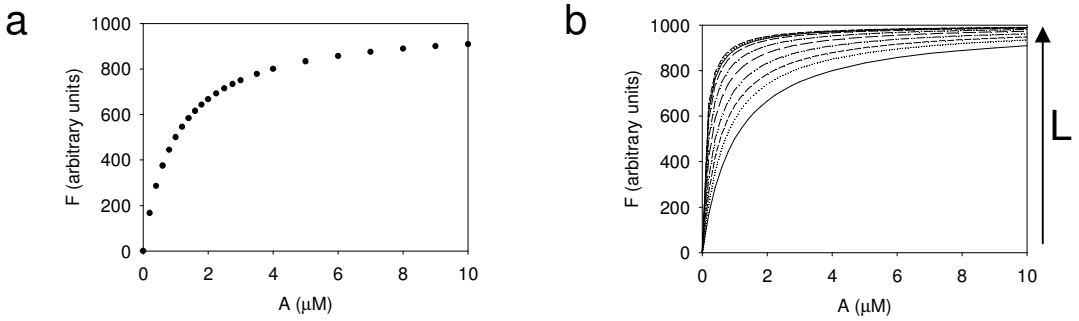

Figure 2.3 Theoretical TIRF Equilibrium Binding Curves. Theoretical equilibrium binding curves are shown for the ligand-dependent association of surface-immobilized PXR with fluorescently labeled coactivator in the absence of ligand (a) and with increasing concentration of ligand (L) (b). For these simulations, the curves are assumed to be corrected for contributions from background light and from the linear dependence of evanescently excited fluorescence on the solution concentration of coregulator. Additionally, constants have been fixed such that K_1=1 μM^{-1}, K_2=2 μM^{-1}, K_3=20 μM^{-1}, K_4=10 μM^{-1} and QR_T=1000.

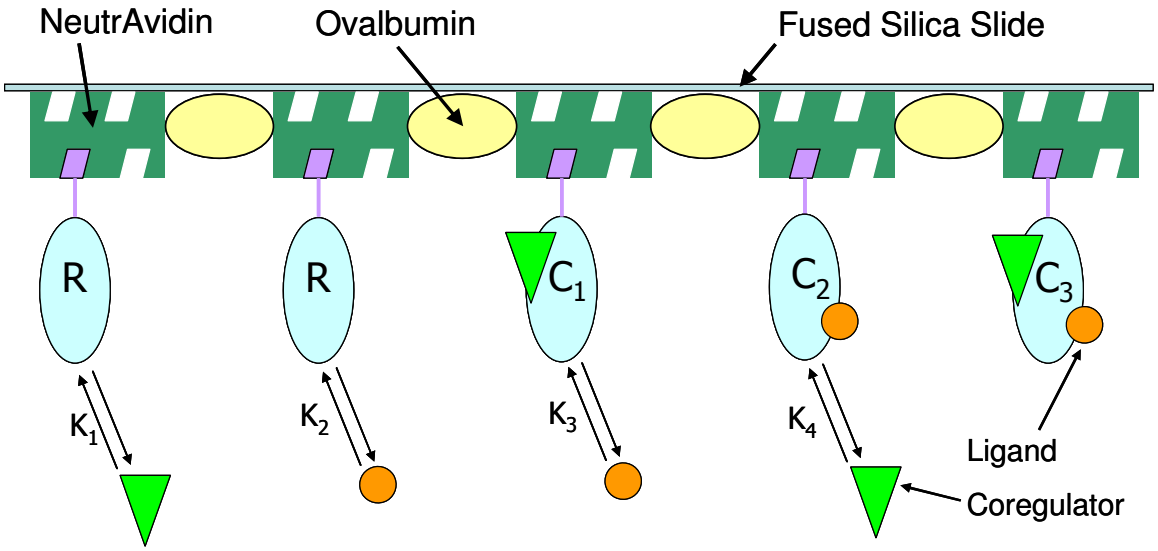

Figure 2.4 Reversible Equilibria of Surface-Immobilized PXR Complexes. This cartoon illustrates the simultaneous equilibrium binding processes occurring among surface-immobilized LBD-PXR (R) with coregulators and ligands in solution. LBD-PXR binds coregulator or ligand to form complex 1 or complex 2, which is described by K_1 and K_2, respectively. Additionally, C_3 is generated when C_1 binds ligand or when C_2 binds coregulator, giving rise to K_3 and K_4, respectively. For TIRF, the coregulator is fluorescently labeled, therefore; only binding events that lead to the formation of C_1 and C_3 contribute to the evanescently-excited fluorescent signal at the surface.

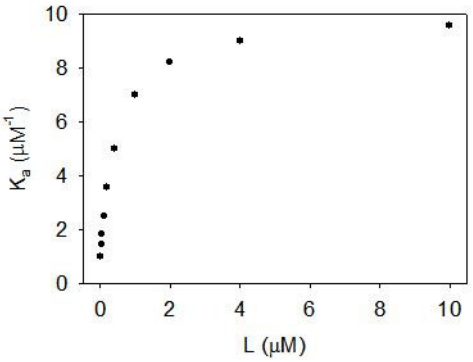

Figure 2.5 Theoretical K_a vs L Curve. A theoretical K_a vs L curve is presented, where K_a are the equilibrium binding constants obtained for surface-immobilized PXR to fluorescently labeled coactivator in solution as a function of ligand concentration (L). In this model, ligand binding to PXR increases the affinity of the receptor for the coactivator. This plot was generated using K_1=1 μM^{-1}, K_2=2 μM^{-1}, K_3=20 μM^{-1} and K_4=10 μM^{-1}.

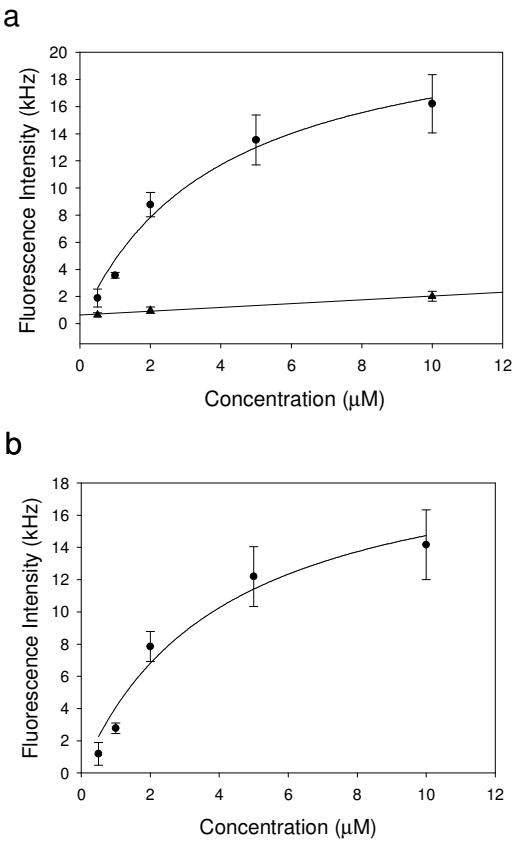

Figure 2.6 Equilibrium Binding of EGFP-His_6 to Ni-DOGS-NTA Lipids. This figure shows a representative binding curve obtained by measuring the evanescently excited fluorescence generated by EGFP binding to Ni-NTA-DOGS as a function of the solution concentration of EGFP before (a) and after (b) background correction. By fitting the background subtracted data to equation 26, a K_d of 4.43 ± 0.62 μM was obtained.

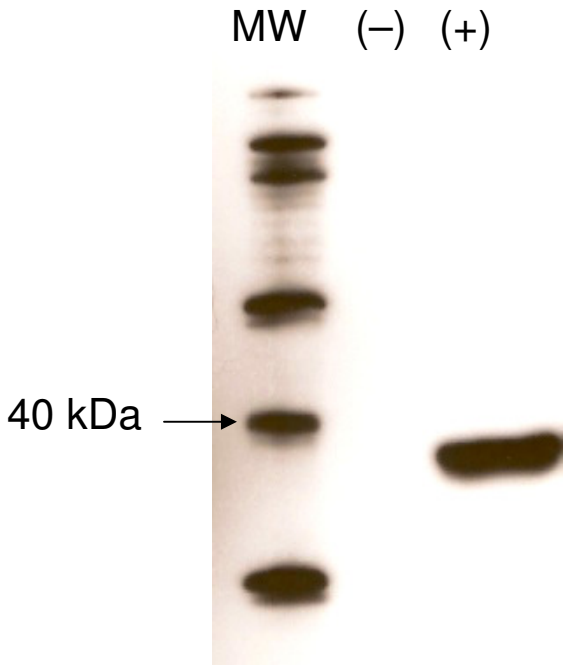

Figure 2.7 Western Blotting of B-PXR. Western blot analysis of b-PXR/BirA reaction solution under reducing conditions with anti-biotin-HRP antibodies showed successful biotinylation of PXR (+). To ensure the observed signal was not from BirA, a negative control consisting of BirA in PXR buffer with BiomixA and Biomix B was run and no signal was observed (-). Biotinylated protein ladder was run as a MW marker (MW).

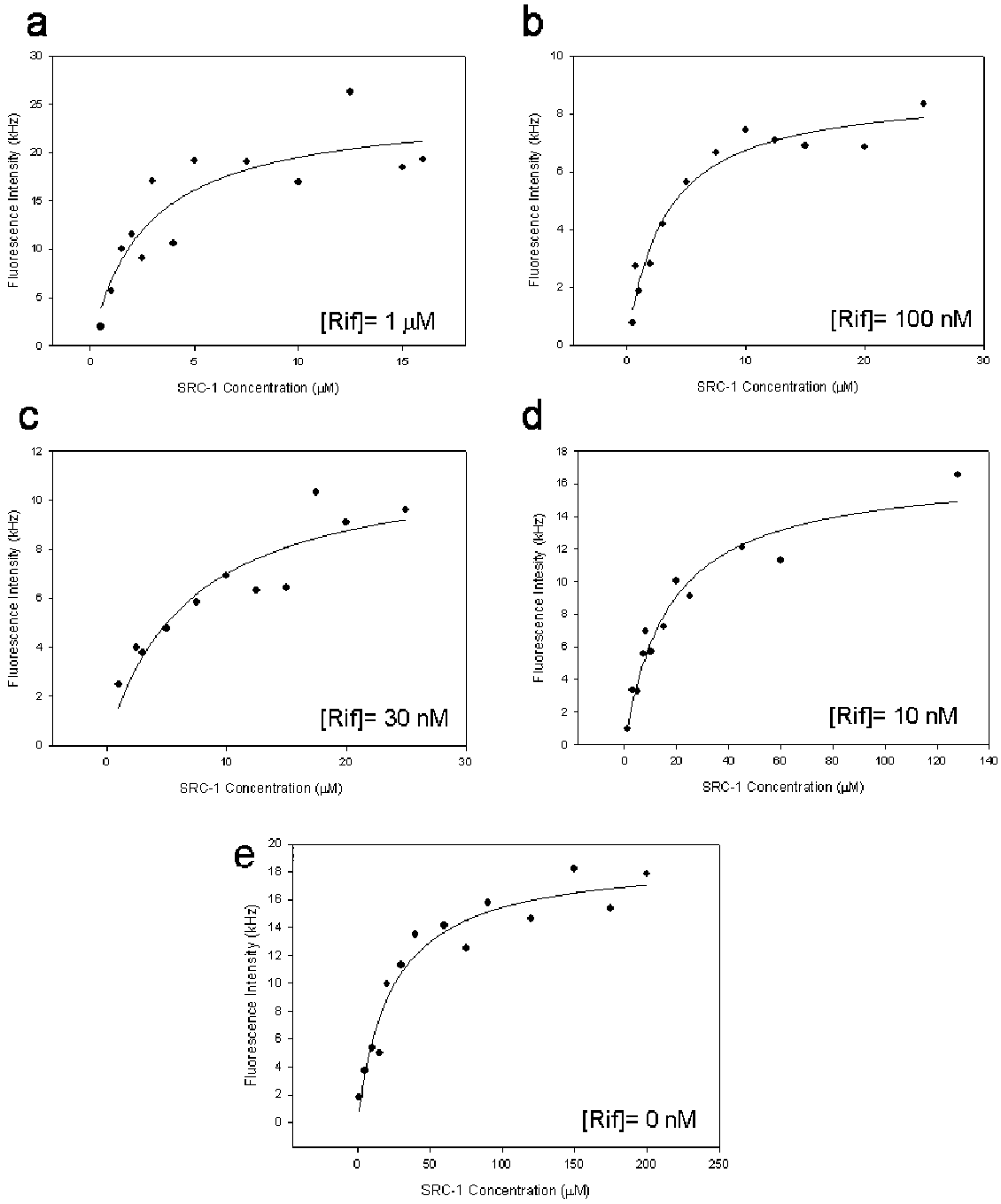

Figure 2.8 SRC-1 Binding to Immobilized B-PXR. This figure shows representative binding curves obtained using TIRF for the binding of fluorescently labeled SRC-1 peptide to the biotinylated LBD-PXR in the presence of 1 μM (a), 100 nM (b), 30 nM (c), 10 nM (d) and 0 nm (e) rifampicin (Rif). Each curve is a composite of three sets of background corrected and normalized data and are fit to equation 27 to obtain equilibrium binding constants, which are listed in Table 2.3.

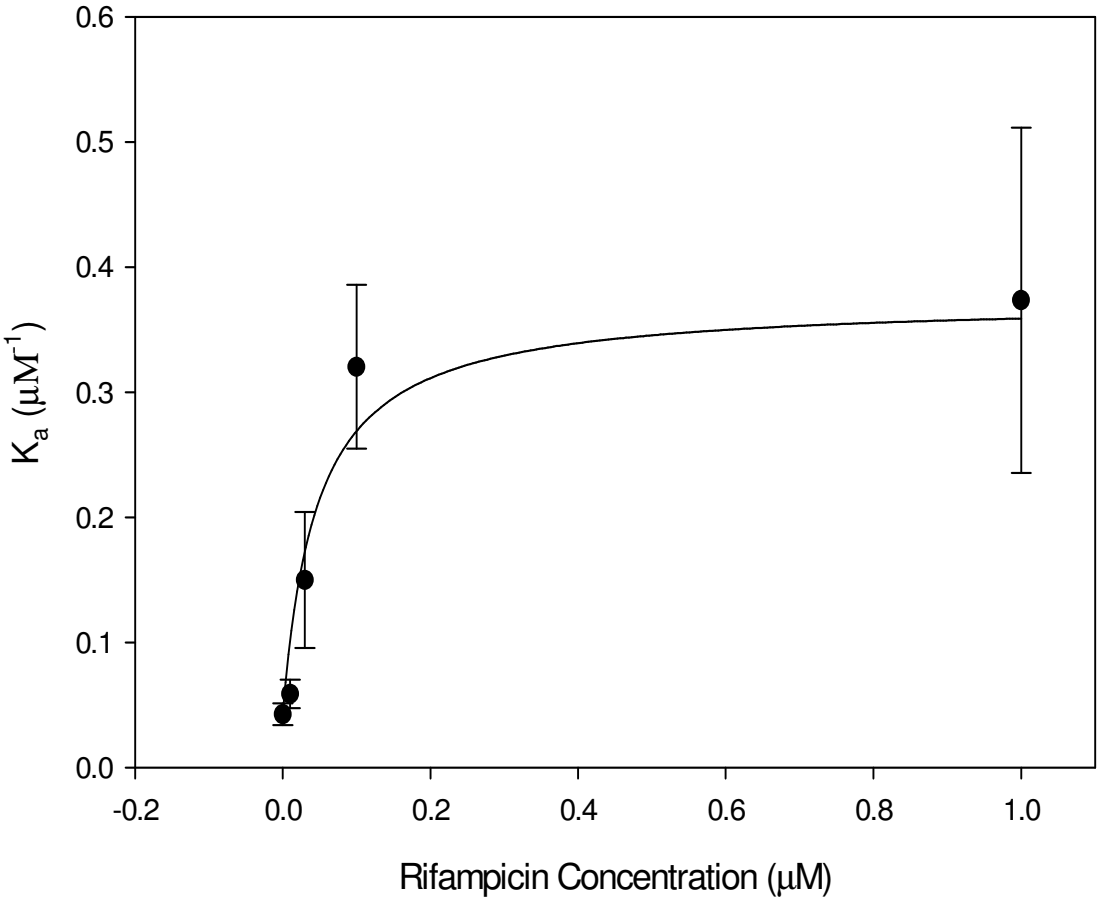

Figure 2.9 Ligand-Dependent Binding of PXR. In this curve, the association constants measured for SRC-1 binding to PXR are plotted as a function of the corresponding solution concentration of rifampicin. The plot was fitted to equation 24 with K_2 and K_4 as free parameters and K_1 equal to the association constant measured in the absence of rifampicin.

2.6 References

1. Kliewer, S. A.; Moore, J. T.; Wade, L.; Staudinger, J. L.; Watson, M. A.; Jones, S. A.; McKee, D. D.; Oliver, B. B.; Willson, T. M.; Zetterstrom, R. H.; Perlmann, T.; Lehmann, J. M., An orphan nuclear receptor activated by pregnanes defines a novel steroid signaling pathway. *Cell* **1998,** *92* (1), 73-82.

2. Orans, J.; Teotico, D. G.; Redinbo, M. R., The Nuclear Xenobiotic Receptor Pregnane X Receptor: Recent Insights and New Challenges. *Molecular Endocrinology* **2005,** *19* (12), 2891-2900.

3. Ma, Q., Xenobiotic-activated receptors: From transcription to drug metabolism to disease. *Chemical Research in Toxicology* **2008,** *21* (9), 1651-1671.

4. Zhang, B.; Xie, W.; Krasowski, M. D., PXR: a xenobiotic receptor of diverse function implicated in pharmacogenetics. *Pharmacogenomics* **2008,** *9* (11), 1695-1709.

5. Staudinger, J. L.; Ding, X.; Lichti, K., Pregnane X receptor and natural products: beyond drug-drug interactions. *Expert Opinion on Drug Metabolism & Toxicology* **2006,** *2* (6), 847-857.

6. Kliewer, S. A.; Goodwin, B.; Willson, T. M., The nuclear pregnane X receptor: A key regulator of xenobiotic metabolism. *Endocrine Reviews* **2002,** *23* (5), 687-702.

7. Hartley, D. P.; Dai, X.; Yabut, J.; Chu, X.; Cheng, O.; Zhang, T.; He, Y.; Roberts, C.; Ulrich, R.; Evers, R.; Evans, D., Identification of potential pharmacological and toxicological targets differentiating structural analogs by combination of transcriptional profiling and promoter analysis of LS-180 and Caco-2 adenocarcinoma cell lines. *Pharmacogenetics and Genomics* **2006,** *16*, 579-599.

8. Hariparsad, N.; Chu, X. Y.; Yabut, J.; Labhart, P.; Hartley, D. P.; Dai, X. D.; Evers, R., Identification of pregnane-X receptor target genes and coactivator and corepressor binding to promoter elements in human hepatocytes. *Nucleic Acids Research* **2009,** *37* (4), 1160-1173.

9. Kawana, K.; Ikuta, T.; Kobayashi, Y.; Gotoh, O.; Takeda, K.; Kawajiri, K., Molecular mechanism of nuclear translocation of an orphan nuclear receptor, SXR. *Molecular Pharmacology* **2003,** *63* (3), 524-531.

10. Koyano, S.; Kurose, K.; Saito, Y.; Ozawa, S.; Hasegawa, R.; Komamura, K.; Ueno, K.; Kamakura, S.; Kitakaze, M.; Nakajima, T.; Matsumoto, K.; Akasawa, A.; Saito, H.; Sawada, J. I., Functional characterization of four naturally occurring variants of human pregnane X receptor (PXR): One variant causes dramatic loss of both DNA binding activity and the transactivation of the CYP3A4 promoter/enhancer region. *Drug Metabolism and Disposition* **2004,** *32* (1), 149-154.

11. Squires, E. J.; Sueyoshi, T.; Negishi, M., Cytoplasmic localization of pregnane X receptor and ligand-dependent nuclear translocation in mouse liver. *Journal of Biological Chemistry* **2004,** *279* (47), 49307-49314.

12. Augereau, P.; Badia, E.; Balaguer, P.; Carascossa, S.; Castet, A.; Jalaguier, S.; Cavailles, V., Negative regulation of hormone signaling by RIP140. *Journal of Steroid Biochemistry and Molecular Biology* **2006,** *102* (1-5), 51-59.

13. Gurevich, I.; Flores, A.; Aneskievich, B., Corepressors of agonist-bound nuclear receptors. *Toxicology and Applied Pharmacology* **2007,** *223*, 288-298.

14. Watkins, R. E.; Wisely, G. B.; Moore, L. B.; Collins, J. L.; Lambert, M. H.; Williams, S. P.; Willson, T. M.; Kliewer, S. A.; Redinbo, M. R., The human nuclear xenobiotic receptor PXR: structural determinants of directed promiscuity. *Science* **2001,** *292*, 2329-2333.

15. Chrencik, J. E.; Orans, J.; Moore, L. B.; Xue, Y.; Peng, L.; Collins, J. L.; G. Bruce Wisely; Lambert, M. H.; Kliewer, S. A.; Redinbo, M. R., Structural Disorder in the Complex of Human Pregnane X Receptor and the Macrolide Antibiotic Rifampicin. *Molecular Endocrinology* **2005,** *19* (5), 1125-1134.

16. Watkins, R. E.; Maglich, J. M.; Moore, L. B.; Wisely, G. B.; Noble, S. M.; Davis-Searles, P. R.; Lambert, M. H.; Kliewer, S. A.; Redinbo, M. R., 2.1 angstrom crystal structure of human PXR in complex with the St. John's wort compound hyperforin. *Biochemistry* **2003,** *42* (6), 1430-1438.

17. Watkins, R. E.; Davis-Searles, P. R.; Lambert, M. H.; Redinbo, M. R., Coactivator Binding Promotes the Specific Interaction Between Ligand and the Pregnane X Receptor. *Journal of Molecular Biology* **2003,** *331*, 815-828.

18. Xue, Y.; Moore, L. B.; Orans, J.; Peng, L.; Bencharit, S.; Kliewer, S. A.; Redinbo, M. R., Crystal structure of the pregnane X receptor-estradiol complex provides insights into endobiotic recognition. *Molecular Endocrinology* **2007,** *21* (5), 1028-1038.

19. Ding, X. F.; Anderson, C.; Ma, H.; Hong, H.; Uht, R.; Kushner, P.; Stallcup, M., Nuclear receptor-binding sites of coactivators glucocorticoid receptor interacting protein 1 (GRIP-1) and steroid receptor coactivator 1 (SRC-1): multiple binding motifs with different binding specificities. *Molecular Endocrinology* **1998,** *12*, 302-313.

20. Noble, S. M.; Carnahan, V. E.; Moore, L. B.; Luntz, T.; Wang, H.; Ittoop, O. R.; Stimmel, J. B.; Davis-Searles, P. R.; Watkins, R. E.; Wisely, G. B.; LeCluyse, E.; Tripathy, A.; McDonnell, D. P.; Redinbo, M. R., Human PXR forms a tryptophan zipper-mediated homodimer. *Biochemistry* **2006,** *45*, 8579-8589.

21. Teotico, D. G.; Frazier, M. L.; Ding, F.; Dokholyan, N. V.; Temple, B. R. S.; Redinbo, M. R., Active Nuclear Receptors Exhibit Highly Correlated AF-2 Domain Motions. *PLoS Comput Biol* **2008,** *4* (7), e1000111.

22. Glickman, J. F.; Schmid, A.; Ferrand, S., Scintillation proximity assays in high-throughput screening. *Assay and Drug Development Technologies* **2008,** *6* (3), 433-455.

23. Shukla, S. J.; Nguyen, D. T.; MacArthur, R.; Simeonov, A.; Frazee, W. J.; Hallis, T. M.; Marks, B. D.; Singh, U.; Eliason, H. C.; Printen, J.; Austin, C. P.; Inglese, J.; Auld, D. S., Identification of Pregnane X Receptor Ligands Using Time-Resolved Fluorescence Resonance Energy Transfer and Quantitative High-Throughput Screening. *Assay and Drug Development Technologies* **2009,** *7* (2), 143-169.

24. Lichti, K.; Staudinger, J., Novel 'humanized' rodent models for use in the biochemical characterization of PXR-mediated gene activation. *Drug Metabolism Reviews* **2006,** *38*, 209.

25. Ma, X.; Shah, Y.; Cheung, C.; Guo, G. L.; Feigenbaum, L.; Krausz, K. W.; Idle, J. R.; Gonzalez, F. J., The pregnane X receptor gene-humanized mouse: A model for investigating drug-drug interactions mediated by cytochromes P450 3A. *Drug Metabolism and Disposition* **2007,** *35* (2), 194-200.

26. Ai, N.; Krasowski, M. D.; Welsh, W. J.; Ekins, S., Understanding nuclear receptors using computational methods. *Drug Discovery Today* **2009,** *14* (9-10), 486-494.

27. Biswas, A.; Mani, S.; Redinbo, M. R.; Krasowski, M. D.; Li, H.; Ekins, S., Elucidating the 'Jekyll and Hyde' Nature of PXR: The Case for Discovering Antagonists or Allosteric Antagonists. *Pharmaceutical Research* **2009,** *26* (8), 1807-1815.

28. Synold, T. W.; Dussault, I.; Forman, B. M., The orphan nuclear receptor SXR coordinately regulates drug metabolixm and efflux. *Nature Medicine* **2001,** *7* (5), 584-590.

29. Lehmann, J. M.; McKee, D. D.; Watson, M. A.; Willson, T. M.; Moore, J. T.; Kliewer, S. A., The human orphan nuclear receptor PXR is activated by compounds that regulate CYP3A4 gene expression and cause drug interactions. *Journal of Clinical Investigation* **1998,** *102* (5), 1016-1023.

30. Jones, S.; Moore, L. B.; Shenk, J.; Wisely, G. B.; Hamiltion, G.; McKee, D.; Tomkinson, N.; LeCluyse, E.; Lambert, M. H.; Wilson, T.; Kliewer, S. A.; Moore, J., The pregnane X receptor: a promiscuous xenobiotic receptor that has diverged during evolution. *Molecular Endocrinology* **2000,** *14*, 27-39.

31. Chang, T. K. H.; Waxman, D. J., Synthetic drugs and natural products as modulators of constitutive androstane receptor (CAR) and pregnane X receptor (PXR). *Drug Metabolism Reviews* **2006,** *38*, 51-73.

32. Huang, H.; Wang, H.; Sinz, M.; Zoeckler, M.; Staudinger, J.; Redinbo, M.; Teotico, D.; Locker, J.; Kalpana, G.; Mani, S., Inhibition of drug metabolism by blocking the activation of nuclear receptors by ketoconazole. *Oncogene* **2007,** *26*, 258-268.

33. Wang, H.; Huang, H.; Li, H.; G.Teotico, D.; Sinz, M.; Baker, S. D.; Staudinger, J.; Kalpana, G.; Redinbo, M. R.; Mani, S., Activated Pregnenolone X-Receptor Is a Target for Ketoconazole and Its Analogs. *Clinical Cancer Research* **2007,** *13* (8), 2488-2495.

34. Ekins, S.; Chang, C.; Mani, S.; Krasowski, M. D.; Reschly, E. J.; Iyer, M.; Kholodovych, V.; Ai, N.; Welsh, W. J.; Sinz, M.; Swaan, P. W.; Patel, R.; Bachmann, K., Human pregnane X receptor antagonists and Agonists define molecular requirements for different binding sites. *Molecular Pharmacology* **2007,** *72* (3), 592-603.

35. Ekins, S.; Kholodovych, V.; Ai, N.; Sinz, M.; Gal, J.; Gera, L.; Welsh, W. J.; Bachmann, K.; Mani, S., Computational Discovery of Novel Low Micromolar Human Pregnane X Receptor Antagonists. *Molecular Pharmacology* **2008,** *74*, 662-672.

36. Das, B. C.; Madhukumar, A. V.; Anguiano, J.; Kim, S.; Sinz, M.; Zvyaga, T. A.; Power, E. C.; Ganellin, C. R.; Mani, S., Synthesis of novel ketoconazole derivatives as inhibitors of the human Pregnane X Receptor (PXR; NR1I2; also termed SXR, PAR). *Bioorganic & Medicinal Chemistry Letters* **2008,** *18* (14), 3974-3977.

37. Dorn, I.; Neumier, K.; Tampé, R., Molecular Recognition of Histidine-Tagged Molecules by Metal-Chelating Lipids Monitored by Fluorescence Energy Transfer and Correlation Spectroscopy. *Journal of the American Chemical Society* **1998,** *120*, 2753-2763.

38. Lata, S.; Reichel, A.; Brock, R.; Tampé, R.; Piehler, J., High-Affinity Adaptors for Switchable Recognition of Histidine-Tagged Proteins. *Journal of the American Chemical Society* **2005,** *127*, 10205-10215.

39. Moore, J.; Kliewer, S. A., Use of the nuclear receptor PXR to predict drug interactions. *Toxicology* **2000,** *153*, 1-10.

40. Johnson, D. R.; Li, C.-W.; Chen, L.-Y.; Ghosh, J. C.; Chen, J. D., Regulation and Binding of Pregnane X Receptor by Nuclear Receptor Corepressor Silencing Mediator of Retinoid and Thyroid Hormone Receptors (SMRT). *Molecular Pharmacology* **2006,** *69* (1), 99-108.

41. Thompson, N. L.; Pero, J. K., Total internal reflection-fluorescence correlation spectroscopy. In *Reviews in Fluorescence 2006*, Geddes, C.; Lakowicz, J., Eds. Kluwer Academic/Plenum Press: New York, 2006; Vol. 3, pp 215-237.

42. Allen, N. W.; Thompson, N. L., Ligand binding by estrogen receptor beta attached to nanopsheres measured by fluorescence correlation spectroscopy. *Cytometry Part A* **2006,** *69A*, 524-532.

43. Thompson, N. L.; Pero, J. K., Total internal reflection fluorescence microscopy: applications in biophysics. In *Fluorescence Spectroscopy in Biology Advanced Methods and their Applications to Membranes, Proteins, DNA, and Cells*, Hof, M.; Hutterer, R.; Fidler, V., Eds. Springer-Verlag: Berlin Heidelberg, 2005; Vol. 3, pp 79-103.

44. Holden, M. A.; Cremer, P. S., Microfluidic tools for studying the specific binding, adsorption, and displacement of proteins at interfaces. *Annual Review of Physical Chemistry* **2005,** *56*, 369-387.

45. Li, C. W.; Dinh, G. K.; Chen, J. D., Preferential Physical and Functional Interaction of Pregnane X Receptor with the SMRT alpha Isoform. *Molecular Pharmacology* **2009,** *75* (2), 363-373.

46. Zhou, G.; Cummings, R.; Li, Y.; Mitra, S.; Wilkinson, H.; Elbrecht, A.; Hermes, J.; Schaeffer, J.; Smith, R.; Moller, D., Nuclear receptors have distinct affinities for coactivators: characterization by fluorescence resonance energy transter. *Molecular Endocrinology* **1998,** *12*, 1594-1604.

47. Chandra, V.; Huang, P. X.; Hamuro, Y.; Raghuram, S.; Wang, Y. J.; Burris, T. P.; Rastinejad, F., Structure of the intact PPAR-gamma-RXR-alpha nuclear receptor complex on DNA. *Nature* **2008,** *456* (7220), 350-U33.

Chapter 3

Experiments toward Understanding the Molecular Binding of the Discoidin Domain Receptor 2 to Monomeric and Fibrillar Collagen Type

3.1 Introduction

Collagens are the most abundant proteins in mammals, comprising 30% of the total protein observed.[86] The vertebrate superfamily includes over 50 collagens and collagen-like proteins, and to date there are 28 identified types of collagen. Collagens are a major component of the extracellular matrix, which acts as a scaffold for tissues and is critical for the biomechanical properties of tissues. Collagens are substantial constituents of skin, tendon, bone, ligament, cornea, and cartilage, and mutations in collagen genes cause numerous diseases including osteoporosis, osteoarthritis, tissue fibrosis, and arterial aneurysms.[87] Collagens also play important roles in cell adhesion and migration during growth, differentiation, morphogenesis, and wound healing through interactions with other matrix proteins and cell surface receptors.[88] Collagens are classified by their ability to form supramolecular structures or networks and can be divided into three major categories, fibrillar collagens, non-fibrillar collagens, and other collagens such as the transmembrane collagens.[89, 90]

The fibrillar collagens, types I-III, V, and XI, are characterized by the presence of a 300 nm triple helical domain that in collagen types I-III is flanked on either end by two short, globular peptides know as the telopeptides. Each collagen molecule contains three left-handed, helical polypeptide chains containing approximately 1000 amino acids, termed α chains, which coil around each other to form a right-handed triple helix. Each α chain consists of repeating G-X-Y sequences, where X and Y can be any amino acid. The three α chains in a collagen molecule may be identical or different, depending on the type of collagen.[88-90] Glycine is required at every third position to allow tight packing within the core of the triple helix, stabilizing the molecule through hydrogen bonding of

the glycines and other residues.[91] The X and Y residues are exposed on the surface of the molecule and are frequently proline or hydroxyproline, respectively. These residues also stabilize the triple helix by restricting flexibility about the peptide bond and through interchain hydrogen bonding. At high temperatures, hydrogen bonding is disrupted causing the polypeptide chains to melt and denature into random coils. In cells, collagen molecules are synthesized and secreted in the form of a soluble precursor, known as procollagen, that contains large, globular propeptide domains on the N and C-terminals. Upon secretion, the propeptide regions are cleaved by specific proteinases and the tropocollagen molecules (triple-helical collagen monomers) then spontaneously self-assemble into fibrils containing parallel arrays of quarter-staggered molecules, which are stabilized by covalent cross-linking. As adjacent collagen monomers overlap each other by 234 amino acids, this gives rise to a repeating axial gap-overlap structure know as the D period, which is visible by electron microscopy and appears as an alternating pattern of light and dark regions (Figure 3.1). The characteristic length of the D period ranges from 64-67 nm, depending on the tissue type, and the length of one collagen molecule is approximately 4.4 D-periods.[89, 90] Fibril diameters range from 20-500 nm in vertebrates and depend on the tissue type and stage of development.[92] While the formation of fibrils *in vivo* and *in vitro* has been the subject of study for over 50 years, major questions concerning the mechanisms of fibril assembly, the regulation of fibril length and diameter, and the subsequent formation of hierarchical, macromolecular structures from fibrillar subunits still remain unresolved.

Fibrilogenesis *in vitro* has been widely studied, in most cases using purified, acid-soluble collagen type I, the most abundant collagen in mammals, from skin or tendon.[92]

When the pH of acid-soluble collagen is adjusted to around neutral and the solution warmed to near physiological temperature, collagen fibrils spontaneously form due to an increase in solvent entropy arising from burying of surface exposed hydrophobic residues within the fibril. Fibril formation proceeds via a nucleation and growth mechanism.[89] Some evidence suggests that hydrogen bonding between polar residues and other electrostatic forces may help drive fibrillogenesis.[93] The structure of the resulting fibrils is dependent on concentration,[94] pH,[95, 96] temperature,[97] ionic strength,[95, 96] ionic composition,[98] and presence of the telopeptides,[99, 100] and these conditions determine whether D-periodic or non-banded collagen filaments are observed.[101] As such, there are several protocols given in the literature for the formation of collagen fibrils with native D-periodicity and randomly aligned fibrils.[92, 97, 101] As collagen alignment *in vivo* determines biomechanical properties such as tensile strength[102] and has been shown to direct cell proliferation and migration,[103] obtaining collagen gels and films with highly oriented collagen fibers is desirable but has proven to be more challenging, often requiring the use of strong magnetic fields,[104, 105] gravity-driven flow,[106] or interstitial flow.[107] Alternatively, a simple method for aligning collagen gels using small magnets and streptavidin-coated magnetic beads has been presented, which resulted in good alignment of collagen in 80% of the trials.[108] Aligned collagen has also been observed in microfluidic channels of less than 100 μm in width when flow was induced prior to gelation.[109]

Given the structural complexity and functional diversity of collagens, it is not surprising that several different types of cell-surface collagen receptors have been identified, including integrins, glycoprotein VI, leukocyte-associated IG-like receptor-1,

members of the mannose receptor family, and the receptor tryrosine kinases called the discoidin domain receptors.[88, 110] Receptor tyrosine kinases (RTKs) are a family of proteins which convert extracellular stimuli into cellular response. RTKs are transmembrane proteins that contain a large, glycosylated extracellular domain that is responsible for ligand binding, a single transmembrane region, and a cytoplasmic domain that contains a tryrosine kinase domain. Depending on the class of receptor, RTK's exist as monomers that undergo dimerization upon ligand binding or exist as preformed dimers. In both systems, a conformational change in the intracellular tyrosine kinase domain is induced through ligand binding in the extracellular domain, resulting in activation of the receptor through cross phosphorylation of the two tyrosine kinases, a process known as autophosphorylation. In turn, the activated receptor phosphorylates other cytosolic proteins, triggering a cascade of signaling processes.[111]

The discoidin domain receptors, DDR1 and DDR2, are unusual members of the receptor tyrosine kinase family in that they are not activated by soluble growth factors but by fibrillar and non-fibrillar collagens.[112, 113] DDR1 has been activated by all collagens tested, including types I-VI, and type VIII.[2] Until recently when it was shown to be activated by collagen type X,[114] it was believed that DDR2 was only activated by fibrillar collagens, specifically types I-III and V. Upon binding to collagen, DDRs exhibit unusually slow activation with maximal autophosphorylation occurring 90 minutes to 2 hours after initial stimulation, which is significantly slower than other RTKs that become fully activated within minutes. Heat denatured collagens (gelatins) do not induce receptor autophosphorylation, indicating that the triple helical nature of collagen is necessary for receptor recognition and activation.[2] Phosphorylation of DDRs can be

sustained for up to 18 hours after activation, and this, in conjunction with its slow activation, suggests that the DDRs may be involved in long term monitoring of the extracellular environment rather than mediating acute responses.[112] The DDRs regulate cell adhesion, proliferation, and remodeling of the extracellular matrix and control the expression of matrix metalloproteinases (MMPs), enzymes that degrade components of the ECM including collagen.[2, 88]

The DDRs are widely and differentially expressed in fetal and adult tissues, as well as normal and malignant tissue.[2, 115] DDR1 is mostly found in epithelial cells and leukocytes, where DDR2 is a mesenchymally (cells that give rise to such structures as connective tissues, blood, lymphatics, bone, and cartilage) expressed receptor. Specific examples of DDR function can be observed through knockout studies in mice. DDR1 knockouts indicate that this receptor is an important regulator of mammary glands and kidneys. DDR2 knockouts exhibit dwarfism, indicating DDR2 regulates the growth of long bones through chondrocyte proliferation. The DDRs are implicated in several diseases including tumor progression, atherosclerosis, inflammation, and tissue fibrosis (reviewed in [2]). While many studies have been conducted to understand the role of the DDRs in disease, most work has been performed using type I collagen, neglecting the contribution of other collagens in disease progression.

While following the structural paradigm for RTKs, DDR structure differs in several ways. The ligand binding function is a N-terminal, 160 amino acid discoidin domain homology region that was first identified in the slime mold protein discoidin I from *Dictyostelium discoideum*. This homology is found in more than a dozen functionally different mammalian proteins, including transmembrane receptors as well as

secreted proteins. This region is followed by an approximately 200 amino acid domain unique to DDR receptors, sometimes referred to as the stalk region, whose function has yet to be determined. As in all RTKs, the DDRs have a single transmembrane region followed by an unusually large cytosolic juxta-membrane region. While the function of this region is unknown, it has been speculated that this region may play an autoinhibitory role contributing to the slow activation of the receptor. The C-terminal of the protein contains a well conserved tyrosine kinase domain.[2] To date, crystal structures for the DDR discoidin homology and full length receptors have not been elucidated. Consequently, it is not yet understood how collagen binding in the ECD by the discoidin domain translates into activation in the cytosolic tyrosine kinase domain, however; there is evidence to suggest that internalization of the receptor after ligand binding may play a role in its activation.[116]

Despite the lack of a crystal structure, several studies have been conducted to determine the structure of the discoidin domain (DS). Using known crystal structures from proteins containing homologous discoidin domains, such as the C2 domains from blood coregulation factors V and VIII, as a reference, the structures of the discoidin domains of DDR1 and DDR2 were theoretically modeled.[117, 118] Both models predict a central eight-stranded β-barrel and four finger-like loops protruding from one side of the barrel that are highly conserved between the DDRs. These structures also implicate three of the four conserved loops in collagen binding. More recently, a NMR study determined the solution structure of the discoidin domain of DDR2 and mapped its binding interface with a collagen type II fibril by transferred cross-saturation (TCS) methods.[119] In agreement with previous theoretical structures, overlaying of 20 backbone models shows

the discoidin domain contains eight major β strands that are arranged in two anti-parallel sheets of five and three, forming a β-barrel with a jellyroll topology commonly observed in other DS domains. Three interconnecting straight segments close the bottom of the β-barrel core, and the N and C-terminals are connected with a disulfide bridge between Cys30 and Cys185. On "top" of the β-barrel core are six juxtaposed loops (L1-L6), three (L1, L2, and L4) of which significantly differ in structure from other DS domains. With the exception of L5, these loop regions form the collagen binding site, which is described as a trench with a curved surface. The overall fold is stabilized by a disulfide bridge between Cys73 and Cys177 that links loops L2 and L6 and makes the trench wide and hydrophobic. Mutagenesis and TCS studies revealed that 13 trench residues, which are a mixture of hydrophobic and charged amino acids, are essential for collagen recognition and binding. As the DS domains of the DDRs have an overall sequence identity of 59%, it is likely that the structure of DDR1 is similar to DDR2 but with minor differences that would account for the observed binding preferences for different collagens. Concurrently, a comparison of the two sequences indicates that 11 of the 13 residues identified as essential to ligand binding are conserved between the two proteins.[120]

In addition to determining the structure of the discoidin domain, recent studies have focused on mapping the DDR binding site(s) on fibrillar collagens. Using deletion mutants of collagen type II, which contain three identical α chains, where one of the four repeating D-periods was removed, it was determined that the D2 region is required for binding and activation of DDR2.[121] In a second study, a set of 56 overlapping triple-helical peptides designed to specifically map the entire triple helical domain of collagen II were used to determine specific peptide sequences recognized and bound by DDR2.

These studies found that GVMGFO, where O is hydroxyproline, is the minimal collagen sequence required for DDR2 binding, however; autophosphorylation studies indicated that a longer peptide sequence, GPRGQOGVMGFO, is required for activation of the receptor. This repeat is conserved in collagen type I and III, suggesting that this sequence may be a conserved motif recognized by the DDR proteins for collagen binding, and is found in the D2 region of collagen II, in good agreement with the previous study.[120] The ability of these peptides to activate DDR1 was not investigated.

While several studies have examined the binding of DDR1 and DDR2 to collagen, these studies have provided more questions than answers about the nature of DDR-collagen interactions. Many studies, which use the soluble, extracellular domain (ECD) of the DDRs, have indicated that receptor dimerization[117] or oligomerization[122, 123] is necessary for collagen binding, however; other studies have observed collagen binding by monomeric ECD receptors.[118, 119] Despite the plethora of studies conducted, the relationship between DDR binding and the structural organization of collagen has largely been neglected. Therefore, the goal of this work is to use TIRF to measure the difference in binding affinity between fluorescently-labeled, monomeric and dimeric ECD-DDR2, to fused-silica slides coated with either monomeric collagen type I or with aligned or unaligned collagen type I fibrils. As this work is still in progress, this chapter will describe the expression, purification, and fluorescent-labeling of ECD-DDR2. This chapter will also include a detailed account of the various methods employed to generate fused-silica slides with aligned or unaligned collagen fibrils or collagen monomers, which were characterized using fluorescence microscopy and atomic force microscopy (AFM).

3.2 Materials and Methods

3.2.1 Materials

All chemicals were purchased from Fisher Scientific (Fairlawn, NJ) unless otherwise specified. Deionized (DI) water was generated using a NANOpure® II water purification system (Barnstead International, Dubuque, IA). Acid-soluble collagen type I (2.9 mg/mL, 99.9% pure, in acetic acid pH=2) from bovine skin was commercially purchased (PureCol™, Inamed Biomaterials) and used in all collagen experiments. The collagen was neutralized on ice immediately prior to use by making 1:1:8 solution of 10x MEM pH=5.0 (Sigma-Aldrich, M3024), 0.2 N HEPES pH=9.0, acid-soluble collagen (collagen$_{MEM}$) or was neutralized by dialyzing into PBS (50 mM sodium phosphate, 150 mM sodium phosphate, 0.01% sodium azide, pH=7.4) overnight at 4°C (collagen$_{PBS}$). All ECD-DDR2 cell lines were provided by Dr. Edie Goldsmith (Department of Cell and Developmental Biology, University of South Carolina).

3.2.2 Collagen Alignment and Characterization

3.2.2.*i* *Slide Cleaning and Surface Modification*

Fused silica slides (1" x 1" x 1 mm, cut in house from 3" x 1" x 1 mm slides, Quartz Scientific Inc, Fairport Harbour, OH) were cleaned using either detergent cleaning, base cleaning, or acid cleaning, and glass microscope slides (Gold Seal® Products, Portsmouth, NH) and Fisherbrand cover glasses (No. 1 Circles, 12 mm dia; Fisher Scientific) were cleaned in detergent. Detergent cleaning was carried out by boiling slides in a 10% solution of 7X -ICN detergent (MP BioMedicals, Solon, OH), by bath sonicating for 30 minutes and by thoroughly rinsing with DI water. The slides were then sonicated in DI water for an additional 30 minutes, were rinsed again, and were

dried at 160°C. Base cleaning was carried out by soaking slides in a solution containing 120 g of potassium hydroxide dissolved in 120 mL of DI water and diluted to 1 L with 95% ethanol (AAPER Alcohol, Shelbyville, KY) for 10 minutes, washing with 95% ethanol, and then rinsing with DI water until the pH of the solution returned to neutral. Acid cleaning was performed by soaking slides in a 3:1 solution of concentrated sulfuric acid to 30% hydrogen peroxide for 45 minutes and then rinsed with DI water until a neutral pH was obtained.

Fused silica substrates were surface modified using silane chemistry or using poly-L-Lysine. Poly-L-Lysine slides were made by soaking the slides for 15 minutes in a 0.01% poly-L-lysine solution (Sigma-Aldrich, St. Louis, Mo) and by rinsing in DI water. After base cleaning, fused silica slides were functionalized using a method derived from Lom et. al.[124] and Bhatia et. al.[125] Briefly, the slides were plasma cleaned in argon gas for 15 minutes (PDC-3XG, Harrick Scientific, Ossining, NY), sonicated in a 1% (v/v) solution of N-2-aminoethyl-3-aminopropyl-trimethoxysilane (EDS) (Sigma-Aldrich) in 95% ethanol for 2 minutes, were rinsed in 95% ethanol, were rinsed in 0.22 μm filtered DI water, and were dried at 125°C for 25 minutes. After cooling to room temperature, the slides were incubated in a 2.5% (v/v) solution of glutaraldehyde in PBS for 1 hour, before rinsing with filtered, DI water. The slides were left to dry overnight at room temperature or for 1.5 hours at 60°C.

3.2.2.*ii* *Aligned Collagen Films*

Aligned collagen films were created by tilting a fused silica slide at a 45° angle and placing a rubber cell-scraper approximately 90° relative to the slide and 0.25" from the top of the slide. One hundred to 200 μL of collagen was pipetted onto the slide and

allowed to pool along the cell scraper. The scraper was then slid down the length of the slide to induce flow and evenly coat the slide with the collagen mixture. For collagen samples on bare, fused-silica surfaces, slides were illuminated with UV radiation for 10 minutes in a cell culture hood prior to incubation. The slides were incubated at 37°C for 1 hour to allow collagen to gel or 2.5 hours to produce a dried collagen film. After incubation, slides with collagen were attached via double-sided tape (3M Corp., Part No. 021200-64988) to 3" x 1" x 1 mm glass microscope slides and washed with 600 μL of PBS. The same procedure was used for poly-L-lysine and EDS coated fused silica slides. Films were observed for fibril formation using light microscopy.

3.2.2.*iii* *Unaligned Collagen Films*

Monomeric, unaligned collagen films were generated by incubating Fisherbrand cover glasses (No.1, 12 mm dia) or siliconized glass cover slides (12 mm dia; Hampton Research, Aliso Viejo, CA) for 30 minutes at 37°C in a 10 μg/mL collagen type I solution in 55 mM sodium citrate pH=4.5, 100 mM sodium chloride buffer. Slides were rinsed with 0.22 μm filtered, DI water and dried under a stream of nitrogen. Films were analyzed by AFM to characterize surface properties (see below). Films of unaligned, collagen type I fibrils were generated by pipetting 100-200 μL of collagen$_{MEM}$ onto fused silica substrates that were laid flat and incubating at 37°C for 1 or 2.5 hours. This procedure was repeated using poly-L-lysine and EDS coated fused silica slides. Slides were attached to microscope slides using double-sided tape, were rinsed with 600 μL of PBS, and observed under light microscopy.

3.2.2.*iv* *Fluorescence Imaging of Collagen Films*

Collagen$_{PBS}$ was diluted to 0.25 mg/mL, 0.5 mg/mL, or 1.0 mg/mL, and fluorescein isothiocyanate (FITC) labeled collagen type I (Sigma-Aldrich C4361) was added to a final concentration of 1% in each sample. Aligned and unaligned collagen films on EDS coated fused silica slides were generated as described using 200 μL of collagen$_{PBS}$ with a 2.5 hour incubation time, attached to glass microscope slides, and rinsed with 600 μL of PBS. Images were obtained using epifluorescence on an instrument consisting of an inverted microscope (Zeiss Axiovert 35; 40x water 0.75 N.A. objective)**,** an argon ion laser (Innova 90-3, Coherent, Palo Alto, CA) and a charge-coupled device (CCD) (Photometrics CH250) imaging detector with Photometrics PMIS Image 200 Processing Software (Photometrics Inc., Tucson, AZ). All images were taken using an excitation wavelength of 488.0 nm and an appropriate long-pass filter for fluorescence detection.

3.2.2.*v* *AFM Imaging*

Monomeric, unaligned collagen samples were made as described above, and the glass coverslips were attached to round, metal disks using double-sided tape. Films of collagen fibrils were formed by adding 20 μL of 0.10 mg/mL, 0.25 mg/mL, or 1.0 mg/mL collagen$_{PBS}$ to 18 mm round glass coverslips coated with EDS and by incubating at 37°C for 2 hours. The films were rinsed with 0.22 μM filtered, DI water and attached to metal disks as described above. AFM images were captured in air using either a Nanoscope III or IIIa (Digital Instruments, Santa Barbara, CA) microscope in tapping mode. Pointprobe Plus Silicon-SPM tips (Agilent Technology, Tempe, AZ) with resonance frequencies of approximately 150 to 160 kHz were used for imaging. Images

were collected at a speed of 3 Hz with an image size of 1 μm^2 or 4 μm^2 at 512 x 512 pixel resolution. Images were analyzed using Nanoscope III (R) v5.12r5 software (Veeco, Santa Barbara, CA).

3.2.3 Expression, Purification, and Characterization of DDR2

3.2.3.*i* *Cell Lines and Culture*

Briefly, the entire ECD of mouse DDR2 (amino acids 1-399) was cloned with a C-terminal 6x His tag (ECD-DDR2-His) into human embryonic kidney 293 cells (HEK 293). A second cell line was generated in which Cys348 of the ECD was mutated to another amino acid and was expressed in HEK293 cells (*m*ECD-DDR2-His). Additionally, a fusion protein containing the ECD of DDR2, a 6x His tag, and a C-terminal enhanced green fluorescent protein (EGFP) (ECD-DDR2-EGFP) was expressed in Chinese hamster ovary cells (CHO). All cell lines excreted soluble ECD-DDR2 proteins and were cultured in DMEM/F-12 supplemented with 10% fetal calf serum, 800 μg/mL of Geneticin, 100 units/mL penicillin, 100 μg/mL streptomycin, 1 mM sodium pyruvate, and 2 mM L-glutamine (all reagents were Gibco® brand; Invitrogen Corp., Carlsbad, CA) in a humidified incubator at 37°C with 5% CO_2.

3.2.3.*ii* *Purification of DDR2*

Soluble ECD-DDR2 proteins were purified using nickel nitrilotriacetic acid (Ni-NTA) or affinity column chromatography. Media from cell culture was spun at 5000 rpm in 50 mL conical tubes to remove cell debris prior to being passed through a 0.22 μm bottle-top filter (Corning Inc., Lowell, MA). For Ni-NTA chromatography, the pH of the media was adjusted by adding 50 mM sodium phosphate pH=8.0, 150 mM sodium chloride, and 10 mM imidazole (final concentrations) and passed over Ni-NTA agarose

(Qiagen, Valencia, CA) equilibrated in 50 mM sodium phosphate pH=8.0, 300 mM sodium chloride, and 20 mM imidazole (wash buffer) using gravity-flow columns. Wash buffer equal to twice the volume of media was then passed through the column, before eluting with buffer containing 50 mM sodium phosphate pH=8.0, 300 mM sodium chloride, and 250 mM imidazole. For affinity chromatography, anti-DDR2 antibodies (SC-7555, Santa Cruz Biotechnologies Inc., Santa Cruz, CA) were coupled to cyanogen bromide-activated-Sepahrose® 4-B agarose following the manufacturer's protocol (Sigma-Aldrich, St. Louis, MO). The resulting resin was equilibrated in a 50 mM Tris pH=7.5, 150 mM sodium chloride, 0.1% Tween-20 buffer (buffer I) in a gravity flow column prior to passing media through the column. The column was then washed, with a volume equal to that of the media for each, with buffer I and buffer II (50 mM Tris pH=7.5, 500 mM sodium chloride, 0.1% Tween-20) and was eluted with a 100 mM sodium acetate pH=4.0, 500 mM sodium chloride buffer. For both methods, fractions containing ECD-DDR2 were pooled, dialyzed into PBS, and concentrated using Amicon Ultra MWCO 10,000 (Millipore, Billerica, MA). Concentration of the samples was determined using Bio-Rad protein assay with BSA standards (Bio-Rad Laboratories Inc., Hercules, CA). The purity was confirmed by SDS-PAGE using 7.5% or 10% Tris-HCl ready gels with silver staining (GE Healthcare, Piscataway, NJ).

3.2.3.*iii* *Western Blotting*

To confirm production of ECD-DDR2, samples with a concentration of 1 μM total protein were diluted 1:1 with 2x SDS-Loading Buffer (250 mM Tris-base pH=6.9, 40% (v/v) glycerol, 9.25% (w/v) SDS, 0.1% bromophenol blue) with or without β-mercaptoethanol (10% (v/v)) and loaded onto a 10% Tris-HCl ready gel with Magic

Mark® molecular weight marker (MW) (Invitrogen). The gel was run at 120 V for 20 minutes, then at 180 V until complete, before transferring to a PVDF membrane in 20 mM Tris-HCl, 20 mM glycine buffer at 350 mA for 60 minutes at 4°C. The membrane was blocked in 10 mM Tris pH=7.5, 150 mM sodium chloride, 5% (w/v) non-fat dried milk, and 0.05% Tween-20 buffer (TBST) for 45 minutes, incubated with 1:1000 dilution of 1506 antibody (rabbit anti-(ECD-DDR2) antibody produced in E. Goldsmith's lab) in TBST for 1 hour, and washed three times for 15 minutes with TBST. The blot was then incubated with 1:2000 dilution of HRP-conjugated goat-anti-rabbit antibody (Zymed® Laboratories, Inc., San Francisco, CA) in TBST, was washed an additional three times for 15 minutes with TBST, and was thoroughly washed with DI water to remove the milk. The blocking, incubation, and washing steps were all completed at room temperature. In the dark room, the blot was incubated with ECL detection chemical (Pierce Biotechnology, Rockford, IL) for 2 minutes and was exposed to Amersham Hyperfilm ECL photosensitive film (GE Healthcare) for 16 seconds. The film was developed using standard procedures.

3.2.3.*iv* *Dynamic Light Scattering*

To accurately determine the molecular weight, ECD-DDR2 samples were concentrated to 1.0 mg/mL using Micron YM-10 concentrators (Millipore) and were run on a Wyatt DAWN EOS light scattering instrument interfaced to an Amersham Biosciences ÄKTA FPLC with a Superose™ 12 column at a flow rate of 0.25-0.5 mL/min in PBS with or without 5 mM DTT.

3.2.4 FPLC

To separate monomers from dimers, ECD-DDR2 samples were concentrated to 1 mg/mL using Micron YM-10 concentrations (Millipore) and were 0.22 μm filtered using Ultrafree®-MC centrifugal filters (Millipore). Approximately 0.5 mL of sample was loaded onto a Superose™ 12 (10/300 GL, GE Healthcare) or a Superdex™ 200 (10/300 GL, GE Healthcare) column equilibrated in PBS or PBS with 5 mM DTT using an ÄKTA FPLC UPC-900 (GE Healthcare) with a constant flow rate of 0.5 mL/min. One milliliter fractions were collected and analyzed using SDS-PAGE with 10% Tris-HCl gels and silver staining.

3.2.5 Fluorescent Labeling

ECD-DDR2 and IgG Fab (Zymed® Laboratories, Inc.) were labeled with Alexa Fluor® 514 carboxylic acid, succinimidyl ester (A514) according to manufacturer's protocols (Molecular Probes, Carlsbad, CA). Protein was dialyzed into PBS in the presence or absence or 10-fold molar excess TCEP, was concentrated between 0.4 to 0.8 mg/mL and, after addition of 20 to 25-fold molar excess of fluorophore to each sample, allowed to react at room temperature (Fab) or 4°C (for ECD-DDR2) for 2 hours. To remove the free dye, samples were run down a G-25 Sephadex® column (Sigma-Aldrich), and eluted fractions were pooled and dialyzed overnight at 4°C into PBS. The labeling ratio was determined spectrophotometrically using CF_{280}=0.18, where CF is correction factor ($\varepsilon_{\lambda=280}/\varepsilon_{\lambda=517}$), and $\varepsilon_{\lambda=517}$=80,000 $M^{-1}cm^{-1}$ for Alexa Fluor® 514, and $\varepsilon_{\lambda=280}$=75,000 $M^{-1}cm^{-1}$ for Fab. By determining the concentration of ECD-DDR2 using Bio-Rad Protein Assay and BSA standards and by taking the $A_{\lambda=280}$ of same sample, the $\varepsilon_{\lambda=280}$ for DDR2 was calculated to be 47,000 $M^{-1}cm^{-1}$.

3.2.6 TIRF Microscopy

3.2.6.*i* *Positive and Negative Controls*

Positive control slides of aligned collagen films were made and tested for consistency. The films were generated using 200 µL of collagen$_{PBS}$ incubated on EDS-coated, fused-silica slides for 2.5 hours. The slides were attached to glass microscope slides and washed with 600 µL of PBS. To block non-specific absorption, 100 µL of 10 mg/mL ovalbumin were added to the slides and incubated for 30 minutes at room temperature. Prior to TIRF measurements, 150 µL of 1 µM ECD-DDR2-A514 in 10 mg/mL ovalbumin were added, and slides were sealed with vacuum grease.

Three different types of samples were evaluated for their use as negative controls for TIRF microscopy. EDS-coated, fused-silica slides were attached to glass microscope slides using double-sided tape, and 100 µL of a 50 mg/mL solution of bovine serum albumin (BSA) (Sigma-Aldrich) were pipetted between the slides. The slides were incubated at room temperature for 1 hour. Aligned collagen slides were generated as described above by incubating 150 µL of collagen$_{PBS}$ on an EDS-coated, fused-silica slide for 1 hour at 37°C. Additionally, 150 µL of a 2% solution of gelatin type B from bovine skin (Sigma-Aldrich) were pipetted onto a fused-silica coverslip, incubated at 37°C for 1 hour, and attached to a glass microscope slide with double-sided tape. All samples were washed with 600 µL of PBS prior to adding 100 µL of 10 mg/mL ovalbumin, which was allowed to incubate for 30 minutes at room temperature. To each slide, 150 µL of 1 µM Fab-A514 in 10 mg/mL ovalbumin were added, and slides were sealed with vacuum grease in preparation for TIRF measurements.

3.2.6.*ii* *Instrumental Setup*

Through prism total internal reflection experiments were carried out on the instrument described previously. Fluorescence intensity measurements were collected for 30 seconds using a single-photon counting photomultiplier (RCA C31034A, Lancaster, PA) interfaced to a PC-based correlater board (model 5000/E, ALV). All experiments were conducted at an excitation wavelength of 514 nm, a laser power of 50 μW, and at 25^{o}C.

3.3 Results

3.3.1 Aligned and Unaligned Films of Collagen Fibrils

As seen using light microscopy, aligned and unaligned films of collagen fibrils did not form on bare fused-silica surfaces, even with UV cross-linking. Upon further investigation, it was discovered that immediately after incubation loosely adhered, thin films of collagen fibrils were on the surface, but these films detached and were rinsed away during subsequent wash steps. This process was found to be independent of the method used to clean the slides. Coating the fused-silica slides with poly-L-lysine resulted in only patchy coverage of collagen fibrils. Increasing the amount of collagen that was incubated on the slide also did not significantly increase the observed surface coverage. Fused-silica slides that were covalently bound with N-2-aminoethyl-3-aminopropyl-trimethoxysilane (EDS) showed improved and complete surface coverage when incubated at 37°C for 1 and 2.5 hours, respectively. Dialyzing collagen into PBS overnight at 4°C rather than neutralizing immediately prior to film formation was also found to improve film coverage. However, increasing the incubation time resulted in

partial alignment of the unaligned films due to rings forming as the sample dehydrated. These rings were not observed in aligned collagen samples, and the difference is most likely due to the angle at which the slides were incubated. Therefore, a slightly different procedure that keeps the sample hydrated throughout the entire incubation period will most likely need to be used for unaligned films of collagen fibrils.

3.3.2 Fluorescent Imaging of Collagen Fibril Films

To verify the alignment of collagen fibrils, collagen films that were 1% labeled with FITC were made on EDS treated fused-silica slides and observed using epifluorescence. As shown in Figure 3.2, for aligned collagen films light and dark parallel stripes, which increased in width as the concentration of collagen increased, were observed. The stripes extended along the entire length of the sample, indicating complete surface coverage. Similar morphology was observed for unaligned films, indicating that collagen fibril alignment was occurring in these samples, as previously indicated by light microscopy.

3.3.3 AFM Imaging

To characterize the molecular organization of collagen in unaligned films, atomic force microscopy (AFM) was used to probe collagen films generated by adsorption of acidic or neutralized collagen on bare, siliconized, or EDS-treated glass surfaces. To generate collagen fibrils, unaligned films were made on EDS coated slides using solution concentrations of 0.10 mg/mL, 0.25 mg/mL, or 1.0 mg/mL of collagen$_{PBS}$. At a concentration of 1.0 mg/mL, surface features could not be identified due to too much protein being adsorbed onto the surface. For samples made with 0.10 mg/mL of collagen, short fibrils with a banded appearance signifying D-periodicity were observed

on the surface with heights on the order of 10 nm. At a concentration of 0.25 mg/mL, extended collagen fibrils exhibiting D-periodicity with lengths on the order of several microns and with observed heights in the range of 50 to 75 nm were seen in addition to the short, banded fibrils, as shown in Figure 3.3 (a) and (b). Non-banded, filamentous collagen fibrils were not present in any of the images. Together, these results indicate that the procedures used to generate collagen films produce fibrils in their native D-periodic form.

Collagen films produced from adsorbing collagen at an acidic pH onto siliconized and untreated glass surfaces had very different surface morphologies than collagen films generated at neutral pH. As seen in figure 3.3 (c), the surface morphology of siliconized glass that was incubated in 10 μg/mL of collagen in 55 mM sodium citrate pH=4.5, 150 mM sodium chloride buffer is characterized by branching, filamentous structures. Surface analysis revealed a mean height of 2.80 ± 1.45 nm overall, with heights of 4 to 6 nm in the thicker branches (i.e. lighter). As a collagen molecule has a diameter of 1.5 nm, this roughly corresponds to 2 to 3 monolayers of collagen being absorbed onto the surface. For the untreated glass surfaces, a mean height of 1.67 ± 0.6 nm was observed, roughly corresponding to a monolayer of collagen, and the surfaces appeared to be more evenly coated. AFM images of bare glass (data not shown) did not show any defining surface characteristics and had a mean roughness of approximately 0.2 nm. Overall, these images show that non-specifically adsorbing collagen at an acidic pH gives surface coverage on the order of a few monolayers of collagen.

3.3.4 Expression of DDR2

Of the three cell lines cell lines that were created to produce the ECD of DDR2, only one cell line, ECD-DDR2-His, gave appreciable expression of the excreted, soluble receptor, which was purified from the cell media using Ni-NTA chromatography. SDS-PAGE with silver staining and western blotting analysis of the purified DDR2 revealed that it was expressed as a monomer, dimer, and aggregate mixture as shown in figure 3.4 (a) and (b). Previous reports have indicated that the ECD of DDR2 was expressed as a monomer or dimer, but none of these studies reported seeing a mixture of different species. To the contrary, several studies reported that oligomerization of the receptor required the use of C-terminal fusion proteins that were used along with covalent cross-linking agents to permanently bind the monomers or dimers together.[117, 123, 126] As addition of a large excess of reducing reagent resulted in removal of higher molecular weight species (see Figure 3.4 (c)), it was concluded that a covalent dimer was formed, which was supported by the fact that the amino acid sequence of the ECD of DDR2 contains an odd number (7) of cysteines. Size exclusion chromatography with in-line multi-angle light scattering (SEC-MALS) and refractive index detectors confirmed the presence of 3 molecular species at 60 kDa (monomer), 120 kDa (dimer), and ~1000 kDa (aggregate containing approximately 15-17 monomers) with the monomer as the prevalent molecular species. Interestingly, SEC-MALS experiments that were repeated with 5 mM DTT in the running buffer did not result in removal of the higher molecular weight species, nor was a significant shift in the relative concentrations of the molecular species observed. Representative SEC-MALS chromatograms are shown in Figure 3.5.

As the initial SEC-MALS data resulted in near base-line separation of the three ECD-DDR2 species, attempts were made to separate the monomer from the dimer using FPLC with size exclusion chromatography. However, base-line resolution of the monomer and dimer peaks could not be achieved using the same buffer conditions with either a Superdex™ 200 column or a Superose™ 12 column. Addition of 5 mM DTT did not improve resolution, which was consistent with previous observations, but it did result in a small reduction in the dimer and aggregate peaks (Figure 3.6). Additionally, separated fractions stored at 4°C reverted to the original monomer, dimer, aggregate mixture even when stored under mild reducing conditions. Figure 3.7 shows a gel, which was run three days after separation, of FPLC fractions stored in reducing buffer and run in loading buffer without β-mercaptoethanol. Consequently, separation of the monomer and dimer has not yet been achieved.

3.3.5 TIRF Microscopy

Control slides consisting of aligned collagen films immobilized on EDS treated fused-silica slides attached to microscope slides were blocked with 10 mg/mL ovalbumin in PBS to prevent any areas that may not have been fully saturated with collagen from non-specifically adsorbing fluorescently-labeled proteins. To evaluate their applicability in TIRF measurements, a solution of 1 μM Fab labeled with Alexa Fluor® 514 with 10 mg/mL ovalbumin in PBS (Fab-A514) was added to each sample, and the slides were mounted on the stage of a TIRF microscope. Upon excitation at 514 nm, evanescently excited fluorescence with the characteristic oval shape seen in through-prism TIRF was observed. The spot appeared more diffuse than what is typically observed with other

samples, such as fluorescently-labeled phospholipid bilayers, but was sufficient for TIRF measurements.

To assess the sample to sample reproducibility required for the determination of binding constants with TIRF microscopy, three sets of two slides were prepared using the method described above with 1 μM ECD-DDR2 labeled with Alexa Fluor® 514 in 10 mg/mL ovalbumin in PBS used in place of the Fab-A514 solution. Using TIRF, fluorescent intensities were collected for nine different areas on each sample and were used to calculate a percent standard deviation (% SD) of the average for each slide. For each sample set, the percent difference in the average fluorescent intensity of the two slides was also determined, and the results are summarized in Table 3.1. The % SD for each slide was found to be less than 8%, indicating low variability in ECD-DDR2 surface binding across a given sample. As significant changes in the surface density of receptor binding sites across a sample would increase the % SD, the low % SD observed also indicates that the density of collagen on the surface of each slide is fairly uniform. The percent difference between the average fluorescence intensities of "duplicate" slides made with the same materials on the same day can be used to evaluate the inter-sample reproducibility. As the largest variability in TIRF measurements arises between duplicate samples, the observed percent differences, which ranged between 2.6% and 22.6%, were acceptable. Under ideal conditions that would yield binding constants with very low error, the percent difference between duplicate slides would approach zero.

Table 3.1 Evaluation of Sample Reproducibility

	Day 1		Day 2		Day 3	
Sample	A	B	A	B	A	B
% SD	1.7	9.5	7.3	5.4	4.7	7.4
% Difference	2.6		22.6		11.5	

As the fluorescence signal increases linearly with increasing solution concentration of fluorescent molecules in TIRF, negative controls in which fluorescent molecules in solution do not associate with the surface are required for binding experiments. To create negative controls for ECD-DDR2 binding experiments, this condition was simulated using the same collagen surfaces generated for positive control measurements, but Fab-A514 was used in place of ECD-DDR2-A514. As TIRF measurements are dependent on the relative fluorescence intensity, a correction factor based on the differences in the labeling ratios of the protein samples must be determined and applied to negative controls. To circumvent this problem, the fused-silica surfaces were coated with gelatin or BSA, proteins to which ECD-DDR2 does not bind, and TIRF measurements were taken using the Fab-A514 solution.

The normalized average fluorescence intensities for the three systems are presented in Table 3.2. As data were collected using the same concentration of a given sample of Fab-A514 and with the same excitation intensity, it is surprising that the average fluorescence intensities for gelatin and BSA coated fused-silica slides were much less than that of the collagen slides. These differences could result from many factors, such as Fab-A514 non-specifically binding to the sample or collagen coated slides exhibiting different evanescent wave profiles, and indicate that developing negative

controls will require more investigation. At present, even with the need to correct for differences in the labeling ratio, replacing ECD-DDR2 with Fab appears to be the best method for generating negative controls of the methods tested. However, a promising option would be to prevent DDR2 binding to immobilized collagen films by adding a large excess of a molecular species that binds in the ligand pocket of DDR2 with a very high affinity, such as triple-helical peptide analogs that contain the collagen recognition sequences required for DDR2 binding,[120] or that binds to DDR2 in a manner that blocks its binding pocket. Alternatively, DDR2 binding sites on collagen could be blocked by adding a large excess of a molecular species that binds to collagen at or overlapping the DDR2 recognition sites. Solid phase binding studies have also used collagen type IV, since DDR2 does not bind to this type of collagen, in place of collagen type I as a negative control.

Table 3.2 Negative Controls

	Surface Coating		
	Collagen	Gelatin	BSA
Normalized Fluorescence	1.0	0.3	0.2
Standard Deviation	0.1	0.06	0.02

3.4 Discussion

While conducting this work, many reports characterizing the interaction of the DDRs with collagen have been presented in the literature. Original binding studies of DDRs with collagen indicated that the DDR2 is activated by soluble and fibrillar collagens,[112, 113] but these studies failed to closely monitor the organization state of

collagen. However, more current investigations have focused on characterizing the binding of DDR2 to type I collagen monomers (MC). Using AFM, studies have shown that ECD-DDR2 binds to MC with 95% of the binding events occurring between a single ECD-DDR2 dimer and collagen. From this binding data, it was speculated that there may be two preferred binding sites on collagen, but the exact location of these sites could not be determined due to the fact that the collagen monomers were partially cleaved through pepsin digestion.[126] Furthermore, a study in which a peptide library was used to map the surface binding sites on collagen II for DDR2 saw that these triple-helical peptide analogs are capable of activating DDR2 with the same slow rate of phosphorylation characteristically observed with collagen. These peptides do not associate in solution to form supramolecular structures, suggesting that monomeric collagen is sufficient for receptor activation.[120] Investigations with soluble ECD-DDR2 proteins[123] and with over expression of surface anchored DDR2 receptors that lack that the kinase domain[127] have shown that DDR2 is capable of inhibiting fibrillogenesis of type I collagen in solution and in cell culture based assays. Collagen fibrils formed in the presence of DDR2 lacked native D-periodicity and had reduced radii as compared to fibrils formed in control measurements.[123, 127] As similar results were seen for DDR1,[122] these studies indicate that DDRs plays a significant role *in vivo* in the direct regulation of fibrillogenesis through collagen binding.

Other studies have characterized the interactions of cells expressing DDR2 with collagen type I in its fibrillar state (FC). When grown in contact with FC, proliferation of tumor cells is inhibited, which can be relieved through silencing of DDR2 expression, and an increase in DDR2 tyrosine phosphorylation was observed. Conversely, tumor

cells grown on films of monomeric type I collagen did not show increased activation of DDR2 and exhibited normal growth. This indicates that DDR2 participates in mediating tumor cell cycle arrest through direct receptor-induced signaling.[128] Contrary to findings for tumor cells, non-malignant cells, such as skin fibroblasts and hepatic stellate cells, when grown on FC and Matrigel, a commercial heterogeneous mix of collagens that forms fibrillar structures after incubation at biological temperature, have exhibited increased cell proliferation through DDR2 activation.[129, 130] Consequently when activated by FC, DDR2 may play a duel role as a growth inhibitor or stimulator depending on the cell type, but currently the mechanisms by which these processes occur are not well understood.

While many studies have indicated that the molecular organization of collagen is important for DDR2 recognition *in vivo*, a side-by-side, quantitative comparison of DDR2 binding to collagen in its MC versus FC forms has not been conducted to date. The *in vitro* binding of soluble ECD-DDR2 proteins has been widely studied in the literature with variable results, but these studies have been mostly been focused on the oligomerization state of DDR2 necessary for binding. Initial studies that used solid phase binding assays indicated that ECD-DDR2 binding of collagen type I and II only occurred for dimerized forms of ECD-DDR2 with half-maximal binding occurring at concentrations of approximately 20 nM ECD-DDR2.[117, 121] These studies also showed that the DS domain alone was sufficient for collagen binding when dimerized.[117] Other studies, again using solid phase binding assays[126] or surface plasmon resonance spectroscopy,[123] indicated that ECD-DDR2 clustering or oligomerization was necessary to see measurable binding and, for clusters of DDR2 containing 4 ECD units, found a

dissociation constant (K_d) of 0.3 nM for collagen type I.[123] Eventually, a monomeric DDR2 that consisted of only the DS domain was found to bind collagen type II with a K_d of 25 μM.[119] While these studies have taken great care to classify the oligomerization state of ECD-DDR2, the dependence of ECD-DDR2 binding strength on the organizational state of collagen has largely been ignored. This, along with the fact that the collagens were isolated from varying sources and were extracted using differing protocols, may account for the large discrepancy in the reported measurements. As such, the goal of this study was to use total internal reflection fluorescence microscopy (TIRF) to measure the binding of fluorescently-labeled ECD-DDR2 in solution to films of collagen type I fibrils or monomers that are immobilized at the solid-solution interface.

Through the work described in this chapter, considerable progress towards using TIRF to study the interactions of ECD-DDR2 with collagens has been made. Accurately measuring equilibrium binding constants with TIRF microscopy requires the use of samples with a consistent density of surface binding sites at the solid-solution interface. For ECD-DDR2 binding studies, this required the development of reproducible methods to coat fused-silica slides with collagen type I films, which was successfully accomplished for aligned, fibrillar and monomeric collagen films, as confirmed by fluorescence imaging, TIRF microscopy, and/or AFM. Light microscopy and fluorescence imaging showed partial alignment of unaligned collagen films, therefore; a better procedure for creating these films needs to be developed. The use of negative controls that account for background fluorescence, which increases linearly with the solution concentration of fluorescently-labeled molecules, is also required for accurate measurement of binding constants with TIRF microscopy. An acceptable method for

making negative controls, which involves replacing ECD-DDR2-A514 with Fab-A514, was also explored. Consequently, TIRF experiments for the binding of ECD-DDR2 to films of aligned, fibrillar or monomeric collagen type I are close to realization.

Attempts to separate the naturally occurring mixture of ECD-DDR2 monomer, dimer, and aggregate were unsuccessful. Recent evidence from the literature indicates that *in vivo* the DDRs exists as dimers and monomers in the plasma membrane of cells. However, upon collagen stimulation, the fraction of dimerized receptors does not increase, and only dimeric receptors exhibit phosphorylation, suggesting that monomeric receptors do not participate in the processes leading to signal transduction.[116, 131, 132] As a 1000-fold difference in the binding strength for collagen type II has been observed between dimeric[121] and monomeric states of ECD-DDR2,[119] separation of the two may not be required to determine dimer binding constants, because in TIRF the signal that arises from surface associated binding is dominated by the molecular species with the strongest equilibrium association constant. As the binding from aggregates, which occur *in vivo* only after activation,[116] has been shown to be approximately 100 fold stronger[123] than for dimers of ECD-DDR2,[117] separation of these two species may be necessary. Due to the large size difference, this separation could most likely be accomplished with filtering or clarification using ultra-centrifugation. Additionally, the occurrence of the molecular aggregate increased with concentrating (data not shown), therefore at low protein concentrations the aggregate may not be present to a significant percentage in ECD-DDR2 samples. Additionally, if future evidence implicates DDR2 monomers in significant biological roles, monomeric ECD-DDR2 could be generated through genetic cloning by removal of the stalk region, as DDR2 proteins containing only the DS domain

have been shown to retain collagen binding[117, 119] and as dimerization has been shown to occur through the ECD stalk region in DDR1,[132] which is homologous to the stalk region of DDR2. Currently, dimerization is not believed to induce a conformational change that increases binding affinity in the DS domain,[120] therefore; it may also be desirable to produce monomer only solutions of ECD-DDR2 to altogether avoid the need for separation of the oligomerization states. Since a mutation in DDR1 similar to the one made in the *m*ECD-DDR2-His plasmid was shown to abolish receptor dimerization,[132] work to increase the protein expression in this cell line could achieve this goal.

Overall, many new avenues exist for studying the interactions of ECD-DDR2 with collagen using TIRF microscopy. Pure collagen type I was initially selected for these studies because it is the most abundant collagen found in mammals and has widely been studied in the literature. However, even in tissues that are predominately collagen type I other types of collagen are found, notably types III and V. For example, in the case of the cornea, coassembly of collagen type V into collagen type I fibrils are believed to be one of the factors that regulate the small, uniform fibrillar diameters observed in this tissue.[90] Additionally, in developmental processes where DDRs are believed to play a key role in regulation of the ECM, multiple types of collagen exist and undergo changes in density, for example as seen in heart valve development.[115, 133] Therefore, classifying the interactions of DDR2 with other types of collagens or with mixtures of collagens is a direction that, as of yet, largely remains unexplored. As the binding of DDRs has been found to be dependent on the level of glycosylation in collagen,[112, 128] this represent another area for future study. Furthermore, there are no studies on the *in vitro* kinetic rates for the interaction of the DDRs with collagen, which could potentially be studied

with TIRF through combination with fluorescence recovery after photobleaching or fluorescence correlation spectroscopy.

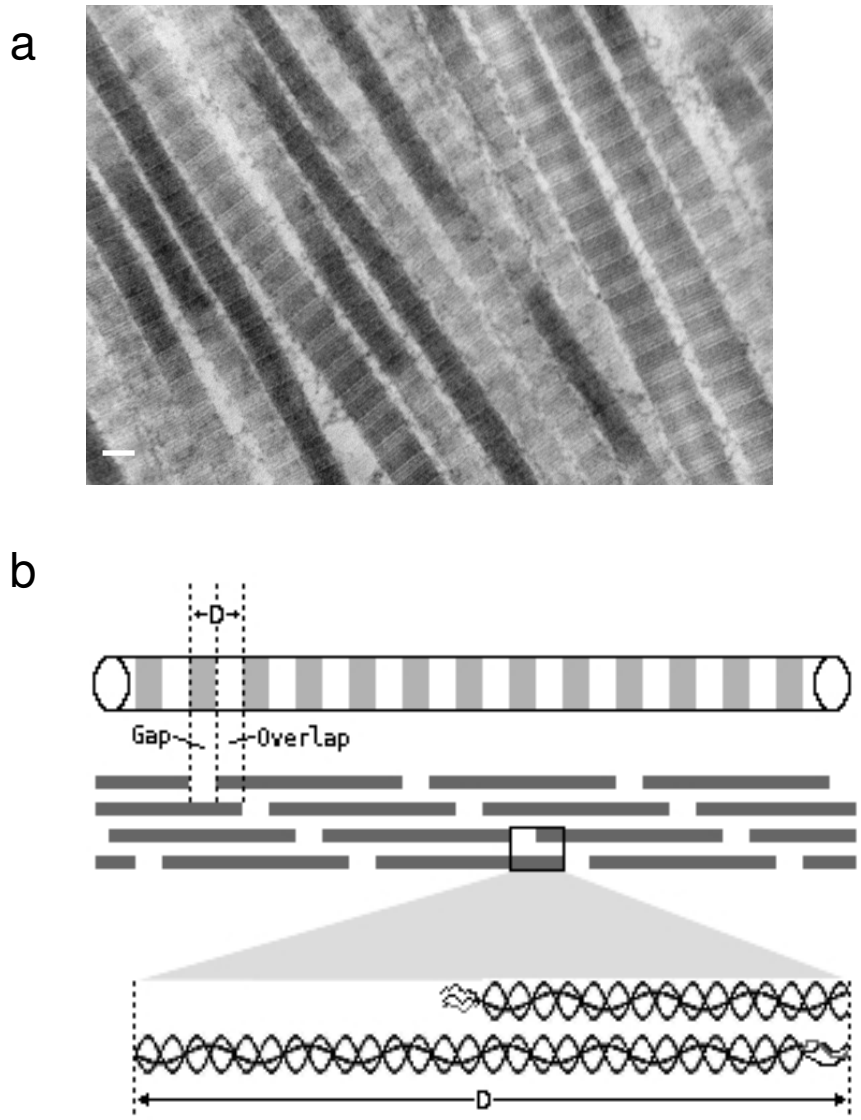

Figure 3.1 Structure of collagen fibrils. (a) TEM image of collagen type I fibrils isolated from mammalian lung tissue. The bar in the left hand corner represents 50 nm. (b) Cartoon rendering of a collagen fibril showing the characteristic, alternating light/dark pattern resulting from gap (dark) and overlap (light) regions of the fibril *(top)*. Each dark box represents a collagen molecule, aligned N to C from left to right, arranged in the staggered, parallel array conformation found in fibrils with D-periodicity *(middle)*. A zoomed in image of the D period shows the 234 amino-acid overlap between adjacent, triple-helical collagen molecules (bottom). [Figure (a) was released to the public domain by Louisa Howard (2006); http://remf.dartmouth.edu/images/mammalianLungTEM/source/9.html]

Figure 3.2 NMR Structure of the Discoidin Domain of DDR2 (side view) shows the jellyroll topology formed by the β-sheets (orange). The collagen binding site (not labeled) is located on top of the structure. (From ref 35; RCSB PDB ID: 2z4f)

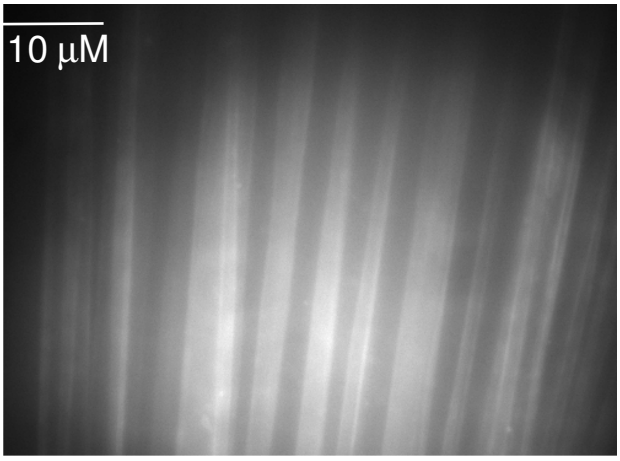

Figure 3.3 Epifluorescent Image of Aligned Collagen Fibrils. A 1.0 mg/mL solution of collagen type I with 1% FITC labeling was absorbed onto an EDS treated fused-silica coverslip, attached to a microscope slide, and washed with PBS. The image was collected with a CCD camera at 40x magnification on an inverted microscope with epifluorescence using an excitation wavelength of 488 nm.

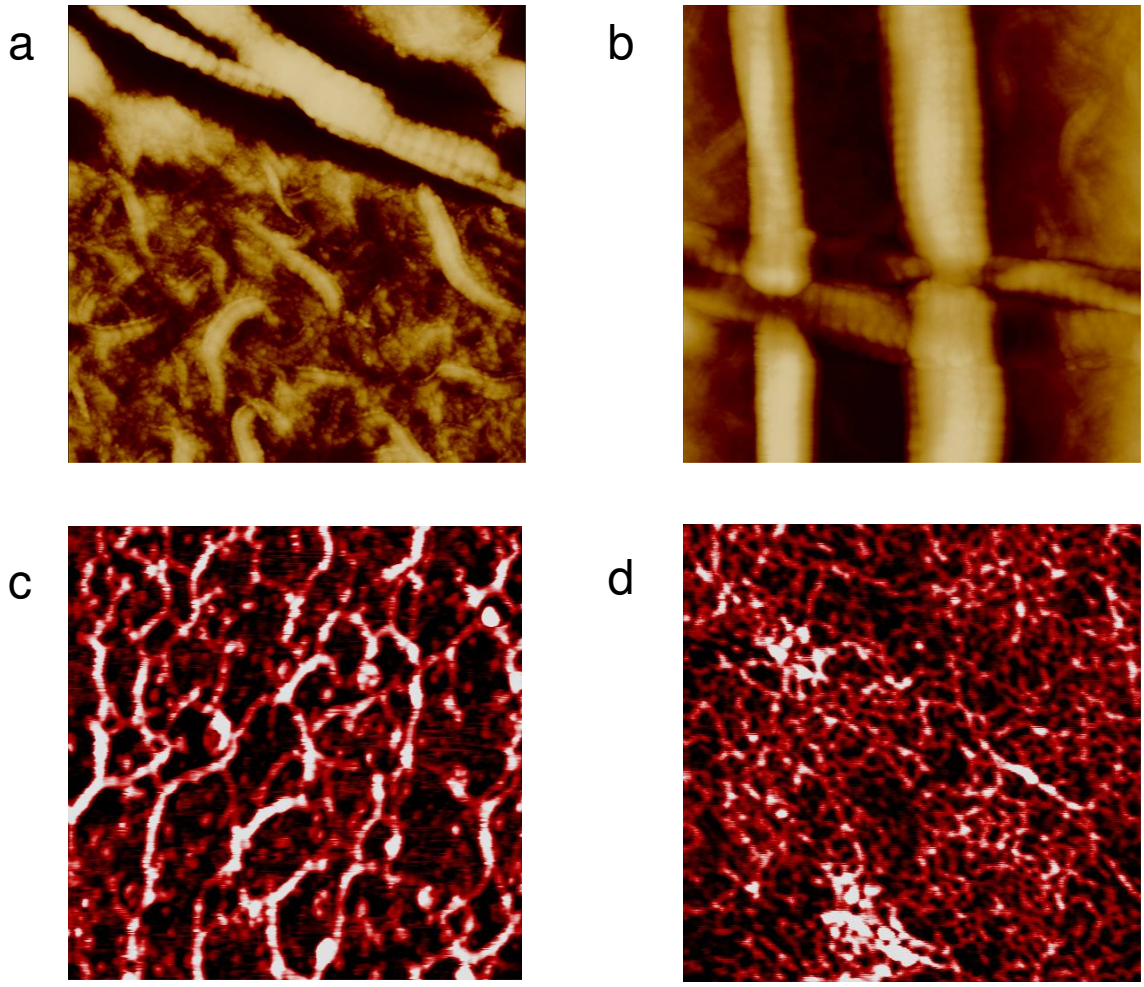

Figure 3.4 AFM Images of Collagen Films. EDS treated glass surfaces after non-specific adsorption of a 0.25 mg/mL solution of collagen neutralized in PBS results in (a) small fibrils (4 μm^2, 15 nm height scale) and (b) micron sized fibrils with clear D-periodicity (4 μm^2, 70 nm height scale). Adsorption of acidic collagen results in short, filamentous morphology of collagen molecules on (c) siliconized glass (1 μm^2, 10 nm height scale) and (d) bare glass (1 μm^2, 3 nm height scale). All images were taken in air.

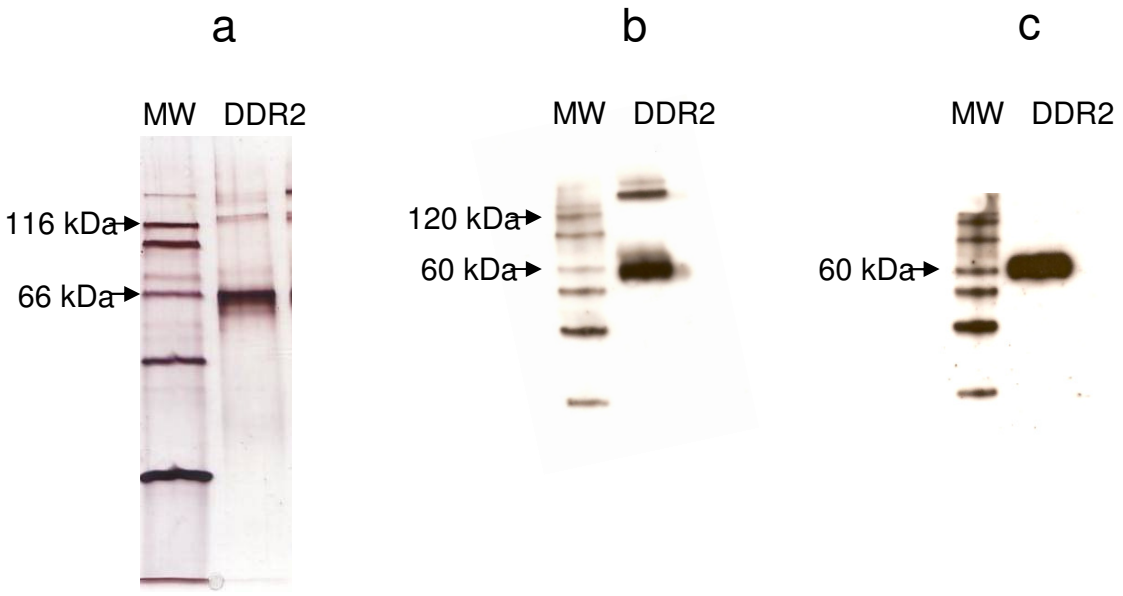

Figure 3.5 SDS-PAGE and Western Blotting of ECD-DDR2. (a) SDS-Page with silver staining of a 10% Tris-HCl gel showed multiple bands for the purified ECD-DDR2 samples under non-reducing conditions. (b) Western blot analysis under non-reducing conditions with anti-ECD-DDR2 primary antibodies indicated that ECD-DDR2 oligomerizes. (c) Western blot analysis probed with anti-ECD-DDR2 primary antibodies of the same sample as in (b) but under reducing conditions showed loss of high MW products and provides evidence for covalent interactions.

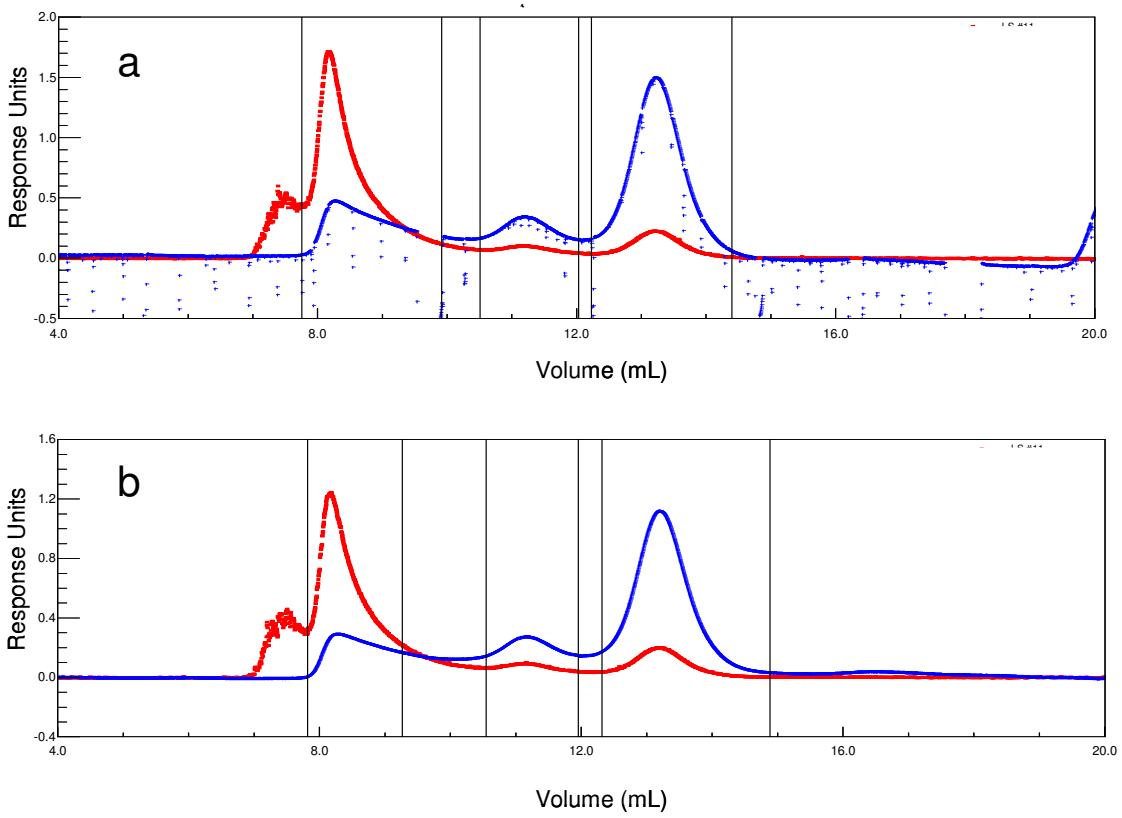

Figure 3.6 SEC-MALS of ECD-DDR2. FPLC chromatograms with multi-angle light scattering (–) and refractive index (–) detection of ECD-DDR2 samples run in PBS (a) or in PBS with 5 mM DTT (b). The black lines indicate the widths used to calculate peak area for MW determination. From left areas the boxed peaks correspond to the molecular aggregate, dimer, and monomer.

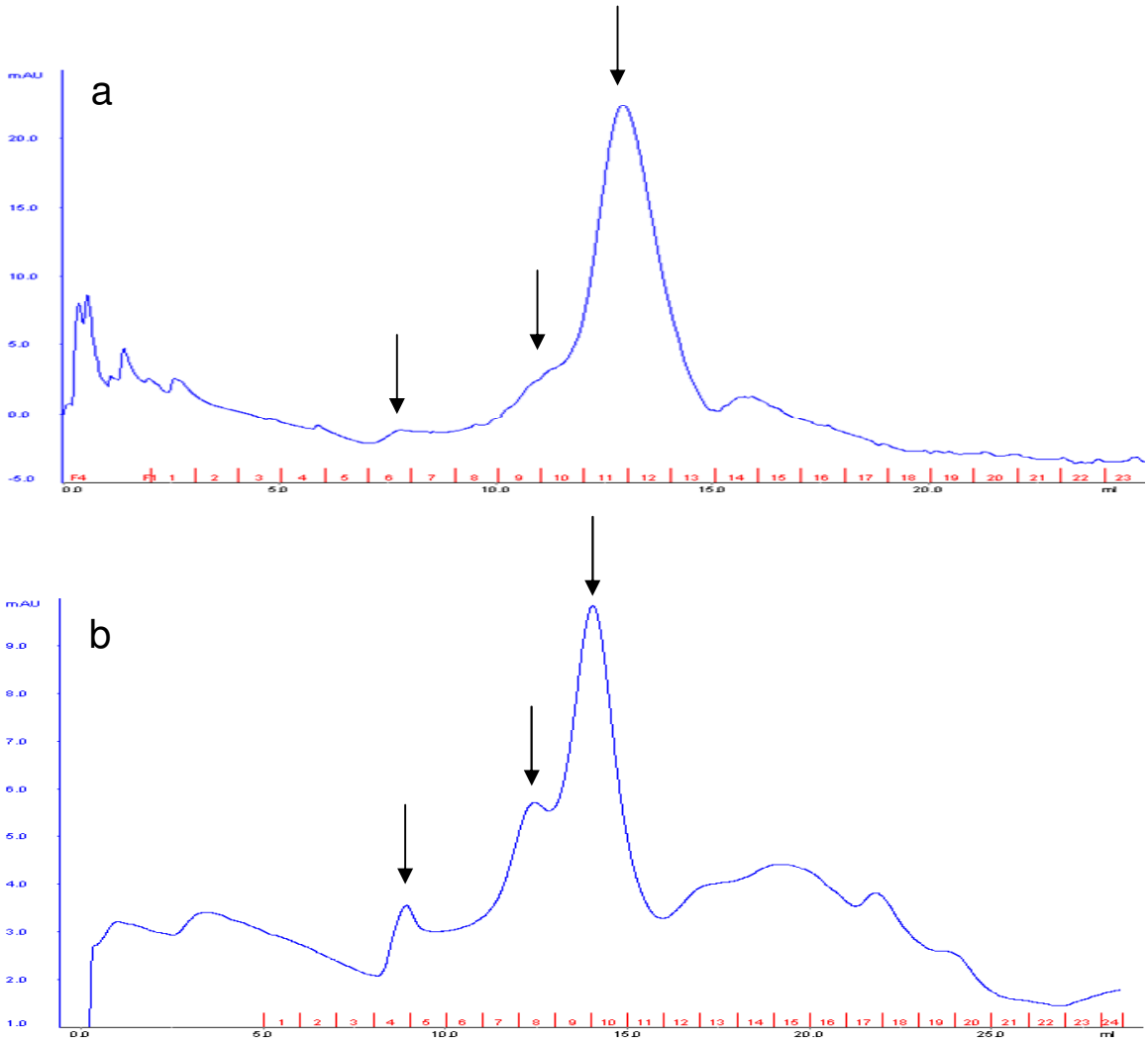

Figure 3.7 FPLC Chromatograms of ECD-DDR2 Samples. FPLC chromatograms with UV detection of 1.0 mg/mL ECD-DDR2 samples run at a flow rate of 0.5 mg/mL in PBS with 5 mM DTT (a) and in PBS (b) on a Superdex™ 200 column. From left to right, the three arrows in each chromatogram indicate aggregate, dimer and monomer peaks. A slight reduction in the peak areas of the aggregate and dimer can be observed in (a) as compared to (b).

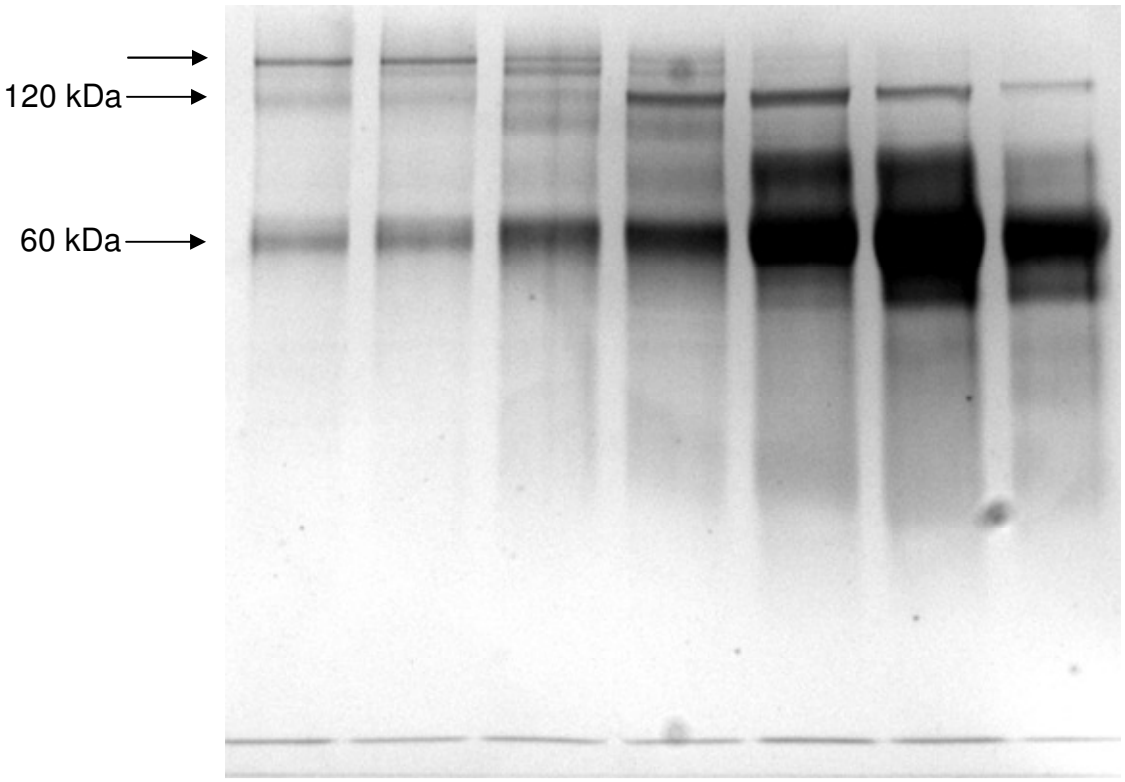

Figure 3.8 SDS-PAGE of FPLC Fractions. SDS-PAGE on a 10% Tris-HCl gel with silver staining of successive FPLC fractions collected in PBS with 5 mM DTT diluted 1:1 with non-reducing 2x SDS-Loading Buffer revealed that monomeric and dimeric forms of ECD-DDR2 were present in all samples 3 days after separation. The top arrow indicates DDR2 molecular aggregate, which was detected in only the first four fractions analyzed.

3.5 References

1. Suh, H., Collagen Fabrication for the Cell-based Implants in Regenerative Medicine. In *Bioengineering in Cell and Tissue Research*, Artmann, G.; Chien, S., Eds. Springer: 2008; pp 159-192.

2. Myllyharju, J.; Kivirikko, K., Collagens, modifying enzymes and their mutations in humans, flies, and worms. *Trends. Genet.* **2004,** *20*, 33-43.

3. Leitinger, B.; Hohenester, E., Mammalian collagen receptors. *Matrix Biology* **2007,** *26*, 146-155.

4. Hulmes, D., Collagen Diversity, Synthesis, and Assembly. In *Collagen: Structure and Mechanics*, Fratzl, P., Ed. Springer US: 2008; pp 15-47.

5. Wess, T., Collagen Fibrillar Structue and Hierarchies. In *Collagen: Structure and Mechanics*, Fratzl, P., Ed. Springer US: 2008; pp 49-80.

6. Rivier, N.; Sadoc, J., The Structure of Collagen. In *Topology in Molecular Biology*, Monastyrsky, M., Ed. Springer Berlin Heidelberg: 2007; pp 147-162.

7. Holmes, D.; Kadler, K., Collagen fibril assembly *in vitro*. In *Cell Biology Protocols*, Harris, J. R.; Graham, J.; Rickwood, D., Eds. John Wiley and Sons, Ltd.: Chinchester, 2006; pp 375-378.

8. Leikin, S.; Rau, D.; Parsegain, V., Temperature-favoured assembly of collagen is driven by hydrophilic not hydrophobic interactions. *Nat. Struct. Biol.* **1995,** *2*, 205-210.

9. Raspanit, M.; Viola, M.; Sonaggere, M.; Tira, M. E.; Tenni, R., Collagen Fibril Structure is Affected by Collagen Concentration and Decorin. *Biomacromolecules* **2007,** *8*, 2087-2091.

10. Harris, J. R.; Reiber, A., Influence of saline and pH on collagen type I fibrillogenesis in vitro: Fibrit polymorphism and colloidal gold labelling. *Micron* **2007,** *38* (5), 513-521.

11. Li, Y.; Asadi, A.; Monroe, M. R.; Douglas, E. P., pH effects on collagen fibrillogenesis in vitro: Electrostatic interactions and phosphate binding. *Materials Science and Engineering C* **2009,** *29*, 1643-1649.

12. Williams, B.; Gelman, R.; Poppke, D.; Piez, K., Collagen fibril formation: optimal in vitro conditions and preliminary kinetic results. *Journal of Biological Chemistry* **1978,** *235*, 6578-6585.

13. Hayashi, T.; Nagai, Y., Factors affecting the interactions of collagen molecules as observed by in vitro fibril formation. II. Effects of species and concentration of anions. *Biochemistry (Tokyo)* **1973,** *74*, 253-262.

14. Kadler, K.; Holmes, D.; Trotter, J.; Chapman, J., Collagen fibril formation. *Biochem. J.* **1996,** *316*, 1-11.

15. Khoshnoodi, J.; Cartailler, J.-P.; Alvares, K.; Veis, A.; Hudson, B. G., Molecular Recognition in the Assembly of Collagens: Terminal Noncollagenous Domains Are Key Recognition Modules in the Formation of Triple Helical Protomers. *The Journal of Biological Chemistry* **2006,** *281* (50), 38117-38121.

16. Holmes, D.; Graham, H.; Trotter, J.; Kadler, K., STEM/TEM studies of collagen fibril assembley. *Micron* **2001,** *32*, 273-285.

17. Franchi, M.; Trire, A.; Quaranta, M.; Orsini, E.; Ottani, V., Collagen structure of tendon relates to function. *Thescientificworldjournal* **2007,** *7*, 404-420.

18. Matsumoto, N.; Horibe, S.; Nakamura, N.; Senda, T.; Shino, K.; Ochi, T., Effect of alignment of the transplanted graft extracellular matrix on cellular repopulation and newly synthesized collagen. *Archives of Orthopaedic and Trauma Surgery* **1998,** *117* (4-5), 215-221.

19. Dickinson, R.; Guido, S.; Tranquillo, R., Biased cell-migration of fibroblasts exhibiting contact guidance in oriented collagen gels. *Ann Biomed Eng* **1994,** *22* (342-356).

20. Torbet, J.; Ronziere, M., Magnetic Alignment of collagen during self-assembly of collagen during self-assembly. *Biochem. J.* **1984,** *219*, 1057-1059.

21. Mosser, G.; Anglo, A.; Helary, C.; Bouligand, Y.; Giraud-Guille, M., Dense tissue-like collagen matrices formed in cell-free conditions. *Matrix Biology* **2006,** *25*, 3-13.

22. Ng, C.; Swartz, M., Mechanisms of interstitial flow-induced remodeling of fibroblast-collagen cultures. *Ann Biomed Eng* **2006,** *34*, 446-454.

23. Guo, C.; Kaufman, L., Flow and Magnetic field induced collagen alignment. *Biomaterials* **2006,** *28*, 1105-1114.

24. Lee, P.; Lin, R.; Moon, J.; Lee, L., Microfludic alignment of collagen fibers for *in vitro* cell culture. *Biomed Microdevices* **2006,** *8*, 35-41.

25. Heino, J.; Huhtala, M.; Käpylä, J.; Johnson, M. S., Evolution of collagen-based adhesion systems. *The International Journal of Biochemistry & Cell Biology* **2009,** *41*, 341-348.

26. Ulrich, A.; Schlessinger, J., Signal Transduction by Receptors with Tyrosine Kinase Activity. *Cell* **1990,** *61*, 203-212.

27. Vogel, W. F.; Gish, G.; Alves, F.; Pawson, T., The discoidin domain receptor tyrosine kinases are activated by collagen. *Molecular Cell* **1997,** *1*, 13-23.

28. Shrivastava, A.; Radziejewski, C.; Campbell, E.; Kovac, L.; McGlynn, M.; Ryan, T.; Davis, S.; Goldfarb, M.; Glass, D.; Lemke, G.; Yancopoulos, G. D., An orphan receptor tyrosine kinase family whose members serve as nonintegrin collagen receptors. *Molecular Cell* **1997,** *1*, 25-34.

29. Vogel, W. F.; Abdulhussein, R.; Ford, C. E., Sensing extracellular matrix: an update on discoidin domain receptor function. *Cellular Signalling* **2006,** *18*, 1108-1116.

30. Leitinger, B.; Kwan, A. P. L., The discoidin domain receptor DDR2 is a receptor for type X collagen. *Matrix Biology* **2006,** *25* (6), 355-364.

31. Morales, M. O.; Price, R. L.; Goldsmith, E. C., Expression of discoidin domain receptor 2 (DDR2) in the developing heart. *Microscopy and Microanalysis* **2005,** *11* (3), 260-267.

32. Mihai, C.; Chotani, M.; Elton, T. S.; Agarwal, G., Mapping of DDR1 Distribution and Oligomerization on the Cell Surface by FRET Microscopy. *Journal of Molecular Biology* **2009,** *385* (2), 432-445.

33. Leitinger, B., Molecular Analysis of Collagen Binding by the Human Discoidin Domain Receptors, DDR1 and DDR2. *Journal of Biological Chemistry* **2003,** *278* (19), 16761-16769.

34. Abdulhussein, R.; McFadden, C.; Fuentes-Prior, P.; Vogel, W. F., Exploring the collagen-binding site of the DDR1 Tyrosine kinase receptor. *The Journal of Biological Chemistry* **2004,** *279*, 31462-31470.

35. Ichikawa, O.; Osawa, M.; Nishida, N.; Goshima, N.; Nomura, N.; Shimada, I., Structural basis of the collagen-binding mode of discoidin domain receptor 2. *Embo Journal* **2007,** *26* (18), 4168-4176.

36. Konitsiotis, A. D.; Raynal, N.; Bihan, D.; Hohenester, E.; Farndale, R. W.; Leitinger, B., Characterization of High Affinity Binding Motifs for the Discoidin Domain Receptor DDR2 in Collagen. *Journal of Biological Chemistry* **2008,** *283* (11), 6861–6868.

37. Leitinger, B.; Steplewski, A.; Fertala, A., The D2 period of collagen II contains a specific binding site for the human discoidin domain receptor, DDR2. *Journal of Molecular Biology* **2004,** *344* (4), 993-1003.

38. Agarwal, G.; Mihai, C.; Iscru, D. F., Interaction of discoidin domain receptor 1 with collagen type 1. *Journal of Molecular Biology* **2007,** *367* (2), 443-455.

39. Mihai, C.; Iscru, D. F.; Druhan, L. J.; Elton, T. S.; Agarwal, G., Discoidin domain receptor 2 inhibits fibrillogenesis of collagen type 1. *Journal of Molecular Biology* **2006,** *361* (5), 864-876.

40. Lom, B.; Healy, K.; Hockberger, P., A versatile technique for patterning biomolecules onto glass coverslips. *Journal of Neuroscience Methods* **1993,** *50*, 385-397.

41. Bhatia, S. N.; Yarmush, M. L.; Toner, M., Controlling cell interactions by micropatterning in co-cultures: Hepatocytes and 3T3 fibroblasts. *Journal of Biomedical Materials Research* **1997,** *34* 189-199.

42. Agarwal, G.; Kovac, L.; Radziejewski, C.; Samuelsson, S. J., Binding of discoidin domain receptor 2 to collagen I: An atomic force microscopy investigation. *Biochemistry* **2002,** *41* (37), 11091-11098.

43. Blissett, A. R.; Garbellini, D.; Calomeni, E. P.; Mihai, C.; Elton, T. S.; Agarwal, G., Regulation of Collagen Fibrillogenesis by Cell-surface Expression of Kinase Dead DDR2. *Journal of Molecular Biology* **2009,** *385* (3), 902-911.

44. Wall, S. J.; Werner, E.; Werb, Z.; DeClerck, Y. A., Discoidin domain receptor 2 mediates tumor cell cycle arrest induced by fibrillar collagen. *Journal of Biological Chemistry* **2005,** *280* (48), 40187-40194.

45. Olaso, E.; Labrador, J. P.; Wang, L. H.; Ikeda, K.; Eng, F. J.; Klein, R.; Lovett, D. H.; Lin, H. C.; Friedman, S. L., Discoidin domain receptor 2 regulates fibroblast proliferation and migration through the extracellular matrix in association with transcriptional activation of matrix metalloproteinase-2. *Journal of Biological Chemistry* **2002,** *277* (5), 3606-3613.

46. Olaso, E.; Ikeda, K.; Eng, F. J.; Xu, L.; Wang, L.-H.; Lin, H. C.; Friedman, S. L., DDR2 receptor promotes MMP-2–mediated proliferationand invasion by hepatic stellate cells. *The Journal of Clinical Investigation* **2001,** *108*, 1369-1378.

47. Noordeen, N. A.; Carafoli, F.; Hohenester, E.; Horton, M. A.; Leitinger, B., A transmembrane leucine zipper is required for activation of the dimeric receptor tyrosine kinase DDR1. *Journal of Biological Chemistry* **2006,** *281* (32), 22744-22751.

48. Abdulhussein, R.; Koo, D. H. H.; Vogel, W. F., Identification of disulfide-linked dimers of the receptor tyrosine kinase DDR1. *Journal of Biological Chemistry* **2008,** *283* (18), 12026-12033.

49. Goldsmith, E. C.; Hoffman, A.; Morales, M. O.; Potts, J. D.; Price, R. L.; McFadden, A.; Rice, M.; Borg, T. K., Organization of fibroblasts in the heart. *Developmental Dynamics* **2004,** *230* (4), 787-794.

Chapter 4

Quantifying GFP Diffusion in *Escherichia coli* by Using Continuous Photobleaching with Evanescent Illumination

4.1 Introduction

Translational diffusion is central to most biological processes especially in prokaryotic cells. Since these cells lack the motor proteins and developed cytoskeletal networks of higher organisms, diffusion is often their primary source of intracellular movement. Measuring diffusion in micron-sized structures, however, is challenging because of their small size compared to classical optical resolution.

The primary method for measuring diffusion in biological systems, fluorescence recovery after photobleaching (FRAP) with a small focused spot,[134, 135] suffers from the fact that the smallest focused laser spot used for illumination is not much smaller than an *Escherichia coli* cell or an organelle.[136] Thus, not only is optical alignment difficult, but also the quantity of unbleached molecules that can contribute to fluorescence recovery is limited. These effects reduce the signal-to-noise ratio and complicate data analysis. In addition, the recovery time associated with a small, focused spot and solute diffusion is too rapid for many conventional, simpler instruments. Despite these challenges, diffusion of green fluorescent protein (GFP) has been measured in *E. coli* with a combination of confocal microscopy and bleaching of a significant portion of the cell.[137-139]

Fluorescence correlation spectroscopy (FCS) is the other primary method for measuring translational diffusion in biological systems.[135, 140, 141] FCS suffers in the context of small, contained structures, since the size of the illuminated region is on the same order of magnitude as the structures. Consequently, there is only a small population of non-illuminated molecules. Under such conditions, the fluorescence fluctuations can be recorded for only a short time before the reservoir of unbleached molecules is depleted by photobleaching. This limitation significantly reduces the signal-to-noise ratio of the

fluorescence fluctuation autocorrelation function. Nonetheless, FCS has been successfully employed to measure protein diffusion coefficients in *E. coli* cells.[142] The method is limited, however, to low concentrations of fluorescent molecules.

Continuous fluorescence microphotolysis or continuous photobleaching (CP) is an alternate method for characterizing lateral diffusion in biological systems. In CP, a small region of a fluorescently labeled sample is continuously illuminated such that two competing processes arise—photobleaching of fluorophores in the illuminated region and fluorescence recovery due to diffusion of unbleached fluorophores from surrounding regions into the illuminated region. By monitoring the rate and shape of the fluorescence decay, rate constants for the two processes can be determined by fitting to appropriate theoretical forms.[143, 144] Recently, CP has been used, along with FCS, to measure diffusion and compartmentalization in giant unilamellar vesicles and in large living cells.[145] The results of CP, FCS, spatial imaging, and confocal microscopy have been used together to analyze diffusion of intracellular molecules and binding to specific sites in cells.[146] CP has also been combined with 4Pi microscopy to obtain higher spatial resolution.[147] Pulsed FRAP, a modification that combines CP and FRAP, has been used with confocal microscopy to measure the diffusion coefficients of fluorescent proteins in *E. coli.*[148]

Total internal reflection (TIR) has previously been combined with FRAP to measure solute diffusion in eukaryotic cells.[149] The small penetration depth of the evanescent wave results in photobleaching only near the interface. Since this depth is much smaller than the diameter of the laser beam, a one-dimensional geometry can be used to simplify the mathematical diffusion model. The small penetration depth,

however, also leads to fast recovery, thus requiring special equipment (e.g., acousto-optic modulators).

Here, we combine total internal reflection and continuous photobleaching to demonstrate a new method, TIR-CP, for characterizing the translational diffusion of fluorescent molecules contained in structures only slightly larger than classical optical resolution. These structures are deposited on a surface at which a laser beam is internally reflected, such that the resulting evanescent intensity illuminates only those fluorescent molecules close to the surface. The sample is continuously photobleached as a function of the excitation intensity. As in CP, two competing processes contribute to the rate and shape of fluorescence decay. At low intensities, the decay is determined by the photobleaching rate within the evanescent wave. At higher intensities, the decay is also affected by diffusion of the fluorescent molecules. Thus, the diffusion coefficient of the fluorescent molecules within the small structures can be determined by acquiring data as a function of the excitation intensity. This paper describes the theoretical basis for this new method and demonstrates its applicability by measuring the diffusion coefficient of GFP in *E. coli* cells.

4.2 Theory

4.2.1 Conceptual Basis

The notion behind the new method is illustrated in Fig. 1. Small structures of average length L are deposited on a surface at which a laser beam is internally reflected. The evanescent intensity decays with distance z from the surface and with a spatial profile in the x-y plane as

$$I(x,y,z) = I_0 \exp(-\frac{2x^2}{w_x^2}) \exp(-\frac{2y^2}{w_y^2}) \exp(-\frac{z}{d}) \quad (1)$$

where I_0 is the intensity at the interface (z = 0) and at the spot center (x = y = 0).[150] The characteristic distance for the evanescent wave decay, d, depends on the excitation wavelength, the incidence angle, and the refractive indices of the two materials at which internal reflection occurs. Parameters w_x and w_y are $1/e^2$ values for the elliptical Gaussian shape of the internally reflected beam in the sample plane and depend on the initial beam radius as well as the optical parameters used to generate internal reflection.

The observed sample volume is defined by the depth of the evanescent intensity and by a pinhole placed at a back image plane of an optical microscope through which the fluorescence is collected. The pinhole, which is positioned to correspond to the center of the illuminated region (x = y = 0), restricts fluorescence observation to a small volume so that the collected fluorescence is low enough to be measurable even at relatively high excitation intensities. For the same reason, fluorescence is collected though a low numerical aperture objective. The low numerical aperture does not compromise z-axis resolution, which is very thin as defined by the evanescent excitation intensity. The observed area is small enough so that only a few of the small structures are present in this area.

The sample's fluorescence is monitored as a function of time, t, with t = 0 corresponding to the onset of illumination. The time-dependent fluorescence decays to zero as molecules within the evanescent wave are photobleached and the reservoir of unbleached molecules within the small structure is depleted. Two competing processes,

diffusion and photobleaching, contribute to the rate and shape of fluorescence decay. At low intensities, the decay is determined by the photobleaching rate within the evanescent wave. At high enough intensities, the photobleaching rate is fast enough that the diffusion of unbleached molecules into the evanescent wave becomes the rate limiting step. By acquiring data as a function of the excitation intensity, the diffusion coefficient of the fluorescent molecules within the small structure is determined.

4.2.2 Concentration of Unbleached Molecules as a Function of Space and Time

The evanescently illuminated area is much larger than the observed area, and the pinhole is placed at the center of this illumination. Since the sample radius (~ 5 μm) is much less than w_x and w_y (22 and 65 μm respectively), the intensity at z = 0 does not vary much over the observed area in the x-y plane. The intensity at z = 0 also does not vary significantly as a function of x and y for a given cell because an *E. coli* cell is smaller than the observed area. Furthermore, the characteristic distance of the evanescent wave decay (d ~ 0.1 μm) is much less than the length of a cell in the z-direction (L ~ 2 μm). For these reasons, the mathematical problem is approximately one-dimensional in space with the key coordinate being z. The evanescent intensity (Eq. 1) is then approximated as

$$I(z) \approx I(0,0,z) = I_0 \exp(-\frac{z}{d}) \qquad (2)$$

and the concentration of unbleached molecules is assumed not to depend on coordinates x and y. As a result, an approximate differential equation for the concentration of

unbleached molecules is spatially one-dimensional and depends only on the distance from the interface, z, and the time, t. This equation is

$$\frac{\partial}{\partial t}U(z,t) = D\frac{\partial^2}{\partial z^2}U(z,t) \qquad (3)$$

where U(z,t) is the concentration of unbleached molecules as a function of space and time, and D is the diffusion coefficient. Unlike similar theories,[143, 144] Eq. 3 lacks a term describing photobleaching, because photobleaching occurs only at or near the illuminated surface. Instead, this process is described by a boundary condition (Eq. 6, see below).

The initial condition is

$$U(z,0) = C \qquad (4)$$

where C is the total concentration of fluorescent molecules. One boundary condition is

$$[\frac{\partial}{\partial z}U(z,t)]_{z=L} = 0 \qquad (5)$$

where L is the length of the cell measured from the surface into the solution. This "reflection" condition expresses the notion that the flux across the boundary of the structure far from the interface is zero. The other boundary condition is

$$D[\frac{\partial}{\partial z}U(z,t)]_{z=0} = d\kappa I_0 U(0,t) \qquad (6)$$

where κ is a proportionality constant describing the photobleaching propensity with units of intensity^{-1} time^{-1}.[151]

The general solution to Eq. 3 is

$$U(z,t) = [A\cos(\beta z) + B\sin(\beta z)]\exp(-D\beta^2 t) \qquad (7)$$

where A, B and β are constants. Eqs. 5-7 [i.e., the two boundary conditions and the general solution] imply that

$$\begin{aligned} A\sin(\beta L) &= B\cos(\beta L) \\ BD\beta &= d\kappa I_0 A \end{aligned} \qquad (8)$$

These two equations yield a discrete, countably infinite number of β and x values defined by

$$\begin{aligned} \beta_n \tan(\beta_n L) &= \frac{d\kappa I_0}{D} \qquad & x_n \tan(x_n) &= c \\ x_n &\equiv \beta_n L & c &\equiv \frac{d\kappa I_0 L}{D} \end{aligned} \qquad (9)$$

where x_n (for n = 1,2,3,…) and c are dimensionless quantities.

The values of x_1, x_2 and x_3 (determined numerically) are shown in Fig. 2a as a function of c, which is proportional to the excitation intensity, I_0 (Eqs. 9). The values of x_n have the following properties. First, $(n-1)\pi \leq x_n \leq (2n-1)\pi/2$. Second, x_n increases with c. At extremely low intensities, $c \approx 0$, $\tan(x_1) \approx 0$, and $x_1^2 \approx 0$. At higher intensities, $\tan(x_1) \approx x_1$ and $x_1^2 \approx c$. As shown in Fig. 3, this approximation is accurate within 10% up to $c \leq 0.3$. At even higher intensities,

$$\begin{aligned} \tan(x_1) &\approx x_1 + \frac{x_1^3}{3} \\ c &\approx x_1 \tan(x_1) \approx x_1^2 + \frac{x_1^4}{3} \\ x_1^2 &\approx \frac{-3 + (9 + 12c)^{1/2}}{2} \end{aligned} \tag{10}$$

As shown in Fig. 3, this approximation is accurate within 10% up to $c \leq 1.5$. At even higher intensities,

$$\begin{aligned} \tan(x_1) &\approx x_1 + \frac{x_1^3}{3} + \frac{2x_1^5}{15} \\ c &\approx x_1 \tan(x_1) \approx x_1^2 + \frac{x_1^4}{3} + \frac{2x_1^6}{15} \\ x_1^2 &\approx \frac{1}{6}\left\{ \begin{array}{l} -5 + \dfrac{(13)(5^{2/3})}{[-110 - 162c + 9(285 + 440c + 324c^2)^{1/2}]^{1/3}} \\ -(5^{1/3})[-110 - 162c + 9(285 + 440c + 324c^2)^{1/2}]^{1/3} \end{array} \right\} \end{aligned} \tag{11}$$

As shown in Fig. 3, this approximation is accurate within 10% up to $c \leq 2.9$. For extremely large intensities, $c \rightarrow \infty$ and $x_1 \rightarrow \pi/2$.

Eqs. 8 and 9 also imply that

$$A_n = \frac{x_n}{c} B_n \tag{12}$$

Thus (Eqs. 7 and 12),

$$U(z,t) = \sum_{n=1}^{\infty} B_n [\frac{x_n}{c} \cos(\frac{x_n z}{L}) + \sin(\frac{x_n z}{L})] \exp[-D(\frac{x_n}{L})^2 t] \tag{13}$$

At time zero (Eqs. 4 and 13),

$$C = \sum_{n=1}^{\infty} B_n [\frac{x_n}{c} \cos(\frac{x_n}{L} z) + \sin(\frac{x_n}{L} z)] \tag{14}$$

Multiplying both sides of Eq. 14 by the factor,

$$\frac{x_m}{c} \cos(\frac{x_m}{L} z) + \sin(\frac{x_m}{L} z) \tag{15}$$

and integrating z from zero to L (with Eq. 9) implies that

$$U(z,t) = \sum_{n=1}^{\infty} \frac{2c^2 C}{x_n (c + c^2 + x_n^{\ 2})} [\frac{x_n}{c} \cos(\frac{x_n z}{L}) + \sin(\frac{x_n z}{L})] \exp[-D(\frac{x_n}{L})^2 t] \tag{16}$$

It can be shown in a straightforward manner (with Eq. 9) that each term in Eq. 16 satisfies Eqs. 3, 5 and 6. The consistency of Eq. 16 with Eq. 4 can be demonstrated numerically.

4.2.3 Fluorescence Decay During Continuous Photobleaching

The observed fluorescence during continuous photobleaching at (x,y) = (0,0), is given by (Eqs. 2, 9 and 16)

$$F(t) = QI_0 \int_0^L dz \exp(-\frac{z}{d}) U(z,t) = \sum_{n=1}^{\infty} F_n \exp[-D(\frac{x_n}{L})^2 t]$$
$$F_n = 2QI_0 CcdL \frac{(cd+L)x_n^2 - \exp(-\frac{L}{d})[L(c^2 + x_n^2)\cos(x_n)]}{x_n^2 (c + c^2 + x_n^2)(L^2 + d^2 x_n^2)} \quad (17)$$

where Q is a proportionality constant. The initial fluorescence value is (Eqs. 4 and 17)

$$F(0) = QCI_0 d[1 - \exp(-\frac{L}{d})] \quad (18)$$

Thus,

$$f(t) \equiv \frac{F(t)}{F(0)} = \sum_{n=1}^{\infty} f_n \exp[-D(\frac{x_n}{L})^2 t]$$
$$f_n = \frac{2cL\left\{(cd+L)x_n^2 - \exp(-\frac{L}{d})[L(c^2 + x_n^2)\cos(x_n)]\right\}}{[1 - \exp(-\frac{L}{d})]x_n^2 (c + c^2 + x_n^2)(L^2 + d^2 x_n^2)} \quad (19)$$

For our experimental conditions, d ≈ 0.1 μm and L ≈ 2.2 μm (see below). Fig. 2b shows the values of f_1, f_2 and f_3 as function of c, for these values of d and L. As shown, f_1 drops below 0.9 only for c > 0.3. Thus, for c < 0.3, the fluorescence decay can be accurately approximated by a single exponential with rate $R_1 = D(x_1/L)^2$. For our experimental conditions, c ≤ 2 (see below). As shown in Fig. 2b, for 0.3 ≤ c ≤ 2, f_1 ranges from 0.9 to 0.6. Therefore, one might expect that multi-exponential analysis would be required for the higher intensities. For these intensities, however, the second rate, $R_2 = D(x_2/L)^2$, ranges from 5-18 sec^{-1} (see below), faster than the time resolution of our software (50 msec), and contributions to f(t) from terms with n > 1 are negligible. Therefore, we evaluate all data as a single exponential with rate, R, where

$$f(t) \approx \exp[-Rt]$$
$$R \approx D(\frac{x_1}{L})^2 \qquad (20)$$

4.2.4 Limits as a Function of Intensity Parameter c

When c is small (≈ 0), $x_1^2 \approx 0$ (Eq. 9), and Eq. 20 predicts the expected result that R ≈ 0 and f(t) ≈ 1 is constant with time. In other words, for very low intensities, photobleaching does not occur. When c is small but nonzero, $\tan(x_1) \approx x_1$, $x_1^2 \approx c$ and Eqs. 9 and 20 predict that

$$f(t) \approx \exp(-\frac{\kappa I_0 d}{L} t) \qquad (21)$$

The ratio $x_1^2/c \geq 0.9$ for $c \leq 0.3$ (Fig. 3b). In this limit, diffusion within the small structure is fast enough so that the fluorescence decay rate R does not depend on D but only on d, L, κ, and the intensity, as expected. In addition, R is linear with the intensity. For extremely high intensities ($c \rightarrow \infty$), $x_n \approx (2n-1)\pi/2$, $\cos(x_n) \approx 0$, $cd >> L$, $c^2 >> c$. Also, $d << L$. By using these approximations and the method of partial fractions, one can thus show that (Eq. 19)

$$f(t) \equiv \frac{F(t)}{F(0)} = \sum_{n=1}^{\infty} f_n \exp\left\{ - D[\frac{(2n-1)\pi}{2L}]^2 t \right\}$$
$$f_n \approx \frac{2dL}{L^2 + d^2(\frac{(2n-1)\pi}{2})^2} \qquad (22)$$

As expected, for high intensities, the fluorescence decay depends only on d, D and L and not on the intensity.

4.2.5 Measurements with Immobilized GFP

To determine the approximate value of κ, the decay of fluorescence with time was measured with purified GFP immobilized on the surface. In this case,

$$\frac{d}{dt} F(t) = -\kappa I_0 F(t)$$
$$\frac{F(t)}{F(0)} = \exp(-\kappa I_0 t) \qquad (23)$$

where F(t) is proportional to the density of unbleached GFP on the surface.

4.3 Methods

4.3.1 GFP Expression

The pAcGFP1 vector (BD BioSciences Clontech, Palo Alto, CA), which contains the gene for a nondimerizable GFP[152] with 94% identity to EGFP, was transformed into *E. coli* BL21-Gold (DE3) competent cells (Stratagene, La Jolla, CA) and plated on Luria Broth plates containing 1 µg/mL ampicillin (LB_{AMP}). A starter culture of liquid LB_{AMP} was inoculated with a single colony and grown overnight at 37˚C with constant shaking at 225 rpm. This starter culture was used to inoculate (1:25 dilution) 25 mL of fresh LB_{AMP} in a 250-mL flask. Once the optical density at 600 nm was between 0.5 to 0.7, the culture was induced with a final concentration of 1-mM isopropyl-β-D-thiogalactopyranoside (IPTG) and allowed to grow at 37˚C with constant shaking at 225 rpm.

4.3.2 GFP Purification

One L of culture prepared as described above was harvested 4 h after induction by centrifugation (Sorvall RC-3B, Sorvall Instruments, Newtown, CT) at 1600 g for 30 min at 4˚C. The pellet was resuspended in 30 mL of lysis buffer [20-mM Tris (pH 8.0), 200-mM NaCl, 1-mM EDTA, 1-mM PMSF, 1-mM DNase, 1-mM RNase] and pulse sonicated (Branson Ultrasonics, China) at 4˚C (18% amplitude) for two rounds of 5 min each. Cell debris were removed by centrifugation (Sorvall RC-5B with a SS-34 rotor) at 27000 g. After dialyzing overnight at 4˚C against 20-mM Tris buffer (pH 8), the sample was purified by using anion exchange chromatography (HiLoad 16/10 Q Sepharose, AKTA FPLC UPC-900, GE Healthcare, Piscataway, NJ) in 20-mM Tris buffer using a linear gradient from 0-M to 1-M NaCl. The fractions containing GFP were concentrated

in an Amicon Ultra MWCO 3,000 centrifugal filter unit (Millipore, Billerica, MA) and dialyzed into water. The protein was further purified by using size exclusion chromatography (16/60 superdex 75, GE Healthcare) with water. The purity was confirmed by using SDS-PAGE (18%) with Coomassie Brilliant Blue staining.

4.3.3 Sample Preparation

Fused silica slides (1" x 1" x 1 mm, Quartz Scientific, Fairport Harbor, OH) and glass microscope slides (3" x 1" x 1 mm, Fisher Scientific, Fair Lawn, NJ) were boiled in ICN detergent (MP Biomedicals, Solon, OH) for 10 min, bath-sonicated for 30 min, rinsed thoroughly with deionized water, and dried overnight at 160˚C. The dried slides were cleaned in an argon-ion plasma cleaner (PDC-3XG, Harrick Scientific, Ossining, NY) for 15 min at 25˚C immediately prior to use. The fused silica slides were pretreated with a 0.01% (w/v) poly-L-lysine solution (Sigma-Aldrich, St. Louis, MO) for 15 min, rinsed with minimal media [7.6-mM $(NH_4)_2SO_4$, 60-mM K_2HPO_4, 2-mM $MgSO_4$, 20-µM $FeSO_4$, 1-mM EDTA (pH 6.8)], and attached to a microscope slide with double-sided tape (Part No. 021200-64988, 3M Corp, St. Paul, MN) to form a sandwich. For osmotic stress measurements, the minimal media rinse contained 250-mM sorbitol (0.390 osmolal). The samples, which consisted of either bacterial cultures collected 3 h after induction or 2-µM purified GFP containing 5-mg/mL bovine serum albumin (Sigma-Aldrich, St. Louis, MO), were injected into the sandwiches. After incubating for 30 min at 25˚C, the sample chamber was rinsed with minimal media and sealed with vacuum grease.

4.3.4 Total Internal Reflection (TIR) Fluorescence Microscopy

Through-prism total internal reflection bleaching experiments were carried out on an instrument consisting of an inverted microscope (Zeiss Axiovert 35, Thornwood, NY), an argon ion-laser (Innova 90-3; Coherent, Palo Alto, CA), and a single-photon counting photomultiplier (RCA C31034A, Lancaster, PA). The instrument was controlled with an in-house LabVIEW program and DAQ board (PCI-MIO-16XE-50, Texas Instruments, Austin, TX). Experiments were conducted at 25^{o}C by using an excitation wavelength of 488 nm and a laser power $\leq$ 500 mW. To achieve optimal excitation intensity without overloading the detector, a 100-µm diameter pinhole was inserted in a back intermediate image plane of the microscope and aligned to correspond with the center of the TIR illumination. Polarization paper (25% transmission, Edmund Optics, NT54-795) was also inserted after the dichroic mirror and barrier filter, but before the detector, to attenuate the signal. The bleaching intensity was varied by inserting neutral density filters in the beam path prior to excitation. The fluorescence decay was collected with a 10x, 0.25 numerical aperture objective for up to 90 sec.

4.3.5 Size of Evanescent Illumination

TIR was generated on a fused silica/microscope slide sandwich containing a 1-µM solution of Alexa Fluor 488 carboxylic acid, tetrafluorophenyl ester (Molecular Probes/Invitrogen, Carlsbad, CA) as described above. Five images of the TIR spot were collected with an AT200 CCD camera and software (Photometrics, Tucson, AZ). To determine w_x and w_y (Eq. 1), slices of the images with y = 0 or x = 0 were converted to pixel intensities W(x) or W(y) with the Photometrics software and plotted as a function of

distance. The pixel dimension (0.87 μm) was determined by imaging a graticule. The data were fit in Sigma Plot (Systat Software Inc., San Jose, CA) to

$$W(x) = W_0 \exp(-\frac{2x^2}{w_x^2}) + \gamma \quad (24)$$

or

$$W(y) = W_0 \exp(-\frac{2y^2}{w_y^2}) + \gamma \quad (25)$$

with W_0, w_x(or w_y), and γ (the background) as free parameters.

4.3.6 Intensity Values

For a given incident laser power, P, at z = 0 (Eq. 1),

$$P = I_0 \int_{-\infty}^{\infty} dx \int_{-\infty}^{\infty} dy \exp(-\frac{2x^2}{w_x^2}) \exp(-\frac{2y^2}{w_y^2}) = \frac{\pi}{2} w_x w_y I_0 \quad (26)$$

The value of I_0 was determined as

$$I_0 = \frac{2P}{\pi w_x w_y} \quad (27)$$

by using Eq. 27 with the known values of P, w_x and w_y.

4.3.7 Cell Length

Samples were prepared as described above except that 5-μg/mL FM1-43 membrane stain (Molecular Probes/Invitrogen, Carlsbad, CA) was added to the samples

and No. 1.5 glass coverslips (Fischer Scientific, Fair Lawn, NJ) were used in place of the fused silica slides. The cells were imaged on a Zeiss 510 scanning confocal inverted microscope (Carl Zeiss, Thornwood, NY) with a 63x, 1.4 NA oil-immersion objective, a 65-µm pinhole, and an excitation wavelength of 488 nm. Sixteen 36.6-µm x 36.6-µm images were collected in the x-y plane by moving away from the coverslip in 0.2-µm increments. From these images, the maximum lengths of 110 cells in the z-direction were determined and averaged, yielding L = 2.2 ± 0.5 µm. Repeating this process for 107 sorbitol-treated cells gave L = 1.8 ± 0.5 µm.

4.3.8 Data Analysis

Fluorescence decays were fit to the following function by using Sigma Plot:

$$F(t) = F(0)\exp[-Rt] + \varphi \qquad (28)$$

with F(0), R and φ (the background) as the free parameters. At least three (and often more) decay curves were collected for each I_0 and the R values averaged. Three complete data sets were acquired. The average values of R as a function of I_0, for the three data sets, were fit to Eq. 20 with x_1^2 given by Eq. 11 and c given by Eq. 9. In these fits, L was fixed to 2.2 µm (see above) and the free parameters were D and b = κd. The process was repeated for the sorbitol-treated cells using L =1.8 µm (see above).

4.4. Results

4.4.1 Size of Evanescent Illumination in the x-y Plane and I_0 Values

To determine the values of w_x and w_y (Eq. 1), five images of fused silica slides coated with Alexa Fluor 488 were acquired using an imaging detector (see Methods). As shown in Fig. 4a, the lateral intensity profile of the evanescent illumination appeared to be of an elliptical Gaussian shape.[150] Images like those shown in Fig. 4a report the value of I(x,y,0) (Eqs. 1, 24, 25 and 26). The pixel intensities as a function of distance along the x-axis (y = 0) and along the y-axis (x = 0) were plotted for each image. These data were fit to Eqs. 24 and 25 and gave Gaussian-shaped curves as shown by the quality of the fits (Fig. 4b). The averages of the best-fit values were $w_x = 22.4 \pm 0.5$ μm and $w_y = 65.0 \pm 0.4$ μm. Excitation intensities I_0 were then determined by using Eq. 27.

4.4.2 Cell Length

The cell length L was measured by using confocal microscopy and *E. coli* treated with the membrane stain FM1-43. Sixteen 36.6-μm by 36.6-μm images were collected in the x-y plane by moving away from the coverslip to which the *E. coli* were adhered in 0.2-μm increments. Fig. 5 shows two slices in the x-y plane of cells at different distances from the interface. The majority of the cells were ellipsoidal and had their major axis parallel to the interface. The circles in Fig. 5a are cells attached perpendicular to the interface and thus extend further into the solution. This result is apparent in Fig. 5b (the slice farther from the interface) where the ellipsoidal shaped cells have begun to fade, while the fluorescence of the circular cells remains strong. These images also confirmed that the cells were immobilized by the poly-L-lysine and that the GFP was contained within the cells. By averaging the maximum length in the z-direction of 110 cells in

different spatial orientations, L was determined to be 2.2 ± 0.5 μm, which is consistent with the literature value.[153, 154] Repeating this process for 107 sorbitol-treated cells gave L = 1.8 ± 0.5 μm. With > 99% confidence (student's t-test), the sorbitol-treated cells are shorter than non-treated cellst, since osmotic stress shrinks the cells.[155]

4.4.3 Photobleaching Propensity

The propensity for photobleaching, described by the parameter κ (Eqs. 6, 9 and 23), was measured by monitoring the evanescently excited fluorescence decay of pure GFP immobilized on fused silica slides, as a function of time and excitation intensity. Fig. 6a shows three representative decay curves and the corresponding best fits to Eq. 28. At very low excitation intensities, bleaching was almost negligible. As the laser power was increased, so did the initial fluorescence intensity and the decay rate. As shown in Fig. 6b, the decay rate was linearly proportional to the excitation intensity. The slope of this line yields a κ (for immobilized GFP) of 0.21 ± 0.01 $\mu m^2 \mu W^{-1} sec^{-1}$.

4.4.4 Diffusion Coefficient of GFP in *E. coli*

Three complete data sets for the intensity-dependent, evanescently-excited fluorescence decays of GFP in *E. coli* were acquired. Fig. 7 shows examples of typical decay curves collected from continuous photobleaching of the cells close to the adherent surface. For each decay curve, the decay rate constant, R, was determined by fitting the data to Eq. 28 with the intensity, I_0, determined as described above. As expected, both F(0) and R increased with I_0. For each data set, the average values of R as a function of I_0 were then fit to Eq. 20 with L = 2.2 μm, x_1^2 given by Eq. 11, and c given by Eq. 9. The free parameters were D and b = κd. A representative plot showing the experimental values and their best fits to this theoretical form is shown in Fig. 8. The best fit values of

the free parameters for the three data sets were averaged to give D = 6.3 ± 1.1 $\mu m^2 sec^{-1}$ and b = 0.026 ± 0.001 $\mu m^3 \mu W^{-1} sec^{-1}$. In all cases, the parameter c was calculated by using Eq. 9 and the best-fit values of b and D along with the known values of L and I_0. The maximum value of c was 2.0, validating the use of single-exponential fits and Eq. 11 (see above).

The diffusion coefficient obtained by TIR-CP, 6.3 ± 1.1 $\mu m^2 sec^{-1}$, agrees well with that measured by confocal-FRAP on the same system in our laborartory (data not shown). The measured coefficient also agrees well with literature values for GFP diffusion in *E. coli* cells. The most commonly referenced value[137], 7.7 ± 2.5 $\mu m^2\ s^{-1}$, was obtained by using confocal FRAP. Similar studies found D = 6.1 ± 2.4 $\mu m^2\ s^{-1}$ [138] and 3.2 $\mu m^2\ s^{-1}$.[148] Other groups have measured diffusion coefficients of GFP fusion proteins in *E. coli* that are also consistent with our value, such as TorA-GFP (30 kDa), 9.0 ± 2.1 $\mu m^2\ s^{-1}$;[139] cMBP-GFP (72 kDa), 2.5 ± 0.6 $\mu m^2\ s^{-1}$;[137] and CheY-GFP (40 kDa), 4.6 ± 0.8 $\mu m^2\ s^{-1}$.[142]

The b parameter from the fits contains information about the propensity for GFP to photobleach, since b = κd. For our experimental conditions, d ≈ 0.1 μm [156] and b = 0.026 ± 0.001 $\mu m^3 \mu W^{-1} sec^{-1}$. Taken together, these values yield κ ≈ 0.26 $\mu m^2 \mu W^{-1} sec^{-1}$, which is comparable to the value (0.21 ± 0.01 $\mu m^2 \mu W^{-1} sec^{-1}$) for the immobilized GFP (Fig. 6).

Several GFP variants have been reported to reversibly photobleach.[149, 157] To assess the degree of reversible photobleaching that might be occurring, confocal microscopy was used to bleach GFP throughout entire *E coli* cells and to monitor the intracellular fluorescence over time. Post-bleach fluorescence recovery was not

observed, indicating that GFP is irreversibly photobleached over the time scale of the experiment (data not shown).

4.4.5 Effects of Osmotic Shock

To further confirm the validity of the new technique, we measured GFP diffusion in sorbitol-treated cells. Sorbitol, and other forms of osmotic shock, increase the intracellular concentration of macromolecules, which significantly decreases protein mobility.[158] Data from confocal FRAP experiments show that GFP diffusion in *E. coli* cells decreases to 0.94 ± 0.55 $\mu m^2 sec^{-1}$ in 392 milliosmolal solution.[138] A similar study reported a diffusion coefficient of 1.8 $\mu m^2 sec^{-1}$ in a 370 milliosmolal buffer.[148] For TIR-CP experiments, three complete data sets were collected for GFP in *E. coli* exposed to a 390 milliosmolal sorbitol buffer and analyzed as described above. The diffusion coefficient decreased from 6.3 ± 1.1 $\mu m^2 sec^{-1}$, to 3.05 ± 1.0 $\mu m^2 sec^{-1}$in a sorbitol buffer.

4.5 Discussion

As shown here, total internal reflection illumination with continuous photobleaching (TIR-CP) can be used to monitor the translational mobility of fluorescent molecules within small structures that are only slightly larger than optical resolution. The structures are deposited on a surface such that the evanescent wave generated by internal reflection continuously photobleaches only those fluorescent molecules very near the surface (Fig. 1). The resulting fluorescence decay curves depend on two competing processes: photobleaching and diffusion. At low excitation intensities, the propensity for photobleaching determines the rate and shape of the fluorescence decay curves. At higher excitation intensities, the diffusion rate of the fluorescent molecules across the

length of the small structure also affects the fluorescence decay curves. By examining the fluorescence decay as a function of the excitation intensity, the diffusion coefficient of the fluorescent molecules within the small structures can be determined. This new method was demonstrated by measuring the diffusion coefficient of GFP in *E. coli*. The measured diffusion coefficient agreed with those measured by different methods.[137-139, 142, 148] In addition, data were acquired for GFP in *E. coli* subjected to an osmotically stressed environment and analysis of these data reported lower GFP diffusion coefficients. This result is also consistent with data obtained by different methods.[138, 148]

As described in the Introduction, other techniques have also been developed for examining molecular mobility in small biological structures, particularly *E. coli*. The most well developed of these methods is confocal-FRAP. Two advantages of TIR-CP as compared to confocal-FRAP are that the evanescent illumination confines photobleaching to a smaller fraction of the *E. coli* volume and the simplicity of the required instrumentation. TIR-CP also avoids the complication of aligning a very small focused laser beam within the small structure of interest (e.g., *E. coli*). However, for both methods, either the shape of the *E. coli* must be approximated to obtain analytical theoretical forms for the exact geometry of a given *E. coli* must be measured and used in numerical simulations.

Confocal-FRAP monitors diffusion on a cell-by-cell basis, and, although data analysis is somewhat tedious, this method can provide diffusion coefficient histograms and correlations of intracellular molecular mobility with other cellular characteristics. In TIR-CP as described here, a few cells rather than one are in the observed volume. However, the possibility exists of generalizing TIR-CP by using a fast EMCCD camera

and subsequent imaging. Because the evanescent intensity varies as a function of position (Fig 4), the entire range of intensity-dependent decay curves could be acquired from a single time-dependent image sequence. Given a dilute enough density of adherent cells, this method might also provide histograms of apparent diffusion coefficients, as well as correlations of mobility with other cellular properties.

A third method, TIR-FRAP, has also been used to measure the cytoplasmic mobility of fluorescent molecules close to the inner leaflet of membranes of surface adherent, large eukaryotic cells.[149] TIR-FRAP has potential for being generalized to small cells such as *E. coli*. TIR has also been combined with FCS to monitor translational mobility close to surface-adsorbed model membranes.[159] TIR-FCS could, in principle, measure membrane-local diffusion coefficients in small structures. Such potential TIR-FCS measurements, however, would suffer because the pool of unbleached molecules is limited in small structures. In addition, it has been demonstrated that the apparent diffusion coefficients of proteins close to membrane surfaces is significantly reduced due to hydrodynamic effects.[160] Such potential measurements, therefore, would not directly report the overall apparent diffusion coefficient of fluorescent molecules throughout the structure.

In this paper we have used TIR-CP to examine protein diffusion in *E. coli*. This new method may also be applicable to other small biological structures such as phospholipid vesicles, isolated synaptic vesicles, and isolated organelles (e.g., mitochondria). Furthermore, the technique shows promise for use over a wide range of protein concentrations. While FCS is strictly limited to very low concentrations, confocal-FRAP becomes challenging at low concentrations due to poor signal-to-noise.

In contrast, TIR-CP is applicable both to low and high concentrations, because of the range of excitation intensities available. Analysis at these concentrations may be important as it has been reported that the level of protein expression in *E. coli* may affect the protein diffusion coefficient.[137] In addition, controlling the level of one protein while monitoring the diffusion coefficient of another protein might reveal not only concentration-dependent diffusion, but also provide insight about protein-protein interactions.

4.6 Acknowledgements

We thank Michael Chua of the UNC Microscopy Facility for assistance with confocal microscopy and Xiang Wang of UNC Chemistry for assistance with imaging the evanescent illumination. This work was supported by NSF Grants MCB-0641087 (NLT) and MCB-0516547 (GJP), an NSF Graduate Fellowship Award 2006037054 (KMS), and by NIH Director's Pioneer Award DP10D783 (GJP).

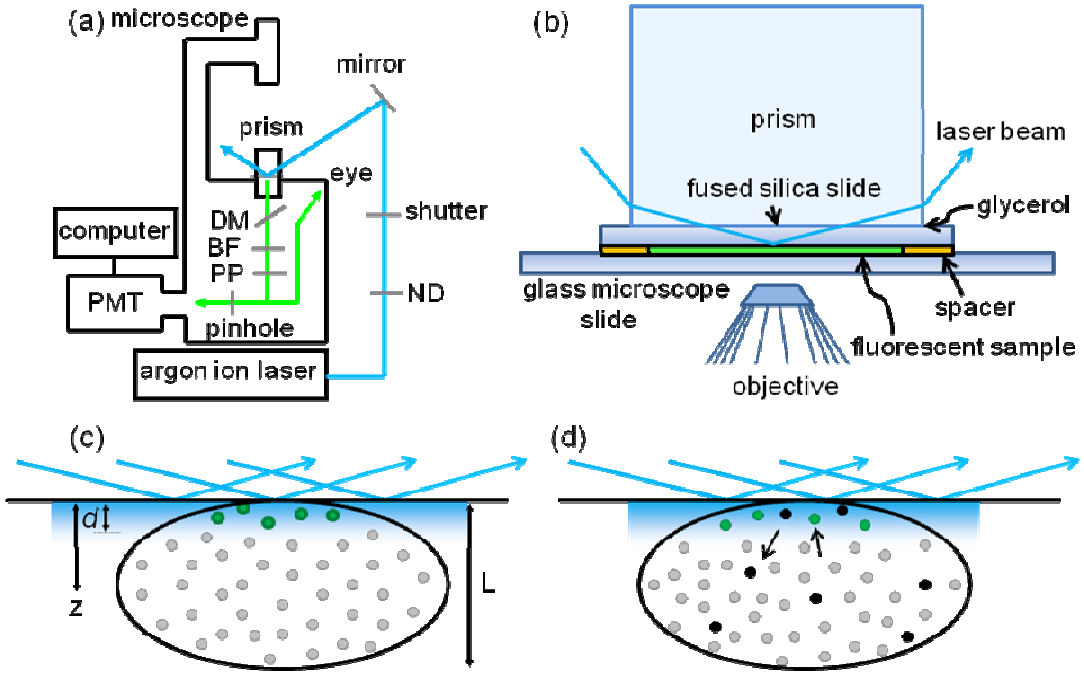

Figure 4.1 Through-Prism Total Internal Reflection with Continuous Photobleaching (TIR-CP). (a) Schematic of the instrumentation: PMT, photomultiplier tube; BF, barrier filter; DM, dichroic mirror; PP, polarization paper (see Methods); ND, neutral density filter. (b) A fused silica prism is optically coupled with glycerol to a sandwich made from fused silica and microscope slides. (c) Small structures that extend a distance L into the solution are attached to the lower surface of the fused silica slide. A laser beam is internally reflected at the interface of the fused silica slide and the internal solution of the sandwich to create an evanescent field whose intensity decays exponentially with distance, z, from the interface. The characteristic distance of this decay, d, is much smaller than L. Molecules contained within the small structure do not fluoresce (grey circles) until they diffuse into the surface-associated evanescent field. (d) Eventually, the fluorescent molecules (green circles) are permanently bleached (black circles) by exposure to the evanescent field. At low excitation intensities, the decay of evanescently excited fluorescence with time is dominated by the propensity for photobleaching. At high excitation intensities, the decay of fluorescence with time is dominated by diffusion through the length of the small structure.

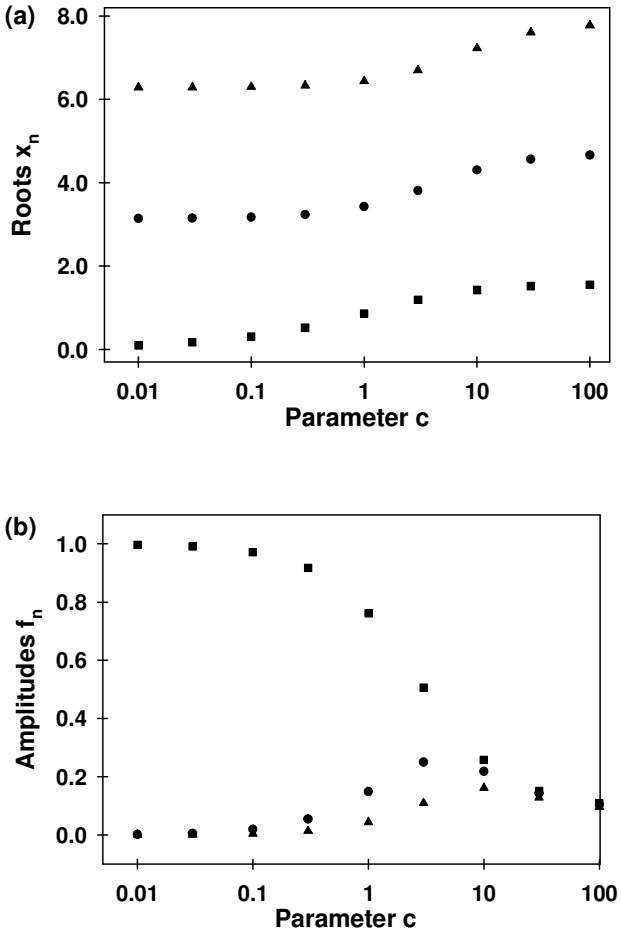

Figure 4.2 Parameters x_n and f_n. Fluorescence decay during continuous photobleaching is described by an infinite sum of exponentials with rates $D(x_n/L)^2$, where D is the diffusion coefficient and L is the cell length (Eqs. 9 and 19). The parameters x_n are a discrete, countably-infinite set of values that are determined by the value of the parameter c. Parameter c depends on experimental conditions (D, L, the depth of the evanescent wave d, and the bleaching propensity κ). Most importantly, c is proportional to the excitation intensity I_0. The parameters f_n are amplitudes associated with the different exponentially decaying terms and are defined, in general, by the values of c, L, d and x_n. (a) The values of x_1 (■), x_2 (●) and x_3 (▲) were calculated numerically as a function of c by using Eq. 9. (b) The values of f_1 (■), f_2 (●) and f_3 (▲) were calculated by using Eq. 19 with L = 2.2 μm and d = 0.1 μm. At low c values, the first amplitude, f_1 is much larger than the others and the fluorescence decay can be approximated as a single exponential with rate $D(x_1/L)^2$. In addition, for many experimental conditions, the terms associated with rates having n > 1 decay too rapidly to affect the observed fluorescence decay.

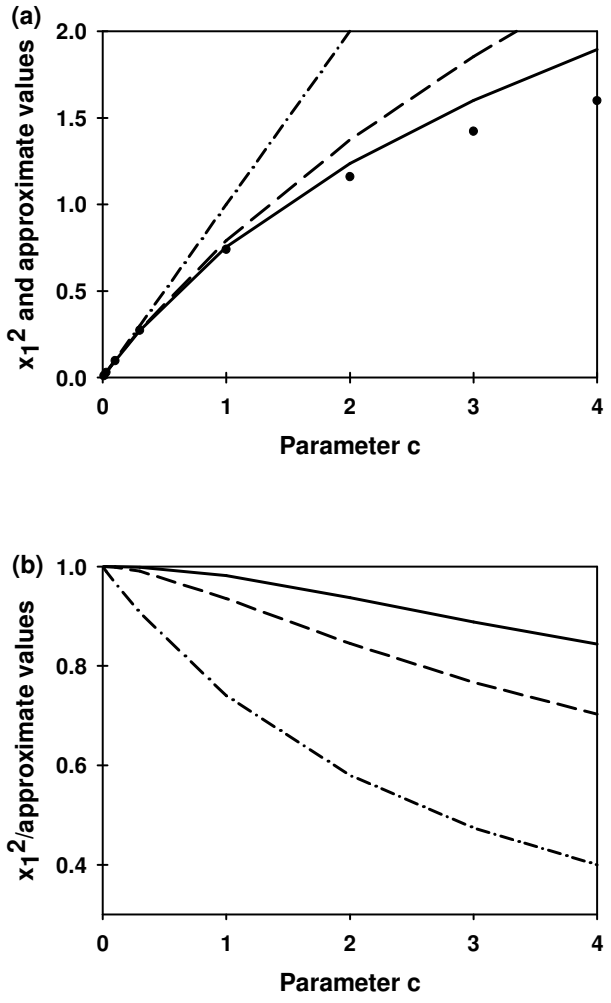

Figure 4.3 Accuracy of x_1^2 Approximations. Parameters x_n and c are described in the caption to Fig. 2. (a) This plot shows x_1^2 approximated as c (- · - ·) (see text), as Eq. 10 (- - -) and as Eq. 11 (—) compared with the numerically determined values (•) as a function of the parameter c (Eq. 9). (b) This plot shows the corresponding ratios of the actual x_1^2 values divided by the approximations as a function of c, such that values close to one represent an accurate approximation. As shown, Eq. 11 is a good approximation for the experimental conditions used in this work ($c \leq 2$).

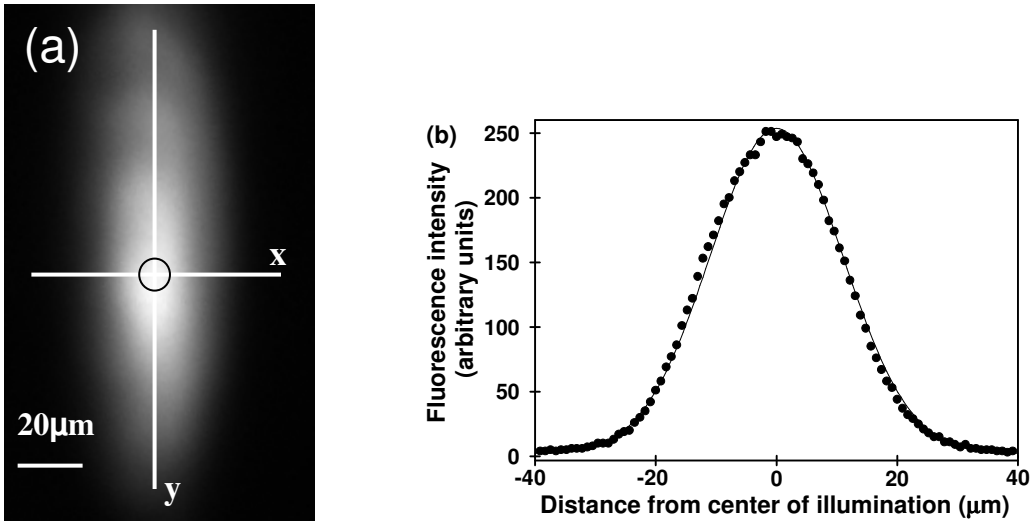

Figure 4.4 Spatial Profile of the Evanescent Illumination in the x-y Plane.
(a) Evanescently excited Alexa Fluor 488 dye was non-specifically adsorbed to the surface of fused silica. The circle indicates the observed area within the pinhole. (b) Data were obtained by slicing images with x = 0 or y = 0 and plotting the corresponding pixel intensities as a function of distance. A representative slice with y = 0 and its best fit to Eq. 24 is also shown.

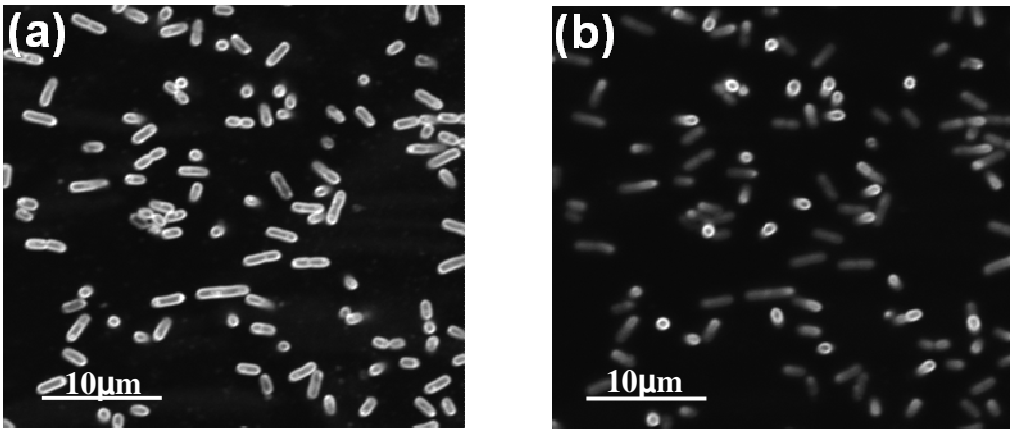

Figure 4.5 Cell Length, L. *E. coli* cells expressing GFP were stained with FM1-43 dye and attached to poly-L-lysine coated coverslips. Using a confocal microscope, images were collected in the x-y plane by moving away from the coverslip in 0.2-µm increments. The images are 36.6 µm x 36.6 µm and were collected (a) 1.4 µm and (b) 2.4 µm from the coverslip.

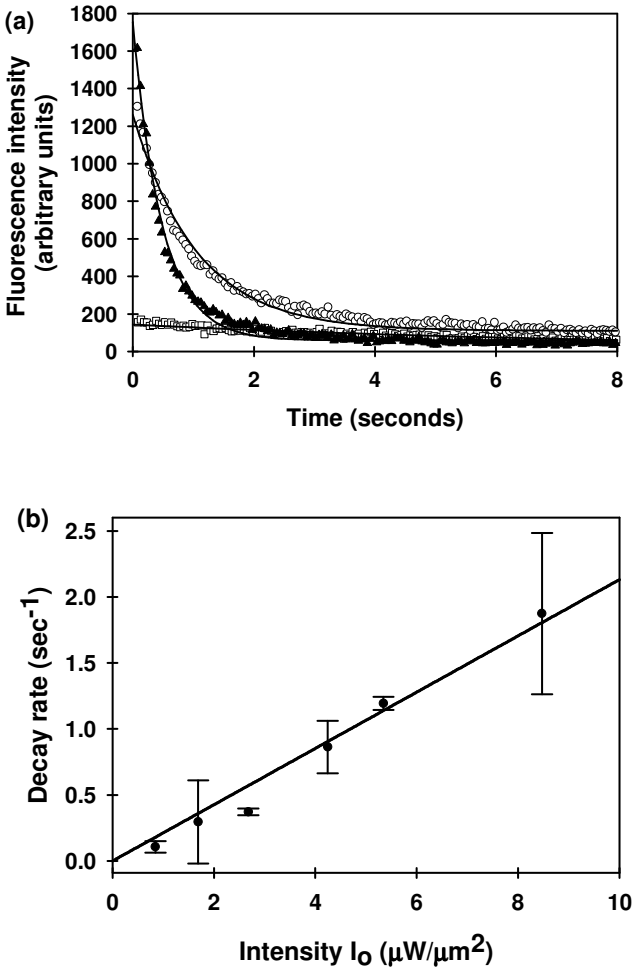

Figure 4.6 Photobleaching Propensity for Immobilized GFP. (a) Representative evanescently excited fluorescence decay curves are shown for purified GFP immobilized fused silica. The excitation intensities I_0 were 0.9 (□), 4.3 (○), and 8.5 (▲) μW/μm^2. Th solid curves show the best fits of the data to Eq. 28. (b) The average fluorescence decay R is a linear function of the excitation intensity, I_0.

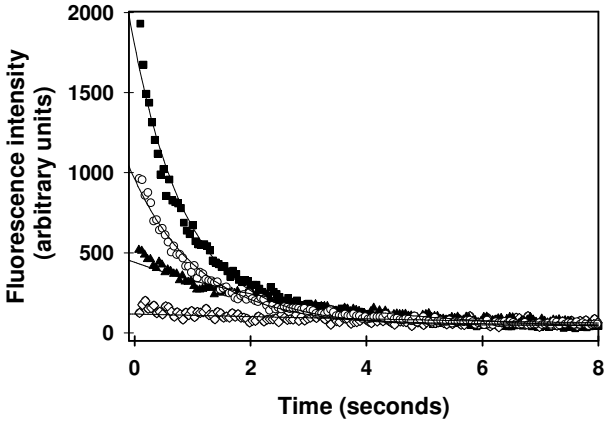

Figure 4.7 Representative Evanescently Excited Fluorescence Decay Curves for GFP in *E. coli* Cells. The excitation intensities were 5 (◊), 35 (▲), 87 (○), and 220 (■) μW/ μm^2. The solid curves show the best fit of the data to Eq. 28.

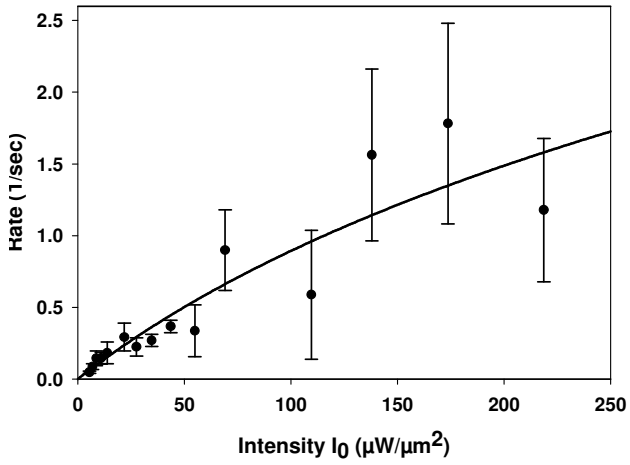

Figure 4.8 Diffusion Coefficient D and Parameter b for GFP in *E. coli*. Plot shows data from one data set in which the measured decay rates R are plotted as a function of the excitation intensities, I_0. Rates represent an average of at least three measurements with uncertainties given as standard deviations. The line shows the best fit to Eq. 20 with x_1^2 given by Eq. 11, L fixed at 2.2 μm, and free parameters D and b = dκ. In this case, D = 6.3 $\mu m^2 sec^{-1}$, b = 0.025 $\mu m^3 \mu W^{-1} sec^{-1}$, the maximum value of c = 2.0 (Eq. 9), and correlation coefficient was 0.93.

4.7 References

1. Axelrod, D.; Koppel, D. E.; Schlessinger, J.; Elson, E.; Webb, W. W., Mobility measurement by analysis of fluorescence photobleaching recovery kinetics. *Biophys. J.* **1976,** *16* (9), 1055-69.

2. Lippincott-Schwartz, J.; Snapp, E.; Kenworthy, A., Studying protein dynamics in living cells. *Nat. Rev. Mol. Cell Biol.* **2001,** *2* (6), 444-56.

3. Mullineaux, C. W., Localization and mobility of bacterial proteins by confocal microscopy and fluorescence recovery after photobleaching. *Methods Mol. Biol.* **2007,** *390*, 3-16.

4. Elowitz, M. B.; Surette, M. G.; Wolf, P. E.; Stock, J. B.; Leibler, S., Protein mobility in the cytoplasm of Escherichia coli. *J. Bacteriol.* **1999,** *181* (1), 197-203.

5. Konopka, M. C.; Shkel, I. A.; Cayley, S.; Record, M. T.; Weisshaar, J. C., Crowding and confinement effects on protein diffusion in vivo. *J. Bacteriol.* **2006,** *188* (17), 6115-23.

6. Mullineaux, C. W.; Nenninger, A.; Ray, N.; Robinson, C., Diffusion of green fluorescent protein in three cell environments in Escherichia coli. *J. Bacteriol.* **2006,** *188* (10), 3442-8.

7. Thompson, N. L.; Lieto, A. M.; Allen, N. W., Recent advances in fluorescence correlation spectroscopy. *Curr. Opin. Struct. Biol.* **2002,** *12* (5), 634-41.

8. Rigler, R.; Elson, E. S., *Fluorescence Correlation Spectroscopy, Theory and Applications. Springer Series in Chemical Physics, No. 65,*. Springer-Verlag: Heidelberg, Germany, 2001.

9. Cluzel, P.; Surette, M.; Leibler, S., An ultrasensitive bacterial motor revealed by monitoring signaling proteins in single cells. *Science (New York, N.Y* **2000,** *287* (5458), 1652-5.

10. Peters, R.; Brunger, A.; Schulten, K., Continuous fluorescence microphotolysis: A sensitive method for study of diffusion processes in single cells. *Proc. Natl. Acad. Sci. U.S.A.* **1981,** *78* (2), 962-966.

11. Brünger, A.; Peters, R.; Schulten, K., Continuous fluorescence microphotolysis to observe later diffusion in membranes. Theoretical methods and applications. *J. Chem. Phys* **1984,** *82*, 2147-2160.

12. Delon, A.; Usson, Y.; Derouard, J.; Biben, T.; Souchier, C., Continuous photobleaching in vesicles and living cells: a measure of diffusion and compartmentation. *Biophys. J.* **2006,** *90* (7), 2548-62.

13. Wachsmuth, M.; Weidemann, T.; Müller, G.; Hoffmann-Rohrer, U. W.; Knoch, T. A.; Waldeck, W.; Langowski, J., Analyzing intracellular binding and diffusion with continuous fluorescence photobleaching. *Biophys. J.* **2003,** *84* (5), 3353-63.

14. Arkhipov, A.; Hüve, J.; Kahms, M.; Peters, R.; Schulten, K., Continuous fluorescence microphotolysis and correlation spectroscopy using 4Pi microscopy. *Biophys. J.* **2007,** *93* (11), 4006-17.

15. van den Bogaart, G.; Hermans, N.; Krasnikov, V.; Poolman, B., Protein mobility and diffusive barriers in Escherichia coli: consequences of osmotic stress. *Mol. Microbiol.* **2007,** *64* (3), 858-71.

16. Swaminathan, R.; Bicknese, S.; Periasamy, N.; Verkman, A. S., Cytoplasmic viscosity near the cell plasma membrane: translational diffusion of a small fluorescent solute measured by total internal reflection-fluorescence photobleaching recovery. *Biophys. J.* **1996,** *71* (2), 1140-51.

17. Burghardt, T.; Thompson, N., Evanescent intensity of a focused Gaussian light beam undergoing total internal reflection in a prism. *Opt. Eng.* **1984,** *23*, 62-67.

18. Thompson, N. L.; Burghardt, T. P.; Axelrod, D., Measuring surface dynamics of biomolecules by total internal reflection fluorescence with photobleaching recovery or correlation spectroscopy. *Biophys. J.* **1981,** *33* (3), 435-54.

19. Yang, F.; Moss, L. G.; Phillips, G. N., Jr., The molecular structure of green fluorescent protein. *Nat. Biotechnol.* **1996,** *14* (10), 1246-51.

20. Koch, A. L., The variability and individuality of the bacterium. In *Escherichia coli and Salmonella typhimurium: Cellular and Molecular Biology* Neidhardt, F., Ed. American Society for Microbiology: Washington D.C., 1987; Vol. 2, pp 1608-1614.

21. Cullum, J.; Vicente, M., Cell growth and length distribution in Escherichia coli. *J. Bacteriol.* **1978,** *134* (1), 330-7.

22. Baldwin, W. W.; Sheu, M. J.; Bankston, P. W.; Woldringh, C. L., Changes in buoyant density and cell size of Escherichia coli in response to osmotic shocks. *J. Bacteriol.* **1988,** *170* (1), 452-5.

23. Thompson, N. L.; Pero, J., Total internal reflection fluorescence microscopy: Applications in biophysics, in Fluorescence Spectroscopy in Biology: Advanced Methods and Their Applications to Membranes, Proteins, DNA and Cells. Wolfbeis, O.; Hof, M.; Hutterer, R.; Fidler, V., Eds. Springer-Verlag: Berlin, 2005; pp 79-103.

24. Sinnecker, D.; Voigt, P.; Hellwig, N.; Schaefer, M., Reversible photobleaching of enhanced green fluorescent proteins. *Biochemistry* **2005,** *44* (18), 7085-94.

25. Cayley, S.; Record, M. T., Jr., Roles of cytoplasmic osmolytes, water, and crowding in the response of Escherichia coli to osmotic stress: biophysical basis of osmoprotection by glycine betaine. *Biochemistry* **2003,** *42* (43), 12596-609.

26. Starr, T. E.; Thompson, N. L., Fluorescence pattern photobleaching recovery for samples with multi-component diffusion. *Biophys. Chem.* **2002,** *97* (1), 29-44.

27. Pero, J. K.; Haas, E. M.; Thompson, N. L., Size dependence of protein diffusion very close to membrane surfaces: measurement by total internal reflection with fluorescence correlation spectroscopy. *Journal of Physical Chemistry B* **2006,** *110* (22), 10910-8.